Atomistic Spin Dynamics Modeling of Spintronic Control in Mn_2Au

Jackson L. Ross

Doctor of Philosophy

University of York
Department of Physics, Engineering and Technology

December 2024

Abstract

Antiferromagnetic spintronics is a complex and valuable field of ongoing research, critical for the development of beyond-start-of-the-art ultrafast, low energy computing and memory devices. Since they are largely unaffected by external magnetic fields, laser excitation, applied currents, and dynamic temperature changes represent the only methods for spintronic control in antiferromagnets. With the vast range of conducting, semi-conducting, and insulating antiferromagnets available to materials science, along with limitless multilayer combinations, there is a crucial need for advanced simulation techniques applicable to time and size scales orders of magnitude faster and smaller than ferromagnets. Mn_2Au is of high interest to the spintronics community due to the presence of an intrinsic spin-orbit torque allowing for field-free spintronic control. Likewise, Mn_2Au presents an ideal platform for advanced atomistic spin dynamics model development: a high Néel temperature, high conductivity, and ordered collinear magnetic and metallic structure make it especially appropriate for highly physical simulations with minimal compromises to model integrity.

Here, we use atomistic spin dynamics to model and simulate Mn_2Au magnetic domain and domain wall control using existing and novel spintronic control methods. A chief result of this thesis is the implementation from *ab initio* theory of a novel laser induced torque using linearly polarised light to switch single domains and drive domain walls. The symmetry of this torque can be leveraged to produce robust toggle, preferential, and deterministic all-optical switching, even under conditions of extreme transient laser heating. This torque is also applied to domain walls, with the symmetry allowing for efficient, ultrafast domain wall motion, domain wall pinning, and domain wall contraction. An additional result with our domain wall simulations is the redescription of the model Hamiltonian used for Mn_2Au in atomistic modelling. This Hamiltonian allows for calculation of the temperature-dependent anisotropy and exchange scaling for use in micromagnetic simulations. Lastly, we expand the drift-diffusion formalism for spin transport to include the current-induced spin polarisation generating the intrinsic Néel spin-orbit torque, calculating directly the correlated effect of non-linear spin accumulation through a domain wall with the intrinsic current-induced spin accumulation of Mn_2Au.

Thus, this thesis presents advances in model development for atomistic spin dynamics simulations and spintronic control methods for antiferromagnets. With spintronics poised as the foundation for next generation computing devices and hardware, advances to antiferromagnetic modeling capabilities are highly relevant to fundamental, developmental, and applications focused research. As such, it is the hope of the author that this thesis will prove useful for a variety of groups and fields beyond the atomistic modeling community.

For Sokka and Zuko
and Erica and now also baby Aidan

Acknowledgements

Despite the single name on the title page, no thesis is the work of an individual. For every thesis accepted, there is a small battalion of collaborators, supervisors, seminar speakers, fellow students, coffee grounds, and even family members in need of acknowledgement. As much as the declaration on the next page confirms this thesis is my own work, it is also true to say it would not have been possible without the help, support, and guidance of numerous parties: my closest collaborator (and friend), Paul; my supervisors and mentors, Roy and Richard; and the voice outside my head telling me what not to do, Oksana.

So long, and thanks for all the physics.

Declaration

I hereby declare that except where specific reference is made to the work of others, the contents of this dissertation are original and have not been submitted in whole or in part for consideration for any other degree or qualification in this, or any other university. The majority of this thesis has been presented at various conferences by the author, some chapters being based on the following publications:

Published:

- **J.L. Ross**, P.-I. Gavriloaea, F. Freimuth, T. Adamantopolous, Y. Mukrousov, R.M. Otxoa, R. Chantrell, R.F.L. Evans, and O. Chubykalo-Fesenko. "Ultrafast Switching of Mn_2Au Using a Novel Laser Optical Torque." *npj Comp. Materials*. (2024)
- P.-I. Gavriloaea, **J.L. Ross** F. Freimuth, Y. Mukrousov, R. Chantrell, R.F.L. Evans, O. Chubykalo-Fesenko, and R.M. Otxoa. "Efficient Motion of 90deg Domain Walls in Mn_2Au via Pure Optical Torques." *npj spintronics*. (2025)
- J.A. Velez, M.-K. Lee, G. Tatara, P.-I. Gavriloaea, **J. Ross**, D. Laroze, U. Atxitia, R.F.L. Evans, R. Chantrell, M. Mochizuki, and R. M. Otxoa. "Chaotic Proliferation of Relativistic Domain Walls for Reservoir Computing." *npj spintronics*. (2025)
- M. Zho, M. Jalali, Z. Zhang, R.F.L. Evans, **J.L. Ross**, R. W. Chantrell., and Y. Liu. "Antiferromagnetic Dynamics of Mn_2Au Driven by Spin Current Pulses with Perpendicular Spin Polarization." *APL*. (2025)

In Review:

- **J.L. Ross**, S. Jenkins, R. Rama-Eiroa, P.-I. Gavriloaea, J. Collings, U. Atxitia, O. Chubykalo-Fesenko, K. Everschor-Sitte, R.M. Otxoa, R. Chantrell, and R.F.L. Evans. "Thermal Effects on Domain Wall Motion in Mn_2Au." (2024)

In Preparation:

- **J.L. Ross**, R. Khantari, P.-I. Gavriloaea, R.M. Otxoa, R.F.L. Evans, J. Chureemart, R.W. Chantrell, and P. Chureemart. "Spin Accumulation Model of the Néel Spin Orbit Torque in Mn_2Au." (2025)

Table of contents

List of tables

List of figures

1

Motivation

The current decade has seen many landmark moments for the computing and data industries: the inevitable failure of Moore's law for data storage, the exponential growth of both power and data storage requirements for the machine learning industry, and, more optimistically, the commercial release of devices making use of heat assisted magnetic recording (HAMR) media for ultra-high density memory storage. While HAMR devices have entered the market with an already impressive energy improvement of 50% over traditional HDD storage media, the lifetime and scope of the technology is limited by the storage medium itself. The problems affecting HAMR technology has often been referred to as a "quadrilemma" [1]. HAMR technology requires high thermal stability, low error rate, high bit density, and minimal external fields. Even with an ideal material, however, HAMR would always remain a technology which is efficient but *slow*; with a bit recovery time on the order of nanoseconds and write time limited to microseconds, HAMR does not lend itself to *ultrafast* memory storage. This, perhaps, extends our quadrilemma into a pentalemma [2]: not only must our ideal storage media be stable and high density, it must be fast. Faster, at least, than conventional HDD storage techniques.

In the push to *ultrafast* memory storage, speedup is not measured in percentages, but orders of magnitude. While state-of-the-art memory devices can read and write up to 20 GB/s, the theoretical limit for magnetic-based operations exists in the range of TB/s [3–5]. The base rational for this drastic difference in operation timescale comes from a change in the

fundamental physics used to read and write memory. In general, operations with *ferro*magnets are limited to the nanosecond (ns) range (GB/s) [6]. Similar to how the tension of a piano wire determines its frequency, the energetic coupling in a ferromagnet (FM) operates at frequencies in the GHz (ns) range. *Anti*ferromagnets, however, operate at an entirely different set of frequencies, from the high GHz to low THz (picosecond, ps) range [7]. Thus, platforms using antiferromagnets (AFMs) for their devices could see orders of magnitude speedup, saving costs in efficiency and drastically improving performance.

But this opportunity is not without physical limitations. Since AFMs emit no stray magnetic fields, control options are limited to the other available nanoscale forces: electric fields, current, lasers, pressure, temperature, and structure. Thus, development of AFMs for commercial storage and computing use requires research into not just device fabrication, but also control schemes able to read and write AFMS on their ultrafast timescale. In general, any singular AFM control method, alone, invariably fails to satisfy a condition of the 'pentalemma' from above. The solution, perhaps, takes inspiration from HAMR: seek combinations of control methods to satisfy our criteria. Just as HAMR utilises local changes in temperature to increase the density of storage bits accessible to a magnetic field, combinations of AFM control mechanisms could allow ultrafast dynamics without compromising on storage density or power consumption.

One promising development in the field has been the discovery of AFMs which respond asymmetrically to electric fields, either in the form of an applied potential to generate current or the electric field directly. This response has been known for AFMs for nearly twenty years, but in the form of laser excitation [8]. Its use, however, was restricted to insulating AFMs, and only for very low temperatures (< 80K). The direct control of an AFM using an electric field from an applied potential would take another decade [9]. The distinction of an electric field generated by an applied potential is made from an applied current due to a nuanced distinction in the mechanism of control: up until recently, applied currents to AFMs were used as a transfer medium for spin injection, either from a heavy metal layer (called spin-orbit torque (SOT)) or from a reference FM layer (generally called spin-transfer torque (STT)). The details of these mechanisms will be covered later, but they of course form the basis for the field of *spintronics*: the coupling of the electron's charge and spin nature [3]. While a

changing electric current will generate a magnetic field through Faraday's Law, spintronics uses instead the intrinsic effect spin-polarised charge currents can have to interact with materials. Useful for both measuring and modifying FMs and AFMs, the spin-polarised charge current already represents a combined control method from those listed above; except for very specific cases, the charge current requires a structure of multiple materials in order to become spin polarised. Two materials, however, have recently been discovered to be spintronically-active without the need for multilayered heterostructures to spin polarise charge currents. CuMnAs [9] and Mn_2Au [10]–both metallic AFMs stable at room temperature–respond asymmetrically to applied electric fields generating a current induced spin polararisation (CISP) which exerts torque on the AFMs depending on the direction of the applied field [11, 12]. This effect has been used experimentally to switch the magnetic domains of AFMs [13, 14] and inject spin currents to other magnetic materials [15], and predicted computationally to drive domain walls [16, 17].

The distinction of magnetic control between current and electric field is hardly a semantic one. For clarity, in this thesis control of AFMs using current will reference the moving charge of electrons which can *gain* a spin polarised component, while control from an applied field refers to the CISP caused by the intrinsic nature of the material itself [12]. Both control methods will generate torque with the right symmetry to switch AFM domains and drive domain walls [18, 19] (more detail in Chapter 4), and Chapter 6 details the modelling of both processes simultaneously). But while the intrinsic CISP is traditionally activated through a DC applied potential, recent experiments have also excited AFM dynamics using THz frequencies to drive AC currents which generate a CISP [20, 21].

This brings in another control method mentioned earlier, laser excitation. Once again, the distinction between torque generated by an electric field and a laser excitation is not a semantic one, and is in fact the main result of this thesis: laser excitations, even at an optical frequency, can generate dynamics distinct from those caused by CISPs, spin injections carried by current, and rapid changes in temperature. This torque–so called the laser optical torque (LOT) due to its similarity to SOT–nonetheless has its own set of symmetry rules affecting switching [22] and domain wall driving [23]. The source of this control stems from the 2^{nd} order coupling of

the electric field to the susceptibility tensor of the electronic structure of the material, generally described in [24, 25] as:

$$\delta \mathbf{S}_i = \chi_{ij} E_j(t) + \chi_{ijk} E_j(t) E_k(t) \tag{1.1}$$

where the term linear in $E_j(t)$ corresponds to the SOT [12], even if driven by a THz electric field. This makes a 2^{nd} order excitation distinct from the CISP generated by an applied potential or a THz electric field supplied by laser excitation. And indeed, the electric field from THz excitation likewise carries a substantial 2^{nd} order coupling term in addition to the CISP [25]. While this effect has been known for insulating AFMs [26, 8], it has not been applied to metallic systems useful for spintronics.

The goal of this thesis, therefore, is to present the use of this novel LOT–in combination with traditional control measures for metallic AFMs–as a control method in Mn_2Au useful for spintronic devices. Mn_2Au provides an excellent material platform for modelling and model development of magnetic control using atomistic spin dynamics simulations. It has a very high Néel temperature (above 1000K) [10] and strong metallic character [20], and its collinear structure allows relatively straightforward analytic descriptions [17, 27], at least compared to non-collinear systems such as Mn_3Sn [28]. And, unlike complex non-collinear systems such as Mn_3Sn, dynamic modelling of system sizes approaching nanoscale devices does not require simplification of the physics. This thesis presents results on the use of a LOT for single domain switching (Chapter 3), domain wall driving at 0K (Chapter 4), and domain wall driving at finite temperatures (Chapter 5) in Mn_2Au. As a step towards combined spintronic control, this thesis also presents development integrating a drift-diffusion spin accumulation model with the CISP generated from an applied potential (Chapter 6).

2

Background and Theory

2.1 Atomistic Spin Models

At the atomistic level, magnetism is intrinsically a *quantum* phenomena. The fundamental magnetic moment, μ_B, is quantised directly in the angular momentum part of the solution to the Schrödinger equation as $\mu_B = e\hbar/2m_e = 9.274 \times 10^{-24} J/T$. Fortunately for us, while each electron has an intrinsic magnetic moment of μ_B, 1.8 L of water with its times 1.08×10^{27} electrons does not have a moment of $10.6 \times 10^2 J/T$. Otherwise, in Earth's gentle magnetic field of 50 μT, we could boil our pasta–or ourselves–with nothing but a mechanical stirrer. In fact, it was this very conundrum–the discrepancy between the electrons' magnetic moments and the correspondingly minimal saturated magnetic moments displayed in materials–that contributed to early push-back of the intrinsic spin-moment of the electron. The competition between spin order and disorder is thankfully resolved by the Pauli exclusion principle and Hund's rules: unpaired electrons are to be found only in the valence band (generalising without any photoexcitation or other transient effects). This is not to say, however, that only valence spins contribute to the magnetic landscape of a material. Fig. 2.1 demonstrates a general transition metal material with an unequal density of states (DoS) between "spin up" and "spin down" electrons in the valence band (the Fermi level for metallic materials). While the Fermi level is dominated by spin down states, the total spin of the states from zero energy to the Fermi level would give a net up value.

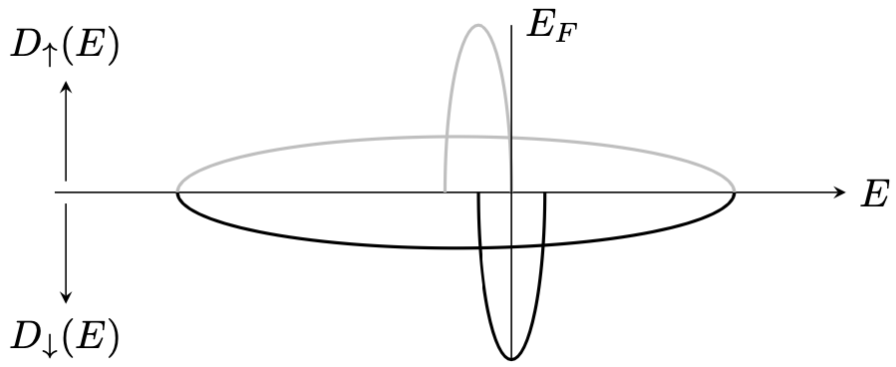

Fig. 2.1 Majority and minority picture of density of states for a generic transition metal. The narrow in energy bands represent the d-orbitals and the wide bands are the sp-orbitals. Figure from [29].

Multiple phenomena compete at the quantum level to dominate this trend, both inside the atom and between atoms, requiring robust *ab initio* theory which often gives results counter to our intuition. Atomistic spin models serve as the in-between scale for quantum mechanical *ab initio* calculations and experimental laboratory results. To do this, Fig. 2.2 illustrates the separation of the multi-scale dynamics of the magnetic system: the basic magnetic material is composed of ordered spins, fixed in place, which represent the subatomic magnetic structure of the material. For materials suitable for ASD modelling, the magnetic texture inside the atomic volume is highly localised and static.

From the experimental side, information about the atomistic magnetic moment is informed by measurements utilising the dipole nature of magnetism:

$$E = -\mathbf{m} \cdot \mathbf{B}$$

gives the energy for a magnetic moment $\mathbf{m}$ in the presence of an external field $\mathbf{B}$. The moment relates to the *saturated magnetisation* of the system, M_s, through $\mathbf{m} = \mathbf{M}_s V$. With a known crystal geometry to give the ratio of atoms to volume, the atomic spin μ_s can be reasonably calculated from $\mu_S = M_s V / n_{atoms}$. More complex materials can have multiple contributing spins in a unit cell. Since these specific contributions can be measured and calculated separately, we can represent the magnetic contribution from species i as $mu_{s,i} = M_{s,i} V / n_{atoms,i}$. *Unusual*

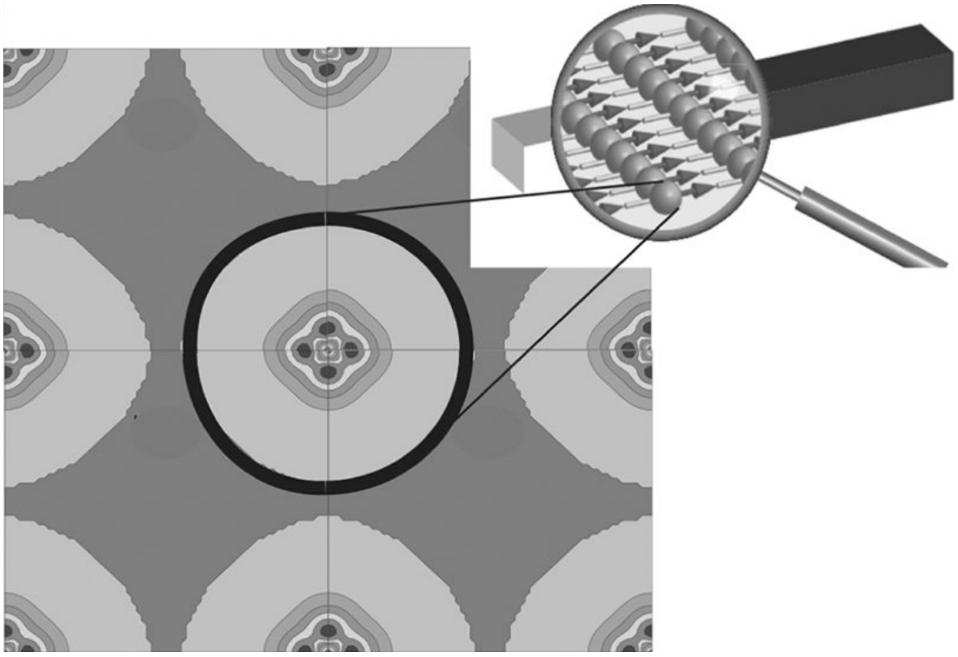

Fig. 2.2 Schematic illustration of multi-scale spin models from subatomic to bulk material. The homogeneous region between the atoms contains no (or static) magnetisation compared to the highly localised magnetic texture inside the atomic volume. Figure from [30].

cases of magnetism correspond to a loss of the ability to represent the magnetisation of a material as arising from an orientation of spins confined to a non-periodic volume, such as a highly dispersive charge-density wave. But for transition metal magnets, nearly all of the moment is localised to the *d* orbitals. *Ab initio* methods can indeed match closely with the experimentally measured μ_s [30], but beyond μ_s there are few easily comparable variables accessible to both *ab initio* and experimental methods. Instead, we must rely on the simulation and modelling of magnetic systems using *ab initio* constants to compare with experimental measurements. Thus, we turn to the background behind ASD constants.

2.1.1 First Principles Background

First principles calculations are especially important for atomistic modelling, as rarely are we interested in the bulk case of a material with only simple ferromagnetism. In such a case, the relationship for $\mu_{s,i}$ above becomes less useful: while we may know the individual moment of each magnetic species, it can be difficult to assign energetic preferences between

them. On the first principles scale, more sophisticated methods than the Stoner model allow for calculation of complex systems with strong spin polarised states above and below the Fermi level, anisotropic preferences for orbital and spin density, and multiple spin species with varying magnetic moments. Much work must be done, however, to reach the appropriate atomistic constants from the quantum mechanical models. The full many-body Hamiltonian for a quantum mechanical system lattice of electrons and nuclei requires a description of all nuclei-nuclei (I,J), electron-electron (i,j), and electron-nuclei (i,I) interactions [30]:

$$\mathcal{H} = -\frac{\hbar^2}{2}\sum_I \frac{\nabla_I^2}{M_I} + \frac{1}{2}\sum_{I\neq J}\frac{1}{4\pi\varepsilon_0}\frac{Z_I Z_J e^2}{|\mathbf{R}_I - \mathbf{R}_J|} - \frac{\hbar^2}{2m}\sum_i\sum_i \nabla_i^2 + \sum_{i\neq j}\frac{1}{4\pi\varepsilon_0}\frac{e^2}{|\mathbf{r}_i - \mathbf{r}_j|} - \sum_{i,I}\frac{1}{4\pi\varepsilon_0}\frac{Z_I e^2}{|\mathbf{r}_i - \mathbf{R}_I|} \tag{2.1}$$

Since there is no exact solution to the many-body equation, and brute-force numerical methods are computational impossible for even the largest computing systems, numerous mathematical approaches have been explored to simplify the problem. Often, only the electron-electron interactions are important for magnetism (though this is not always the case). The Kohn-Sham equation provides a method for calculating these interactions by optimising the wavefunction of the electrons according to a reduced Hamiltonian containing only the electron kinetic operator ∇^2 and a parameterised electron potential $V_{\text{eff}}(\mathbf{r})$:

$$\left(-\frac{1}{2}\nabla^2 + V_{\text{eff}}(\mathbf{r})\right)\psi_i(\mathbf{r}) = \varepsilon_i\psi_i(\mathbf{r}) \tag{2.2}$$

which gives a one-electron solution to the many-body Hamiltonian by simplifying the full electron-electron and electron-nuclei Coulomb potential into more solvable solutions given by V_{eff}. The field of Density Functional Theory (DFT) simplifies the problem of variationally optimising the wavefunction by operating on the electron density, given as the sum of the probability density of the occupied wavefunctions $n(\mathbf{r}) = \sum_i |\psi_i(\mathbf{r})|^2$. We can introduce an additional degree of freedom by considering the spin up ($n^{\uparrow}$) and spin down ($n^{\downarrow}$) electrons (as

diagrammed in Fig. 2.1), resolving the probability density as $n^{\uparrow(\downarrow)}(\mathbf{r}) = \sum_i |\psi_i^{\uparrow(\downarrow)}(\mathbf{r})|^2$. The magnetisation density is then defined as:

$$m(\mathbf{r}) = n^{\uparrow}(\mathbf{r}) - n^{\downarrow}(\mathbf{r}). \tag{2.3}$$

and the magnetic moment can be the integrated magnetisation density:

$$\mathbf{m}_i = \int_{\Omega_i} \mathbf{m}(\mathbf{r}) d\mathbf{r}. \tag{2.4}$$

The problem, of course, is that the Kohn-Sham equation written above does not allow for spin up and spin down electrons. Two separate versions of Eq. (2.2) can be written–one for each electron channel–but without an energetic distinction between spin up and spin down electrons, they will give identical solutions. The integral above gives the entire magnetic moment, but sometimes it can be useful to decompose $\mathbf{m}_i$ into the *spin* and *orbital* contributions by summing the spin and orbital operators over the occupied wavefunctions [30]:

$$\begin{aligned} m_s = &\quad \sum_{i,\mathbf{k}} \langle \Psi_{i\mathbf{k}} | \sigma | \Psi_{i\mathbf{k}} \rangle \\ m_l = &\quad \sum_{i,\mathbf{k}} \langle \Psi_{i\mathbf{k}} | l | \Psi_{i\mathbf{k}} \rangle \end{aligned} \tag{2.5}$$

Fundamental to the DFT process is identifying the necessary changes to the effective potential in Eq. (2.2) to give a one-electron solution based off many-electron interactions. Hartree-Fock formalism models the electrons interacting with a "mean field" approximation, and gives a Hamiltonian:

$$\left(-\frac{1}{2}\nabla_i^2 + V_{\text{ext}}(\mathbf{r}) + \sum_{i \neq j} \int d\mathbf{r}' \frac{\psi_j^*(\text{x'})\psi_i(\text{x'})}{|\mathbf{r}_i - \mathbf{r}_j|} \right) \psi_i(\text{x}) - \sum_{i \neq j} \int d\mathbf{r}' \frac{\psi_j^*(\text{x}')\psi_i(\text{x}')}{|\mathbf{r}_i - \mathbf{r}_j|} \psi_j(\text{x}) \delta_{ij} = \varepsilon_i \psi_i(\text{x}) \tag{2.6}$$

V_{ext} is the electron-nuclei interaction, and the first integral is the Coulomb potential. But the second integral is the purely quantum mechanical result of exchange energy arising from the Fermion description built into the Slater determinate of Hartree-Fock theory: the electrons have an energetic reason to be in different orbitals with their spin aligned. This obvious preference

towards materials having a magnetic moment is a result of the mean field approximation; it is a limitation of the one-electron wavefunctions that it cannot take into account the response of the other electrons when evaluating its operators. This so named electron "correlation" can result in, among other things, reduction of the magnetisation in a similar manner as lattice orbital quenching. Methods to introduce correlation to the Hartree-Fock method exist (e.g. multi-configurational SCF and coupled-cluster theory [31]), but are untenable for lattice systems and even but the smallest molecules. Instead, the Kohn-Sham Hamiltonian is used, with a less severe restriction to the wavefunction than Hartree-Fock's Slater determinate. Rather than use the "exact exchange" present in Eq. (2.6) (which contains no correlation), a modified–and often phenomenological–functional is used to enforce a mix of exchange and correlation. The V_{eff} in Eq. (2.2) can now finally be defined:

$$V_{\text{eff}}(\mathbf{r}) = V_{\text{ext}}(\mathbf{r}) + \int \frac{n(\mathbf{r}')}{|\mathbf{r}-\mathbf{r}'|} d^3r' + \varepsilon_{xc}[n(\mathbf{r})] + n(\mathbf{r}) \frac{\partial \varepsilon_{xc}[n(\mathbf{r})]}{\partial n(\mathbf{r})} \tag{2.7}$$

where V_{ext} is still the electron-nuclei interaction, the integral is the Coulomb potential, and the last two parts are the exchange and correlation functionals, respectively. Two versions of Eq. (2.7) get defined for spin up and spin down electrons, finally allowing for self-consistent, variational calculations to be made to the electron density representing our magnetisation. Multiple forms of functionals exist, constructed and optimised for different elements, phenomena, and operators, but the motivation remains the same: to calculate something useable by the sciencist.

For the atomistic spin-dynamicist, no *ab initio* constant is more important than the Heisenberg exchange J_{ij} between two interacting spin moments. To describe this system, the Hamiltonian usually avoids dealing with changes to the local magnetic density $\mathbf{m}_i$ from Eq. (2.4), and instead holds the local magnetisation magnitude μ_s constant to deal with the magnetic *orientation* $\mathbf{S}_i$:

$$\mathcal{H} = -\frac{1}{2} \sum_{i \neq j} J_{ij} \mathbf{S}_j \cdot \mathbf{S}_j \tag{2.8}$$

Numerous methods exist to extract this energy, but the precise calculation of these constants is firmly in the realm of *ab initio* rather than ASD. Instead, we acknowledge the limitations

working with the Heisenberg Hamiltonian places on ASD: while all methods to calculate the exchange constant seek to quantify the energetic relationship between spins at sites i and j, the Heisenberg exchange is *inter*-atomic. Sites i, j for J_{ij} are differing atoms, rather than differing electrons, orbitals, or even nuclei location. This is a true approximation only in the sense that the above corrections are usually small compared to the Heisenberg constant, but do express themselves in crucial physics (see [32–36]). In metals the full calculation can take a complex arrangement due to induced-polarisation of the d-orbitals acting non-locally through the conduction band. This so named RKKY theory (for additional *ab initio* background beyond [30] see [37, 38]) explains the AFM ordering typical of layered metals: in general, metals in-plane order parallel; metals out-of-plane order antiparallel. But this is less of a correction to the Heisenberg Hamiltonian than it is an analysis technique.

The largest correction necessary to the Heisenberg Hamiltonian–on the basis of energy rather than fundamental approximations–is the directional variation in J_{ij} at site i independent of j. Often called the magnetocrystalline anisotropy energy (MAE) or magnetic crystalline anisotropy (MCA), this anisotropic preference for the moment is usually treated as a property independent of exchange (i.e., using its own constant k_i rather than J_i). This is especially true for models dealing with larger systems simulating shape effects. For materials with symmetric, strong spin-orbit coupling, it is possible instead to build the anisotropic contribution into an exchange tensor. This adjusts the Heisenberg Hamiltonian slightly to:

$$\mathcal{H} = -\frac{1}{2}\sum_{i\neq j}\mathbf{S}_i J_{ij}\mathbf{S}_j - \sum_i k_i(\mathbf{S}_i \cdot e_i)^n \tag{2.9}$$

where J_{ij}^T is the exchange tensor, k_i is the MCA constant depending purely on i spins, and n is the so-called "anisotropy order" exponent representing the energetic scaling of the anisotropy and spin. Anisotropies which are truly "single-ion" and which belong in the exchange tensor can be difficult to differentiate, even with first principles formalism. d-orbital projections to Cartesian space can introduce additional directional components to the magnetic preference beyond the exchange splitting of interatomic bands. This can take the form of crystal field splitting–localised charge polarisation around the magnetic moment breaking the

orbital symmetry–or spin-orbit coupling. Both sources of anisotropy have a strong lattice symmetry component, allowing for decomposition of the anisotropy constant in (2.9) into a phenomenological description combining both the crystal-field and spin-orbit contributions dependent on symmetry orders [39]. For metals with weak ionic potentials the crystal field splitting is less important than the spin-orbit coupling [29]: the spin-orbit coupling strength ξ is proportional to $dV_{\text{eff}}(\mathbf{r})/\mathbf{r}d\mathbf{r}$, and can be on the order of exchange interactions for transition metals (or larger for rare-earth elements) [30]. The spin-orbit interaction $\xi l \cdot s$ must enter into the Kohn-Sham equation effective potential (Eq. (2.7))–usually from a perturbation approach. Then, the spin-orbit coupling (SOC) strength along direction $\hat{\mathbf{n}}$ for spins s, s', on occupied and unoccupied states i, j (respectively), wavefunctoin $\mathbf{k}$, and orbitals l, l' on atom q from other atoms q' is [30]:

$$E^{ss'}_{soc,q}(\hat{\mathbf{n}}) \propto -\sum_{\mathbf{k}ij}\sum_{q'}\sum_{l} \frac{\langle qls|\xi_q l \cdot s|ql's'\rangle\langle q'l's'|\xi_{q'} l \cdot s|q'l's\rangle}{\varepsilon_{\mathbf{k}j} - \varepsilon_{\mathbf{k}i}} \tag{2.10}$$

The value of $\varepsilon_{\mathbf{k}j} - \varepsilon_{\mathbf{k}i}$ weights the contribution of the MAE towards states on opposite sides of the Fermi energy but still close in energy. The MAE is then the difference of orientation energies for all atoms and spins:

$$E_{MAE} \propto \sum_{qss'} E^{ss'}_{soc,q}(\hat{\mathbf{n}}_1) - E^{ss'}_{soc,q}(\hat{\mathbf{n}}_2) \tag{2.11}$$

For systems with strong, ordered spin-orbit interactions or strong applied fields [29], the exchange splitting gets enhanced when aligned to certain directions, making the perturbation approach less-accurate and requiring self-consistent approaches to SOC [40]. In this case, the anisotropic contribution is considered "two-site" [41], and should be considered as part of the exchange tensor [39].

2.1.2 Atomistic Spin Dynamics

Modelling the spin on the atomic scale uses the Landau-Liftshitz-Gilbert (LLG) equation of motion (Eq. (2.12)) for the local moment to describe the precession and damping path in the presence of the local moment's effective field. This motion is a classical derivation, requiring

minimal quantum mechanical routes of energy transfer out of the atomic moment (e.g. through intra-atomic spin transitions). The damping term for the LLG equation, α, represents the atomic preference for the magnetic moment to align with the effective field, rather than precess around it, and is an intrinsic property of materials relating to interactions with the phonon lattice, conduction band, and other magnetic moments. Various theories exist to describe the damping term, but in the LLG equation it is a phenomenological, dimensionless quantity representing the ratio of precession to damping in the system. For metals of high crystalline order and quality, the value can be on the order of 10^{-3}. The LLG equation combines the precession of the moment in the effective field as well as the damping of the spin:

$$\frac{d\mathbf{S}_i}{dt} = -\frac{\gamma_e}{(1+\alpha^2)}\left[\mathbf{S}_i \times \mathbf{B}_i^{\text{eff}} + \alpha \mathbf{S}_i \times \left(\mathbf{S}_i \times \mathbf{B}_i^{\text{eff}}\right)\right] \tag{2.12}$$

The effect of temperature on the motion of the atomic spin is a topic of rich analysis, with ongoing research for many theory and computation groups [42, 36, 43, 44], and the full details are beyond the scope of this thesis. The inclusion of temperature into the LLG equation is done by linking the conduction band heat bath to the effective field of each moment according to dissipation-diffusion theory so the so called Langevin thermostat. The fluctuations of the field from moment-to-moment (2.13) have a Gaussian distribution $\Gamma(t)$ with width determined by the size of the moment μ_s, Gilbert damping parameter α, effective temperature T_{eff}, and the time-step Δt, averaging out to zero for each spin (2.14).

$$\mathbf{B}_i^{therm} = \Gamma(t)\sqrt{\frac{2\alpha k_B T_{\text{eff}}}{\gamma_e \mu_s \Delta t}} \tag{2.13}$$

$$\langle B_i^{therm}(t)\rangle = 0 \tag{2.14}$$

This thermal field is then added to the effective field from the derivative of the Hamiltonian:

$$\mathbf{B}_i^{\text{eff}} = -\frac{1}{\mu_s}\frac{\partial \mathcal{B}}{\partial \mathbf{S}_i} + \mathbf{B}_i^{therm} \tag{2.15}$$

To solve the LLG equation, we utilise an explicit 2$^{\text{nd}}$ order Runge-Katta integration scheme with predictor-correction step (i.e. the Heun integrator) due to its computational performance and convergence with the fluctuation-dissipation formulation of the stochastic thermal fields [30]. This involves a two-step solution to the EoM with a normalisation step between each to preserve the spin length [45]:

$$\text{1a. } \Delta\mathbf{S}_i = -\frac{\gamma_e}{(1+\alpha^2)}\left[\mathbf{S}_i \times \mathbf{B}_i^{\text{eff}} + \alpha\mathbf{S}_i \times \left(\mathbf{S}_i \times \mathbf{B}_i^{\text{eff}}\right)\right]$$

$$\text{1b. } \tilde{\mathbf{S}}_i' = \mathbf{S}_i + \Delta\mathbf{S}\Delta t$$

$$\text{1c. } \mathbf{S}_i' = \tilde{\mathbf{S}}_i'/|\tilde{\mathbf{S}}_i'|$$

$$\text{2a. } \Delta\mathbf{S}_i = -\frac{\gamma_e}{(1+\alpha^2)}\left[\mathbf{S}_i' \times \mathbf{B}_i'^{\text{eff}} + \alpha\mathbf{S}_i' \times \left(\mathbf{S}_i' \times \mathbf{B}_i'^{\text{eff}}\right)\right]$$

$$\text{2b. } \tilde{\mathbf{S}}_i^{t+\Delta t} = \mathbf{S}_i + \frac{1}{2}\left[\Delta\mathbf{S}_i + \Delta\mathbf{S}_i'\right]\Delta t$$

$$\text{2c. } \mathbf{S}_i^{t+\Delta t} = \tilde{\mathbf{S}}_i^{t+\Delta t}/|\tilde{\mathbf{S}}_i^{t+\Delta t}|$$

A well-known phenomenon of the Langevin thermostat is to overestimate the thermal activation at low temperatures. Corrections to this effect are varied, and likewise outside the scope of this thesis [42, 46]. We use the method by Kuz'min to adjust the effective temperature of the spin activation by the ratio of the material temperature relative to the Néel temperature. This rescales the Curie-Bloch law to include an additional exponent term, where α_{CB} is the phenomenological rescaling exponent (different from the atomistic Gilbert damping term in the LLG equation above), T_N is the Néel temperature, and β is the usual Curie-Bloch critical exponent for a 3D Heisenberg spin [47]. This rescaling is performed for all simulations with finite temperature:

$$\frac{T_{\text{eff}}}{T_N} = \left(\frac{T_{\text{real}}}{T_N}\right)^{\alpha_{CB}} \tag{2.16}$$

where T_{eff} is the rescaled thermodynamic temperature for the spin, T_N is the Néel temperature, and T_{real} the desired simulation temperature, which differs from the effective temperature of the spin bath. This approximates the correction to the system necessary for quantum thermodynamics without the need for the magnon spectra of the material [48, 46]. This introduces an additional exponent for the standard Curie-Bloch law:

$$m_e(T) = m_e(0)\left[1 - \left(\frac{T_{\text{real}}}{T_N}\right)^{\alpha_{CB}}\right]^{\beta} \tag{2.17}$$

2.1.3 Energy Landscape

The energy landscape of the spin system can be further explored using a Monte Carlo (MC) Metropolis simulation. There, the temperature enters into the Boltzmann energy of the move-step–rescaled by Eq. (2.17)–and the state of the system is revealed through sampling of the MC simulation after sufficient time-steps have passed to ensure equilibrium has been reached [45]. The MC simulation makes direct use of the Heisenberg Hamiltonian to calculate the energy difference between two spin positions $\Delta E = \mathcal{H}(\mathbf{S}_i') - \mathcal{H}(\mathbf{S}_i)$. The probability for switching is then:

$$P = \exp\left(-\frac{\Delta E}{k_B T_{\text{eff}}}\right) \tag{2.18}$$

Generation of the trial spin state $\mathbf{S}_i'$ is determined through a modified Hinke-Nowak algorithm which combines spin-flip, random-spin, and small-angle changes to efficiently sample the full phase space, including an adaptive angle rate to speed up convergence for high temperature systems [49]. The small-angle change is proportional to the effective temperature of the system:

$$\mathbf{S}_i' = \frac{\mathbf{S}_i + \sigma\Gamma}{|\mathbf{S}_i + \sigma\Gamma|} \tag{2.19}$$

where σ is the cone width scaled by a Gaussian distribution Γ. The cone width can be adjusted by an additional multiplicative factor f such that, if the total rate of success of the Boltzmann probability in Eq. (2.18) R differs from 50%, the width σ can be scaled by $f = 0.5/(1-R)$.

This has been shown to improve the MC performance for systems operating near 0 K and T_N regions [49]. The width of σ then is given as:

$$\sigma = f\frac{2}{25}\left(\frac{k_B T_{\text{eff}}}{\mu_B}\right)^{1/5} \tag{2.20}$$

The MC algorithm can also be used to sample the energy landscape of constrained systems in order to explore high-energy configurations. The so-called Constrained MC (CMC) technique establishes thermodynamic equilibrium for the system at the simulated temperature and constraint configuration [50, 49], and is especially useful for modelling the torque response at certain spin angles for a range of temperatures in order to calculate the anisotropy scaling effects with increasing temperature. Likewise, the CMC simulation is also used to calculate the effective torque response over a range of temperatures on a constrained spin-spiral. This method gives a value of the exchange scaling with temperature. There, the spin steps in Eq. (2.19) are evaluated by an additional criteria that the total magnetisation for a given subset of the full spin system $\hat{\mathbf{M}}_j \equiv \sum_j \mathbf{S}_j / |\sum_j \mathbf{S}_j| \approx \hat{\mathbf{M}}_j^{\text{constraint}}$. Spins outside the subset j are evaluated using the standard criteria Eq. (2.18) and spins inside the subset j under a new probability criteria [50]:

$$P^j = \left(\frac{\hat{\mathbf{M}}'}{\hat{\mathbf{M}}}\right)^2 \frac{|\mathbf{S}_j|}{|\mathbf{S}'_j|} \exp\left(-\frac{\Delta E}{k_B T_{\text{eff}}}\right) \tag{2.21}$$

This allows microscopic equilibrium of the subset for a given temperature. Specific details for the subsets and constraints in the CMC simulations utilised in Chapter 5 are given there.

2.1.4 Dynamic Temperature

Dynamically, laser excitation causes changes to the temperature of the magnetisation heat bath on the ultrafast timescale. This is included through the use of the "two temperature model"[1], applicable for transition row metals. Since the heat bath coupling to the magnetic spin in metals

[1] A popular microscopic model of ultrafast demagnetisation from thermal processes is the three temperature model, which adds an additional degree of freedom for the magnetisation coupling through the spin temperature of the system [51, 52]. For atomistic simulations, the need for a microscopic spin bath is replaced by the natural excitation of the LLG equation by the Langevin thermostat.

occurs through the electron system, which has a much lower heat capacity than the phonon lattice, the magnetisation experiences a transient temperature peak before cooling to match the phonon temperature. Often, this transient heating can raise the temperature above the Néel temperature–on the order of picoseconds–causing sharp reduction in the system magnetisation without fully causing a phase change to the paramagnetic state. For longer timescales–on the order of tens of picoseconds–the metal thin film cools to the temperature of the insulating substrate through phonon coupling.

The energy added to the system from a laser excitation of a Gaussian temporal profile with full width at half height t_p is [53]:

$$S(t) = 2\frac{F}{t_p \delta \sqrt{\pi/\ln 2}} \exp^{-4\ln 2\left(\frac{t}{t_p}\right)^2} \tag{2.22}$$

where F is the fluence of the laser pulse in J/m^2 and δ is the thickness of the film. A full description of the laser heating includes a height-dependence impacted by the attenuation of the laser. Provided the thermal conductivity of the material is high and the film is thin, the temperature of the system can be assumed independent of depth. For complex relationships between the intensity of the laser pulse and the heating of the electron thermostat, a more involved expression for $S(z,t)$ and F is required.

The time-dependent temperature of the system is given in the coupled differential equations for energy transfer between the electron temperature T_e and phonon temperature T_p (with cooling to the substrate temperature T_s) by the electron-phonon coupling constant G and characteristic cooling time τ_s. In general, these values begin to become temperature-dependent near the Fermi temperature, but in metals this is far above the heating from ultrafast laser excitation. The differing heat capacities for the electrons $C_e = \gamma T_e$ and phonons C_p link the temperature of the two systems in thermodynamic equilibrium through their energy:

$$\begin{aligned} C_e \frac{\partial T_e}{\partial t} &= -G(T_e - T_p) + S(t) \\ C_p \frac{\partial T_p}{\partial t} &= G(T_e - T_p) - \frac{T_p - T_s}{\tau_s} \end{aligned} \tag{2.23}$$

2.2 Atomistic Modelling of Mn_2Au

Mn_2Au is an ordered, bimetallic material with single or multigrain structure [20, 54]. The full Hamiltonian used for Mn_2Au in this thesis contains the exchange tensor, a uniaxial out-of-plane anisotropy term of 4^{th} order, and an in-plane rotational anisotropy term of 4^{th} order. This gives a strong in-plane spin preference, with the four spin easy axes along $\langle 110 \rangle$ (see Fig. 2.3b). θ describes the polar angle from the $\hat{z}$ coordinate, and ϕ the azimuth angle from the $\hat{x}$ coordinate. Then, the *ab initio* Hamiltonian from DFT calculations in Shick *et al.* [41] and Khmelevskyi *et al.* [55] is given as:

$$\mathcal{H} = -\frac{1}{2}\sum_{i<j} J_{ij}\mathbf{S}_i \cdot \mathbf{S}_j - K_2^{\perp}\sum_i \sin^2\theta - K_{4\perp}\sum_i \sin^4\theta - K_{\parallel}\sum_i \sin^4\theta\cos 4\phi \tag{2.24}$$

A thorough discussion of this Hamiltonian and the consequence of its trigonometric descriptions in the anisotropy components is given in Chapter 5, but for now we note there are nuances involved with the above description. The parametrised macroscopic constants $K_2^{\perp}$, $K_{4\perp}$, and $K_{\parallel}$ in Eq. (2.24) we use in our atomistic LLG and MC simulations is given here for immediate reference, with more details in Chapter 5:

$$\mathcal{H} = -\sum_{i\neq j} \mathbf{S}_i \mathbf{J}_{ij}^T \mathbf{S}_j - k_4 \sum_i \left(S_{i,z}^4 - \frac{30}{35} S_{i,z}^2 \right) - \sum_i k_{4r} (S_{i,x}^4 - 6S_{i,x}^2 S_{i,y}^2 + S_{i,y}^4), \tag{2.25}$$

The exchange constant in Eq. (2.25) is now a tensor containing the $K_2^{\perp}$ anisotropic contribution leading to the easy-plane orientation of the spins. This anisotropy is of the two-ion type. The 4^{th} order anisotropies have been written in an orthogonal Cartesian form parametrised as k_4 and K_{4r} to distinguish from the macroscopic constants in Eq. (2.24) (more details in Chapter 5).

The exchange interactions for the unit cell from Khmelevskyi consist of two antiferromagnetic inter-species and one ferromagnetic intra-species term, consistent with RKKY metals. This gives a total of 9 interactions per atom. The groups of Oppeneer and Novak provide long-

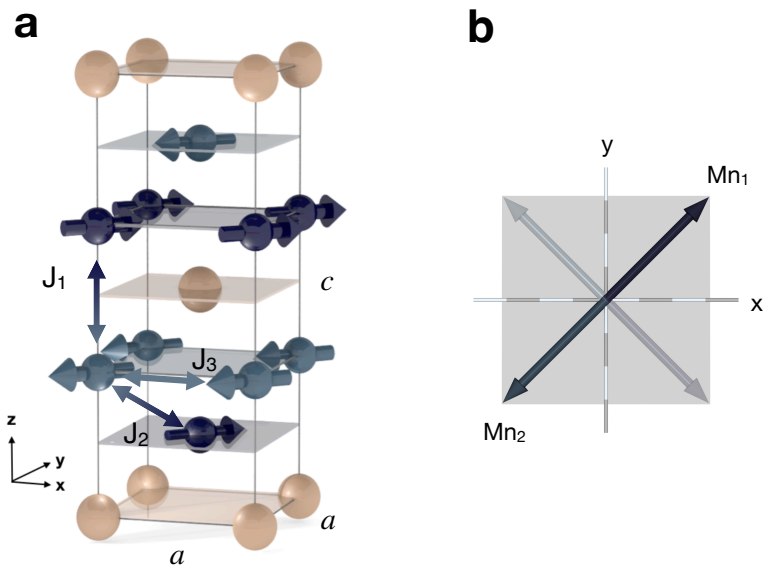

Fig. 2.3 Unit cell with exchange interactions. (a): The tetragonal unit cell has lattice constant $a = 6.291$ along the x and y Cartesian coordinate and $c = 16.142$ along the z coordinate. J_1 and J_2 are the antiferromagnetic inter-species exchange interactions and J_3 is ferromagnetic intra-species interaction. (b): in-plane orientation of spin vectors along $\langle 110 \rangle$ easy axes. Strong AFM coupling ensures a collinear Néel vector along the same. Grey arrows show the Néel vector with 90 degree rotation, equivalent in energy to the starting dark arrows. Cartesian axes x, y are hard axes.

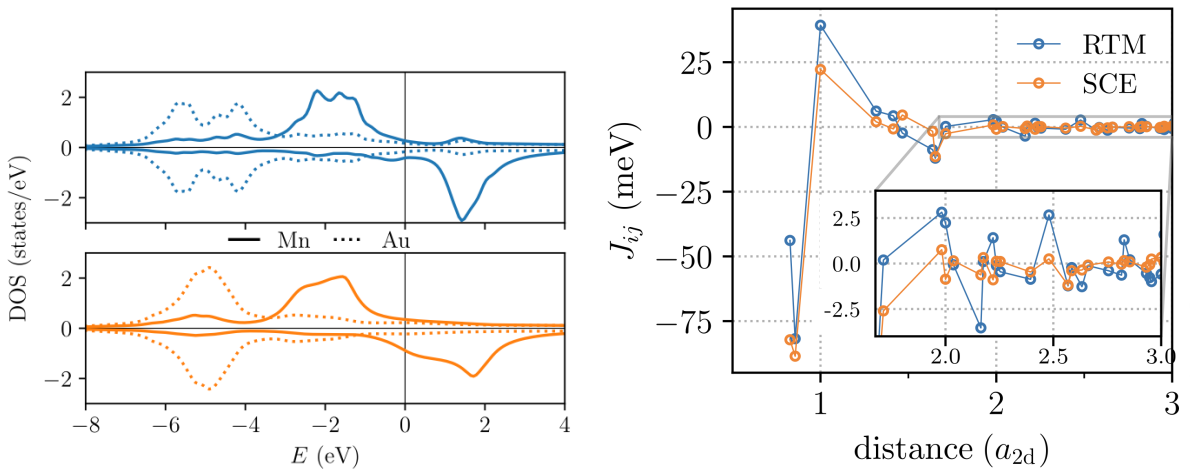

(a) DoS **(b)** Exchange Constants

Fig. 2.4 *ab initio* DoS and exchange constants. (a): Atom resolved DoS in the AFM ground state (top) and the disordered local moment (DLM) state (bottom). (b): exchange constants as function of inter-atomic distance for two DFT methods: (1) relativistic torque method (RTM) and (2) spin-cluster-expansion (SCE) from the DLM reference state. The SCE corresponds to a high-temperature phase (without phonon interactions or lattice expansion). Both figures from [56].

range RKKY exchange up to 9$^{\text{th}}$ order ($\approx$ 1 nm) (Fig. 2.4b)[56], but MC and switching simulations show minimal impact of including these interactions. The SCE constants in Fig. 2.4b correspond to the high-temperature (fully disordered) magnetic phase, and shows the rigidity of the Mn local spin moments (3.71 μ_B vs. 3.74 μ_B) [56]. Likewise, the high-temperature DLM DoS in Fig. 2.4a shows minimal qualitative change compared to the collinear AFM ground state beyond loose thermal broadening. This supports the use of the constants in Table 2.1 even for high-temperature simulations, though no work on spin-phonon coupling or thermal lattice expansion has been done so far on Mn_2Au. The work done by Shick *et al.* find an orbital moment on the Mn sublattices of $\mp 0.013\ \mu_B$ (antiparallel to the spin contribution of the moment). For our atomistic simulations we approximate this to zero [41].

With the Néel temperature of Mn_2Au being above the ordered crystalline point of the material, estimates to the exchange constants are made from a combination of *ab initio* and experimental calculations. Two AFM THz modes (Eqs. (2.26)), as well as single domain wall widths, have been measured, providing upper and lower bounds for the Néel temperature and

rotational anisotropy [57]. We use the exchange values calculated originally by Khmelevskyi [55], though other groups ([58, 56]) have published a range of values consistent with the experimental results. The rotational anisotropy constants from Shick *et al.* (k_{4r}) [41] fit in the middle of the range measured by experiment in Sapozhnik *et al.* [57]. In simulations we also make use of lower bound values from [57] ($k_{4\parallel}$). Both values are used for simulations. Our complete table of values is provided in Table 2.1.

Interactions	J_{xx}	J_{yy}	J_{zz}	Unit
J_1	-1.46923	-1.46923	-1.45932	10^{-20} J/link
J_2	-1.09430	-1.09430	-1.08691	10^{-20} J/link
J_3	0.31826	0.31826	0.31826	10^{-20} J/link
	Parameter	Value		Unit
	μ_s	3.72		μ_B
	$k_{2\perp}$	-1.9727×10^{-22}		J/atom
	k_4	3.710×10^{-25}		J/atom
	$k_{4\parallel}$	1.855×10^{-25}		J/atom
	k_{4r}	8.0255×10^{-25}		J/atom
	T_N	1225		K
	a,c	6.291, 16.142		Å

Table 2.1 Hamiltonian constants

To determine the Néel temperature of our system, we simulate a $(10\,\mathrm{nm})^3$ computational cell with periodic boundary conditions using a standard Monte Carlo Metropolis for calculation of $m_e(T)$. We determine the Néel temperature of 1227 K by performing a Monte Carlo Metropolis simulation and fitting to the modified Curie-Bloch expression (Eq. (2.17)) for the average sublattice magnetization $m_e = (m_1 + m_2)/2$, where $\beta = 0.332 \pm 0.02$ is the high temperature critical exponent and the Bloch exponent $\alpha = 1$ in the classical limit [59, 10]. We then apply the spin temperature rescaling method [59] for $\alpha_{CB} = 2$ as derived from spin wave theory for antiferromagnets and recover a temperature-dependent sublattice magnetisation curve from our semi-classical simulation in very close agreement with neutron scattering measurements [10]. As shown in Fig. 2.5 the fits and data in the quantum cases are in excellent agreement, with the Curie-Bloch equation accurately describing the temperature dependent ordering of Mn_2Au in the full temperature range.

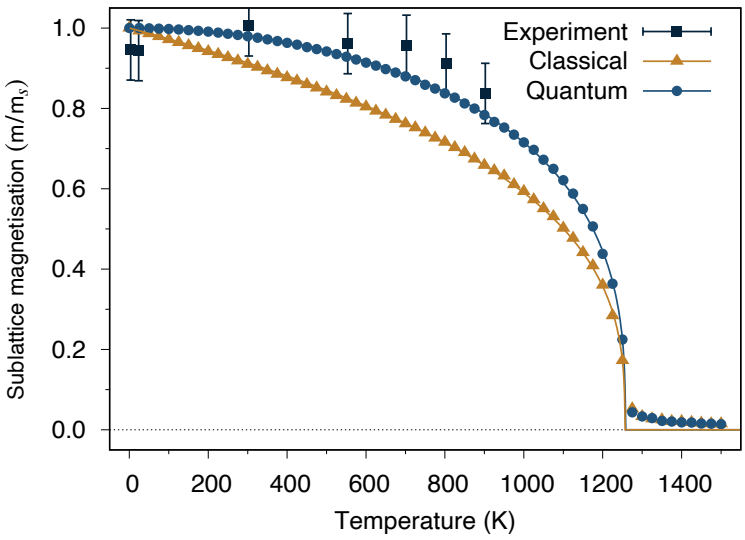

Fig. 2.5 T_N from Monte Carlo simulations. (Classical): sublattice magnetisation with temperature using the unscaled Langevin thermostat. (Quantum): phenomenological temperature rescaling in Eq. (2.17) with $\alpha_{CB} = 2$ showing excellent agreement with the experimental trend over the traditional Lanvegin thermostat.

For simulations with dynamic temperature effect, we utilise the TTM in Eq. (2.23). For simulations where cooling from the substrate is far longer than the timescale of the simulation, we set τ_s in Eq. (2.23) to 0. Constants are from [60] and are consistent with experimental results in [20, 61].

Symbol	Value	Unit
γ	1×10^3	J/K^2 m^3
C_p	6.934×10^6	J/K m^3
G	2.5×10^{17}	J/K m^3
τ_s	20	ps

Table 2.2 Two temperature model parameters.

Of great interest to spintronics is the advent of readily-accessible THz devices and emitters. As a collinear AFM, Mn_2Au has two well described THz modes [62, 63]:

$$\begin{aligned} f_0^\alpha &= \frac{\gamma}{2\pi\mu_s}[2J^{\mathrm{inter}}d_{xy}]^{1/2} \approx 0.85\ THz \\ f_0^\beta &= \frac{\gamma}{2\pi\mu_s}[2J^{\mathrm{inter}}(d_{xy}-d_z)]^{1/2} \approx 2.9\ THz \end{aligned} \tag{2.26}$$

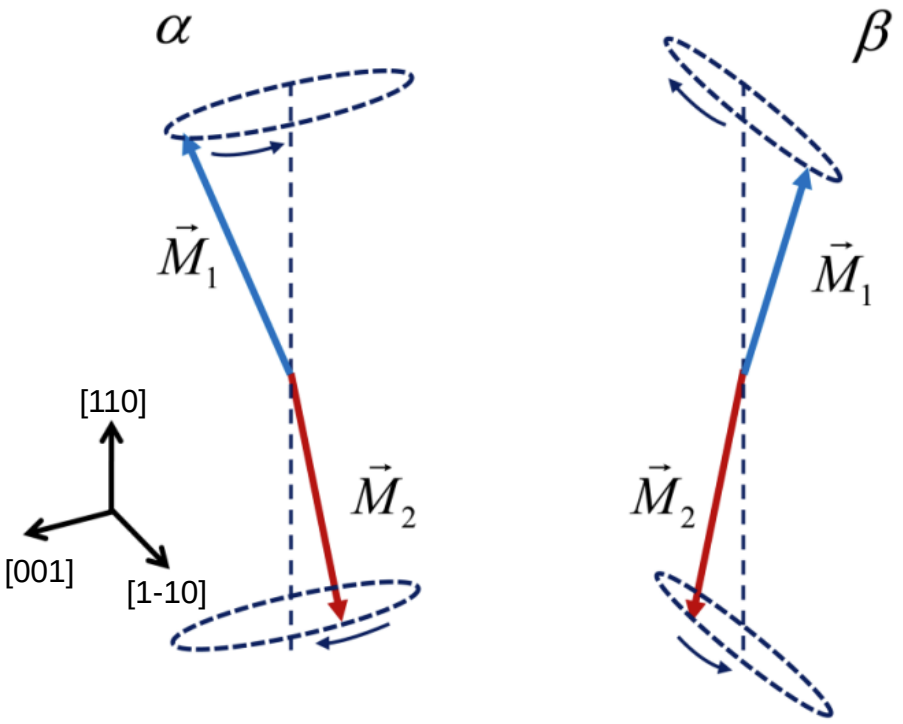

Fig. 2.6 THz modes for collinear, easy plane AFMs. Figure from [62] with coordinate scheme adjusted for specific Mn_2Au symmetry.

where d_{xy} and d_z are the k_{4r} and $k_{2\perp}$ anisotropy constants. The two modes scale with the anisotropy and AFM exchange energies. The lower frequency mode oscillates in the xy-plane (α in Fig. 2.6), while the higher frequency mode has an additional boost from the out-of-plane component activating d_z. In Chapter 5 the presence of a DW shows thermal activation of the anisotropy breathing mode (see Fig. 5.7). ASD simulations have also shown activation of the THz modes in Eq. (2.26) [63, 64]. Experimentally, Mn_2Au THz emissions have been measured from THz excitation [20] and FM bilayer optical excitation [65].

3

Laser Optical Torque Switching

3.1 Introduction

The potential for fast, deterministic control of the order parameter in metallic antiferromagnets (AFMs) at room-temperature without heavy-metal spin injection is highly promising for spintronics research and device applications. Currently, the most understood method for controlling the AFM order parameter in Mn_2Au devices is the application of spin orbit torque (SOT) [66, 19, 67, 68]. But also of interest is the use of spin transfer torques (STTs) [69, 63, 70, 71] and THz excitations to drive AFM switching [20]. However, limitations to these novel methods provide challenges for practical implementation: SOT control using applied currents requires either precise timing to prevent over-switching [72, 69, 18], weaker fields for longer duration [27], or repeated short pulses [13, 73]. STT driven switching requires complex heterostructures [63, 18, 65], and over-shooting beyond 90-degrees is still a risk [69, 63]. THz driven dynamics represent the most precise method of control, but have not been shown to switch the AFM Néel vector with the current experimental THz excitation strength [20]. The ultrafast control of magnetism using laser excitation started with the seminal work of Beaurepaire and Bigot and their demagnetisation of Ni [74]. Since then, all-optical control has been demonstrated in a host of systems using ultrafast heating to switch FM domains ([75, 76] to cite only a few). For ultrafast control of AFMs using optical frequency laser pulses, domain switching has been limited to classes of insulating rare-earth orthoferrites at extremely low

temperatures [8, 77, 26]. So far for metallic AFMs, optical control has been limited to THz excitations [20, 78–80].

Recent *ab initio* work [25] has presented a new option for direct manipulation of the order parameter in metallic Mn_2Au AFM: the induction of *staggered* fields using direct optical laser excitation. The production of staggered fields is crucial for efficient switching in AFMs, as it cants the AFM sublattices, generating a much larger in-plane torque which switches the Néel vector, rather than relying on the laser induced torque itself to switch the magnetisation. The experimental evidence for these torques in metals has been seen in ferromagnetic (FM) materials [71, 81], but only recently has the same theoretical formalism [24] been applied to AFMs [82] (and specifically Mn_2Au [25, 83]). The frequency dependence of the induced staggered magnetic fields is calculated for optical and THz excitations, and is shown to generate a net non-staggered torque (see Fig. 3.1). We demonstrate through atomistic spin simulations that this torque could potentially switch the AFM order parameter.

This chapter presents atomistic spin dynamics simulations of an optical frequency excitation from ultrafast laser pulses on Mn_2Au using the coupling scheme suggested in Freimuth *et al.* [25]. To distinguish between other laser induced torques acting through spin transfer techniques or THz frequency excitation, we call this generated torque a laser optical torque (LOT). Recently, experiments using ultrafast THz pulses have demonstrated induced Mn_2Au dynamics, with modelling predicting the potential for coherent domain switching [20]. Unlike THz pulses, which are predicted to induce both LOT and SOT fields [25], the optical frequency is too far above the AFM frequency ($\approx 1-15$ THz [20, 65, 63]) to excite SOT dynamics. Thus, we focus our work here on demonstrating the possibility to switch the Néel vector in AFMs using purely LOTs in optical frequencies. Additionally, we provide a method using the LOT symmetry to preferentially control the switching direction of the Néel vector, allowing for deterministic, non-toggle all-optical switching (AOS) in AFMs.

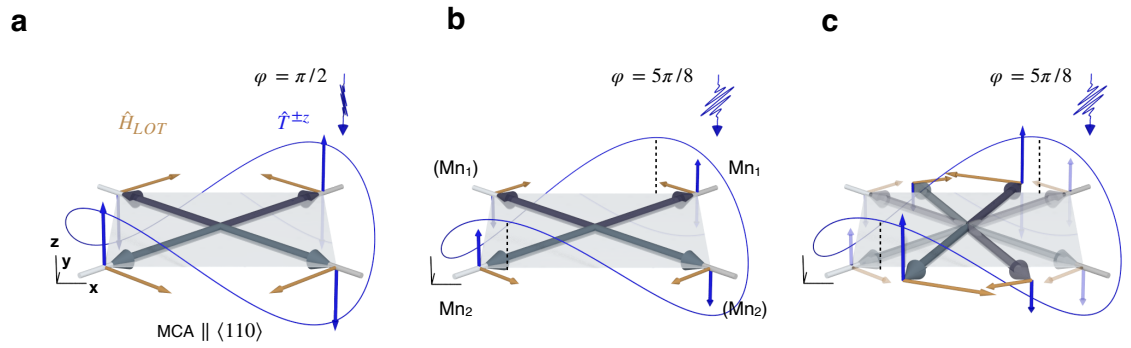

Fig. 3.1 Diagram of net torques from Eq. (3.8) with linearly polarised light parallel to the azimuthal angle φ from x and fourth order in-plane magneto-crystalline anisotropy (MCA) along $\langle 110 \rangle$. (brown/green): magnetisation vector for Mn_1 (Mn_2) sublattice, (gold): induced field, (blue): resultant torque. (blue curve): relative magnitude and sign of LOT, (dashed line): guide to eye for maximal torque location. (a): electric field of laser polarised along y axis. (b): electric field polarised along $\varphi = 5\pi/8$ axis. (c): electric field polarised along $\varphi = 5\pi/8$ with Mn magnetisation sublattices further along rotation path. Note: an electric field of the laser polarised along x will produce equal and opposite torques to the polarisation in (a). For consistency we use the polarisation in (a) in our *easy axes* simulations.

3.2 Methodology

3.2.1 Atomistic System

We perform atomistic spin dynamics simulations in Mn_2Au AFM based on the Landau-Lifshitz-Gilbert (LLG) equation using the open source code VAMPIRE [45] where we included new LOT torques. Unless specified, for the majority of simulations we use a cubic crystal lattice of 1600 spins with periodic boundary conditions (10 x 10 x 4 unit cells). Fig.2.3 illustrates the Mn_2Au unit cell implemented in the atomistic simulations. The effective Heisenberg spin Hamiltonian (Eq. (2.25)) includes the ferromagnetic (FM) and antiferromagnetic (AFM) exchange interaction terms, two-ion anisotropy mediated by the Au sublayers, fourth-order out-

of-plane anisotropy, and the fourth-order rotational in-plane anisotropy (easy axes orientated along the $\langle 110 \rangle$ directions).

The local magnetic moment directions are given by unit vectors $\mathbf{S}_i$ with length μ_s. θ gives the polar angle of magnetisation, and ϕ the azimuthal angle of magnetisation from the x-coordinate. Table 2.1 summarizes the parameters used in the simulations. Shick *et al.* [41] discussed situations where thin films of Mn_2Au have an additional, in-plane, uniaxial strain anisotropy creating a preferential 180-degree orientation along the $[\pm 100]$ or $[0 \pm 10]$ directions (depending on the strain vector). While SOTs/STTs have been simulated to switch 180-degree domains in Mn_2Au [72, 63], we confine our simulations to 90-degree domains without the additional strain anisotropy.

3.2.2 Torque Constant from Susceptibility Tensors

Optically-induced torques show strong crystal symmetry and frequency-dependent coupling to the polarised electric field components of the laser. A full analysis of the symmetry requirements in the Mn_2Au bulk crystal was previously presented by Freimuth *et al.* [25] based on the Keldysh non-equilibrium formalism. There, a linearly or circularly polarised laser pulse was shown to be capable of inducing a torque acting on the Néel vector parameter $\boldsymbol{L}$ via staggered magnetic fields induced by the second order electric field coupling, which act on the Mn spins in the distinct sublattices of the AFM. The magnitude and spatial symmetry of the predicted torque depend both on the local orientation of the Néel vector $\boldsymbol{L}$, as well as the electric field $\boldsymbol{\varepsilon}$ direction of the applied optical pulse. Both in-plane and out-of-plane torques are allowed by symmetry, but only the out-of-plane torque takes advantage of exchange enhancement to drive precessional switching. To achieve magnetic switching using an in-plane torque, the induced field must be at least equal to the in-plane rotational anisotropy field value of 10.3 mT [72]. Assuming a constant linear relationship between torque and laser intensity, this would require pulses on the order of 2000 mJ/cm^2, which would damage and ablate the sample. Thus, this work seeks to apply out-of-plane torques to take advantage of the exchange enhancement characteristic of antiferromagnetic switching [72, 18].

The second order optical effects are generated by oscillating electric field with frequency ω and polarisation ε. Then, the corresponding perturbation to the Kohm-Sham Hamiltonian is [24, 25]:

$$\delta H(t) = e\mathbf{v}\cdot\mathbf{A}(t) \tag{3.1}$$

where e is the elementary charge, $\mathbf{v}$ is the velocity operator, and

$$\mathbf{A}(t) = \mathrm{Re}\left[\frac{E_0\varepsilon e^{-i\omega t}}{i\omega}\right] \tag{3.2}$$

E_0 is assumed to be real valued, but the light polarisation vector ε may be complex, describing circularly polarised light. The electric field of the laser is then:

$$\mathbf{E}(t) = -\frac{\partial\mathbf{A}(t)}{\partial t} = \mathrm{Re}[E_0\varepsilon e^{-i\omega t}] \tag{3.3}$$

In general the time varying second-order susceptibility of the spin $\mathbf{S}_i$ to the electric field is:

$$\delta\mathbf{S}_i(t) = \chi_{ijk}E_i(t)E_j(t) \tag{3.4}$$

where j,k indices on the right-hand-side are the vector components of the electric fields. Already, this suggests the possibility for a time-constant component to the susceptibility through the expansion:

$$E_i(t)E_j(t) = \frac{E_0^2}{2}[\varepsilon_i\varepsilon_j^* + \varepsilon_i^*\varepsilon_i + \varepsilon_i\varepsilon_j e^{-2i\omega t} + \varepsilon_i^*\varepsilon_j^* e^{2i\omega t}] \tag{3.5}$$

In the Keyldish nonequilibrium formalism, the torque T_i is then:

$$T_i = \frac{a_0^3 I}{c}\left(\frac{\mathcal{E}_H}{\hbar\omega}\right)^2 \mathrm{Im}\sum_{jklm}\chi_{ijklm}\varepsilon_j\varepsilon_k^* L_l L_m \tag{3.6}$$

where $a_0 = 4\pi\varepsilon_0\hbar^2/(me^2)$ is the Bohr radius, ε_0 the vacuum permittivity, $\hbar$ the reduced Plank's constant, m the mass of the free electron, c the speed of light, e the fundamental electron charge, $I = \varepsilon_0 cE_0^2/2$ the laser intensity calculated from the electric field component E_0,

$\mathcal{E}_H = e^2/(4\pi\varepsilon_0 a_0)$ the Hartree energy, ε_j the jth Cartesian component of the electric field and L_j the jth Cartesian component of the Néel vector, and χ_{ijklm} the corresponding susceptibility components. The torque value in Eq. (3.6) above follows the same format as the second-order susceptibility in Eq. (3.4), but with the additional degree of freedom depending on the direction of the Néel vector. Importantly, the induced torque sums as the square of the vector components for ε_j and L_m, so the resultant symmetry of the torque can be non-trivial for laser polarisations not along the Cartesian basis vectors or the magnetisation easy axes. The Cartesian vector components of $\boldsymbol{\varepsilon}$ and $\boldsymbol{L} = (\sin\theta\cos\phi, \sin\theta\sin\phi, \cos\theta)^T$ (we will use φ as the azimuthal angle from x for the laser polarisation and the azimuthal angle of the Néel vector as ϕ).

Freimuth *et al.* [25] present thirty susceptibility tensors χ_{ijklm} which are allowed by the Mn_2Au orbital symmetry and which produce a torque perpendicular to the Néel vector (i.e., induce a field not parallel to the sublattice magnetisation). Since Mn_2Au has in-plane magnetisation, we disregard tensors corresponding to an out-of-plane Néel vector component to good approximation ($m_z/\mu_B < 10^{-2} even during canting$). Since we are interested in exchange enhanced precessional switching, we choose a laser geometry with the generated torque to be out-of-plane; Freimuth *et al.* find that light incident normal to the AFM plane with electric field linearly polarised parallel to the in-plane angle φ produces the largest torque values. This geometry reduces the set of thirty tensors to two (tensors 4 and 24 in Freimuth *et al.*) (Table 3.1). The remaining two tensors calculate an identical magnitude, with the total torque being the sum of each tensor.

Tensor	χ_{3jklm}
4	$\langle 32212\rangle - \langle 31112\rangle$
24	$\langle 31211\rangle - \langle 32122\rangle$

Table 3.1 5th rank susceptibility tensors. Note: the i index for the susceptibility tensor χ_{ijklm} is shown here as 3, corresponding to an out-of-plane torque to take advantage of the efficient exchange enhancement switching.

The different polarisation and Néel vector dependencies are parametrised according to the Cartesian vector components, such that

$$
\begin{aligned}
4 \equiv & \mathcal{T}_3\left(\langle 32212\rangle - \langle 31112\rangle\right) \approx \mathcal{T}_3\left(\sin(\varphi)^2\cos(\phi)\sin(\phi) - \cos(\varphi)^2\cos(\phi)\sin(\phi)\right) \\
& = -\frac{\mathcal{T}_3}{2}\cos(2\varphi)\sin(2\phi) \\
24 \equiv & \mathcal{T}_3\left(\langle 31211\rangle - \langle 32122\rangle\right) \approx \mathcal{T}_3\left(\sin(\varphi)\cos(\varphi)\cos(\phi)^2 - \sin(\varphi)\cos(\varphi)\sin(\phi)^2\right) \\
& = \frac{\mathcal{T}_3}{2}\sin(2\varphi)\cos(2\phi) \\
4+24 \approx & \frac{\mathcal{T}_3}{2}\sin(2\varphi - 2\phi).
\end{aligned}
\tag{3.7}
$$

This allows the full Keyldish expression in Eq. (3.6) to be parametrised using trigonometric relations for the laser polarisation angle φ and Néel vector ϕ as:

$$
\mathbf{H}_{\mathrm{LOT}} = \frac{1}{\mu_s}\mathcal{T}(I)\sin(2\varphi - 2\phi)\hat{z}\times\mathbf{S} \tag{3.8}
$$

The torque constant $T(I)$ used in Eq. (3.8) represents the combination of material and experimental constants given in Eq. (3.6) (which are not affected by the laser intensity, laser polarisation, and Néel vector orientation) and the calcualted value of the susceptibility tensor χ_{ijklm} itself, taken from [25]. For a laser intensity of 10 GW/cm^2 with photon energy 1.55 eV, the torque constant $\mathcal{T}_3 \approx 12\times10^{-24}$ J, for a field value of 145 mT on each spin.

For comparison, we can also consider a sub-optimal switching polarisation geometry with the laser polarisation rotated further along the polar angle: an electric field polarisation along [101], photon energy of 1.55 eV, intensity of 10 GW/cm^2, and Néel vector along $\langle 100\rangle$ produces an *in-plane* torque on each magnetic site of $\approx 10^{-24}$ J ($H_{LOT} = 0.05$ mT) [25].

The directions of the induced fields for various light polarisation angles are illustrated in Fig. 3.1. The staggered fields then lead to a non-staggered effective torque. Fig. 3.1a shows the laser polarisation directions corresponding with the maximal torques useful for switching. Fig. 3.1b shows the light polarisation along $\varphi = 5\pi/8$, producing a maximal torque when the Néel vector is off the easy axes. Fig. 3.1c maintains the same polarisation, with the example Néel vectors progressed further along the rotation pathway.

Eq. (3.6) provides a linear relationship with laser intensity. Thus, to simulate the influence of the LOT generated by an ultrafast laser pulse, we scale the laser intensity following a Gaussian time-dependent profile, with the pulse duration $t_p \in [0.02, 6]$ ps giving the time at full-width at half-height of the pulse intensity [53]:

$$\mathcal{T}(t) = \mathcal{T}(I)\exp\left\{-4\ln 2\left(\frac{t-1.5t_p}{t_p}\right)^2\right\}, \tag{3.9}$$

This value is then used to calculate the spin-dependent field in Eq. (3.8) which is then added to the effective field in the LLG equation (2.12).

3.2.3 Discussion on the Origin of the LOT

In the Kohn-Sham framework, the electric field in Eq. (3.3) will induce a change to the spin polarisation quantified by:

$$\delta\mathbf{S} = \int d^3r\,\delta\mathbf{s}(\mathbf{r}) \tag{3.10}$$

where $\delta\mathbf{s}(\mathbf{r})$ is the non-equilibrium spin density. To calculate the resultant torque, the non-equilibrium spin density is crossed with the spin vector $\hat{\mathbf{S}}$:

$$\mathbf{T} = \frac{2\mu_B}{\hbar}\int d^3r\,\Omega^{xc}(\mathbf{r})\,\delta\mathbf{s}(\mathbf{r}) \times \hat{\mathbf{S}} \tag{3.11}$$

However, since $\delta\mathbf{s}(\mathbf{r})$ and the exchange field $\Omega^{xc}(\mathbf{r})$ vary strongly on the atomic scale, it is usually not feasible to calculate the torque directly from the non-equilibrium spin density. Instead, the torque is calculated via lesser Green's function $G^<$ through the operator $\mathcal{T}(\mathbf{r}) = -\mu_B\delta\mathbf{S} \times \hat{\mathbf{S}}\Omega^{xc}(\mathbf{r})$, giving $\mathbf{T} = i\mathrm{Tr}[\mathcal{T}G^<]$ [24].

Qualitatively, the torque operator only measures the *effect* of the non-equilibrium spin density, not the phenomena itself. Thus, while the Keyldish formalism can calculate the resultant torque generated by the laser pulse, the physical origin for the LOT phenomena is still undetermined. Several mechanisms have been discussed: i) optical intersite spin transfer

(OISTR), ii) local ultrafast demagnetisation, iii) SOT induced by charge photocurrents, iv) STT induced by spin photocurrents, and v) inverse Faraday effect (IFE).

While the OISTR can be a critical effect in AFMs [84], in Mn_2Au the LOT excitation energy $\hbar\omega = 1.5$ eV is too small to interact with the bulk of the d-orbitals responsible for the magnetisation (< -2 eV $E - E_F$). As discussed in Chapter 2, the magnetic moment and exchange splitting are highly resistant to the high-temperature, disordered local moment (DLM) calculations [56, 55]. Likewise, the LOT in [25] uses a constant broadening parameter Γ to simulate the steady-state temperature, rather than comparing between the ground state and DLM. This suggests that OISTR and local ultrafast demagnetisation do not contribute to the LOT.

The spin and charge currents induced by linearly polarised optical excitation in Mn_2Au have been investigated in a follow-up study to the work in Freimuth *et al.* [83]. There, the induced *charge* photo current, *spin* photo current, and inverse Faraday effect are analysed for their symmetry properties. The photo currents for charge (propagating along i) and spin (propagating along i with polarisation j) are both effects second-order with the electric field polarisation and first-order in the Néel vector:

$$\begin{aligned} J_i &= \chi^{(4sa)}_{ijkl} E_j E^*_k L_l \\ Q^j_i &= \chi^{(5sp)}_{ijklm} E_k E^*_l L_m \end{aligned} \tag{3.12}$$

where the tensors $\chi^{(4sa)}_{ijkl}$ and $\chi^{(5sp)}_{ijklm}$ include the designation fourth-order staggered axial and fifth-order staggered polar, respectively. This can be compared to the tensor symmetry for the LOT found in [25]: fifth-order axial. Thus, while the charge photo currents and spin photo currents do have allowed torques by symmetry, they do not match precisely the torque symmetries for the LOT.

Lastly, [83] calculate the IFE resulting from laser pulses as the overall induced spin moments in the unit cell. This is reported as the sum of all induced spin moments $\delta\mathbf{S}^+$ and the staggered component of the spin moments $\delta\mathbf{S}^- = \frac{1}{2}[\delta\mathbf{S}(Mn_A) - \delta\mathbf{S}(Mn_B)]$. For a linearly polarised optical frequency ($\hbar\omega = 1.5$ eV) excitation and Néel vector along the easy axis [110], δS^+_z gives a response which changes sign upon 90 degree rotation of the laser polarisation between

$\boldsymbol{\varepsilon} \parallel \hat{x}$ and $\boldsymbol{\varepsilon} \parallel \hat{y}$, with $\delta S_z^- = 0$. When $\boldsymbol{\varepsilon} \parallel \mathbf{N}$ or $\boldsymbol{\varepsilon} \perp \mathbf{N}$, $\delta S_z^+ = 0$, exactly in line with the symmetry of the LOT in Fig. 3.1. This measurement gives the direct change to the spin moments resulting in a canted state, rather than the induced STT or SOT fields generated by the spin photocurrents or charge photocurrents, respectively, in Eqs. (3.12). In other words, the torque response calculated in Eq. (3.6) measures the torque necessary to generate $\delta\mathbf{S}^+$, rather than the torque generated by the canted moments.

The lifetime of the δS_z^+ spin polarisation–represented as the effect of increasing broadening Γ–shows a $\approx \log(\Gamma)$ decay with increasing Γ, rather than the inverse relation seen in $\delta S^+_{\perp\mathbf{N}}$ and $\delta S^+_{\parallel\mathbf{N}}$ (i.e., the in-plane components of the spin polarisation). This indicates the potential for a separate band-dependence excitation for the out-of-plane component of the IFE compared to the in-plane components.

Thus, while the symmetry analysis of the IFE, charge photo currents, and spin photo currents suggests that the IFE is responsible for the LOT, more work remains to be done on the effects of the photo currents on the AFM sublattice.

An additional comment can be made on the torque generated by the non-equilibrium spin density: namely, that it is the *spin* density only contributing to the torque, with no contribution from the orbital moment. Recently, a similar symmetry analysis to the work in [85] was performed for the metallic altermagnet RuO_2 [33] which did include the laser induced orbital contributions, as well as a single element calculation of the laser induced orbital contributions for transition row metals [86]. Both showed large orbital responses to optical frequency light. However, no calculation was performed for the torque generated. [56] estimates the torque from the orbital contribution of the SOT in Mn_2Au (more details in Chapter 6), with the orbital field around five times larger than the resultant spin field. This suggests the orbital component of the non-equilibrium density could have important contributions to both the LOT and orbital photo current excitations.

3.2.4 Laser Heating Temperature Effects

The thermal effects are modelled in the LLG Eq. using the TTM equations detailed in Sec. 2.1 with constants in Sec. 2.2. Fig. 3.2 gives example electron and phonon temperatures and

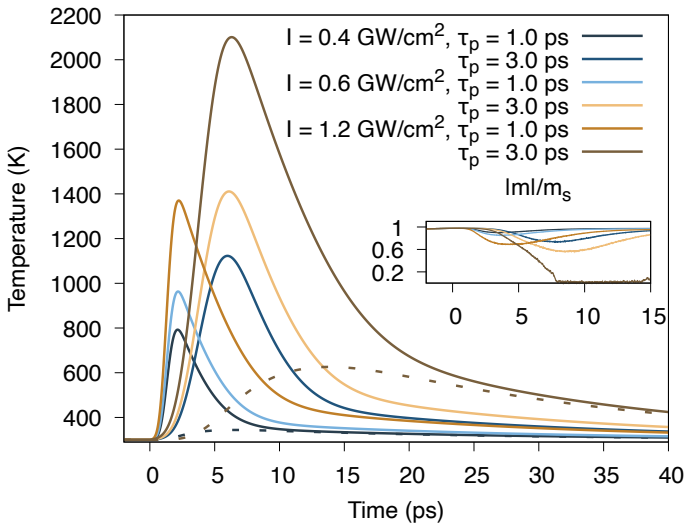

Fig. 3.2 Transient TTM electron and phonon temperature for Fig. 3.9. Inset: corresponding dynamic sublattice magnetisation length. Solid lines are the electron temperature, while the dashed lines are the corresponding phonon temperature (several omitted for clarity).

sublattice magnetisation values for various laser intensities and pulse durations used in the simulations.

The switching probability for simulations above 0 K are calculated using 10 random seed LLG simulations with lattice size 75nm $\times$ 75nm $\times$ 10nm (periodic boundary conditions along x and y) to simulate a thin film single domain structure. The application of the LOT for domain wall driving is studied in Chapters 4, 5, but multi-domain, multi-grain switching with LOT is an area for future research.

The Keyldish formalism in [24, 25] uses a constant broadening parameter Γ to simulate disorder and finite lifetimes from thermal broadening with a $1/\Gamma$ relationship in the susceptibility tensor. A $\Gamma = 25$ meV approximates a clean metallic sample at room temperature, though recent experiments suggest the Γ value for Mn_2Au may in fact be lower [20], leading to a larger torque constant. This value takes into account the non-equilibrium disorder from the laser excitation, so we hold it constant during the simulation. This is a sufficient approximation provided the laser torque is faster than the predominant electron thermalisation (< 1 ps). For longer pulse durations (> 1 ps), a time-dependent broadening parameter may be necessary.

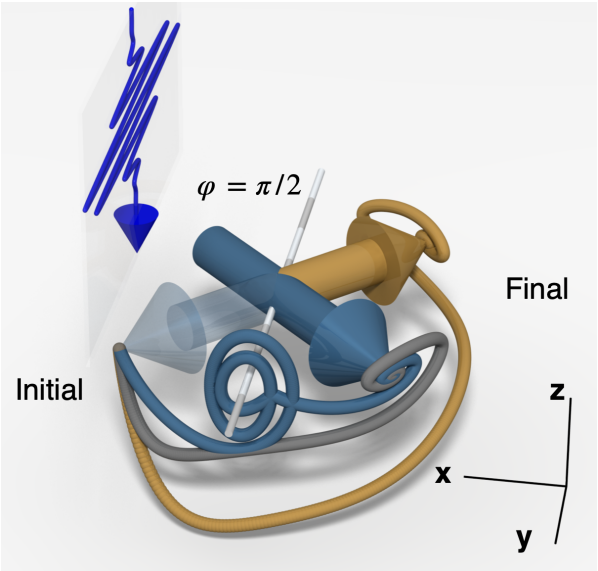

Fig. 3.3 Trace of sublattice magnetisation vectors switching from $[110]$ to $[-110]$ with $\boldsymbol{\varepsilon} \parallel \langle 010 \rangle$. (Opaque): initial orientation. (Bar): precession axis. (grey): $t_p = 400$ fs, $I = 2$ GW/cm^2, (gold): $t_p = 400$ fs, $I = 4$ GW/cm^2, and (blue): $t_p = 3$ ps, $I = 5$ GW/cm^2, $\alpha = 0.001$ (z magnetisation scaled for visibility).

Since a direct relationship between Γ and temperature is unknown, we hold it constant for all simulations.

3.3 Results

3.3.1 Toggle Switching

The LOT modelled by Eq. (3.8) produces 90, 180, and 270-degree precessional switching of the Néel vector in Mn_2Au by *exchange enhancement* generated by the out-of-plane canting as also seen in simulations of the SOT switching [72, 56]. Fig. 3.3 provides example of sublattice magnetisation traces for 90 (grey and blue) and 180-degree (gold) switching. The initial laser induced field causes an out-of-plane canting of the magnetisation, generating a large non-staggered torque on the magnetisation sublattices to rotate the Néel vector.

We model the action of the LOT using four sequential pulses 400 fs long and 8 ps apart for laser intensities $I = 2$ GW/cm^2 ($H_{max} = 42$ mT; blue) and $I = 4$ GW/cm^2 ($H_{max} = 84$ mT; gold). Each consequent pulse produces switching, as shown in Fig. 3.4. Note the

absence of the L_z component; i.e. the Néel vector is rotated in-plane as also typical for the SOT switching [20]. Unlike the SOT considered in [72, 27], the LOT has the additional feature of changing sign during the switching: the intrinsic spatial symmetry defined in Eq. (3.8) ensures the induced LOT changes its sign for any 90-degree rotation of the Néel vector. This allows for both clockwise and counter-clockwise switching by means of the same laser polarisation, i.e. *toggle switching* (see Fig. 3.4) reminiscient of the AOS switching seen from ferrimagnetic thing films [75]. In contrast is the SOT torque, where the direction of the applied current needs to be constantly inverted to change the handedness of rotation for 90-degree switching [13, 20].

180-degree switching is possible with LOT for the same laser polarisation used to generate 90-degree switching, but with strong enough intensities capable to induce larger out-of-plane canting, providing more exchange enhanced torque for the Néel vector rotation (compare the magnitude of the torques in (b) and magnetisation in (d) of Fig. 3.4). The 180-degree switching events are in the same direction, consistently inducing an out-of-plane magnetisation with the same sign.

Fig. 3.5 presents the switching phase diagrams as a function of laser intensity and duration for two Gilbert damping parameters $\alpha = 0.001$ and $\alpha = 0.01$. The colour variation shows intervals of 90-degree switching, typical for precessional switching. Importantly, the switching can be produced by ultrafast laser pulses of several picosecond duration and even below. The absorbed fluence of the sample is approximately linear with intensity and pulse duration [24, 83]. Remarkably, we observe an absorbed fluence of 0.5 mJ/cm^2 ($I = 0.3$ GW/cm^2, $H_{crit} = 6.34$ mT) is sufficient to induce switching on the sub-picosecond timescale for the smaller damping value of $\alpha = 0.001$. Increasing the damping parameter shows a linear dependence in the critical field (see Fig. 3.5b), commensurate with the theory of SOT switching [27].

Analytically, the dynamic behaviour of collinear AFMs under staggered in-plane SOT fields is discussed in [72]. Here, the critical field (H_{crit}) for switching has been shown to depend on the characteristic exchange, anisotropy, and induced magnetic fields. Following the method of [72] - modified for the LOT induced field - the dynamics of the Néel vector in the xy plane can be described by the following equation:

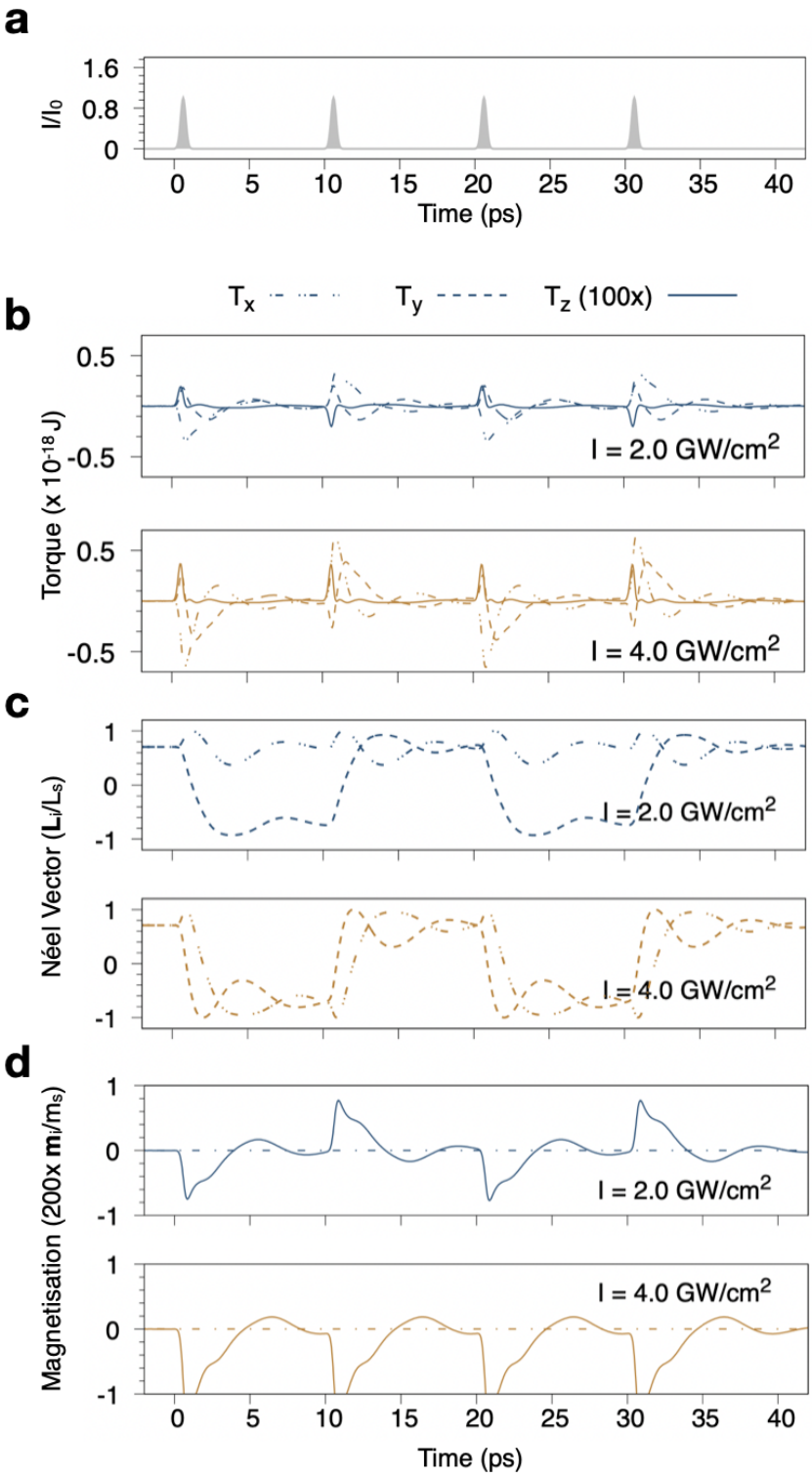

Fig. 3.4 Toggle switching of the Néel vector with multiple optical pulses (a): laser intensity of the pulse (400 fs) 8 ps apart. (b): total torque. Note that the T_z has been scaled 100x for visibility. (dashed): T_x; (dot-dashed): T_y; (solid): T_z. (c): x and y Néel vector components $\boldsymbol{L}_i = (\boldsymbol{m}_1 - \boldsymbol{m}_2)/2$. $L_s = \mu_B$. (dashed): ; (dot-dashed): L_y. (d): Net magnetisation $\boldsymbol{m}_i = (\boldsymbol{m}_1 + \boldsymbol{m}_2)/2$. $m_s = \mu_B$. (dashed): $m_x = m_y$; (dash-dot): m_z (scaled 200x for visibility). Blue lines show 90-degree toggle switching for four sequential pulses. Gold shows 180-degree toggle switching for four sequential pulses.

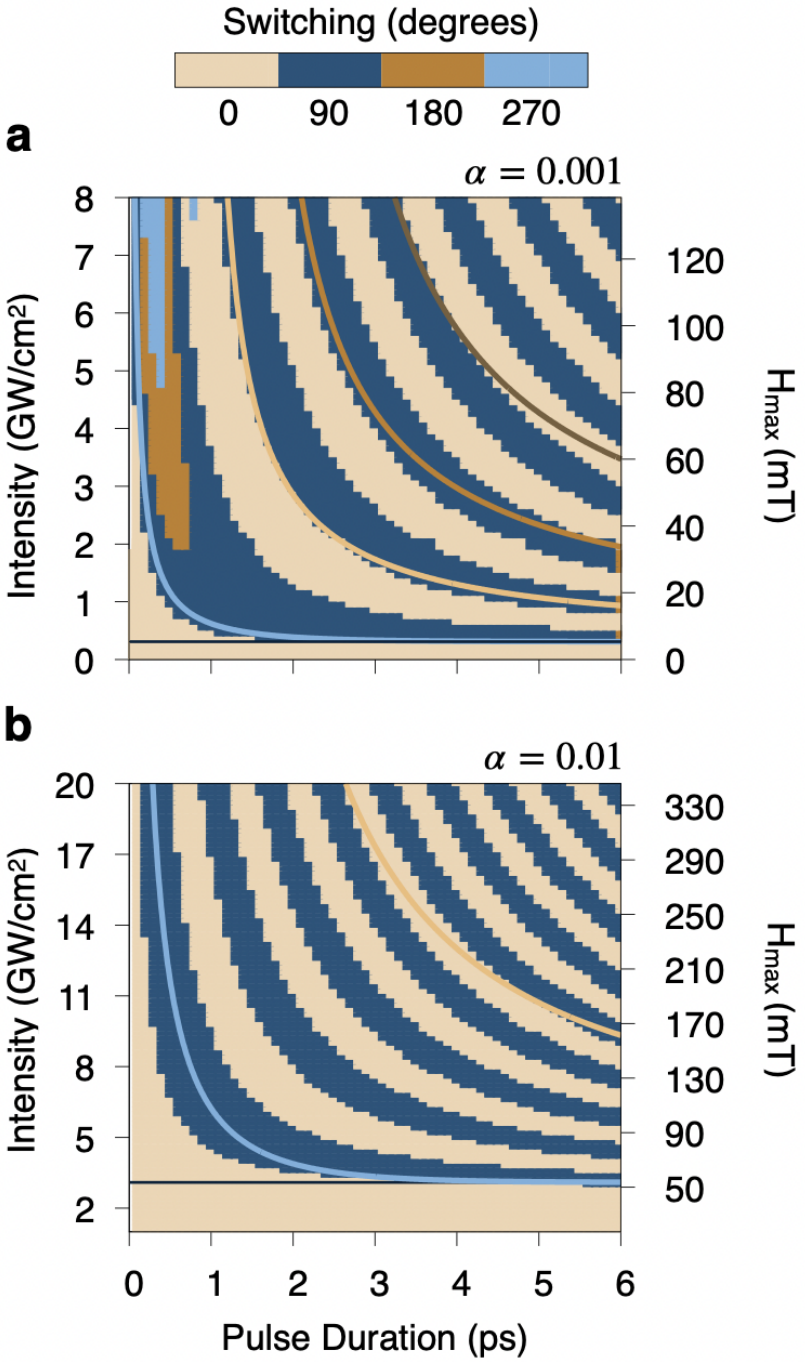

Fig. 3.5 Switching phase diagram in terms of laser intensity and duration. Colours represent the end change of angle from starting orientation along [110]. The corresponding maximum field strength for the laser intensity is given on the second y-axis. Solid colour lines show the analytic H_{crit} values from Eq. (3.15) (a) for $\alpha = 0.001$. Black line: $H_{crit} = \omega_{4\parallel}/(2\gamma) = 5.16$ mT. (b) $\alpha = 0.01$ Black line: $10x\, H_{crit}$.

$$\ddot{\phi} + \frac{\omega_R^2}{4}\cos 4\phi - \gamma\omega_e \frac{\tau(I,\omega)}{\mu_s}\sin(2\varphi - 2\phi) + 2\alpha\omega_e\dot{\phi} = 0 \tag{3.13}$$

where $\omega_e = |5(J_1 + 4J_2)|\gamma/\mu_s$ is the AFM exchange frequency (ignoring the 2-ion anisotropy term to good approximation), $\omega_{4\parallel} = 2\gamma k_{4rot}$ is the fourth order in-plane anisotropy frequency, α is the atomistic damping parameter, γ is the gyromagnetic ratio, and $\omega_R = \sqrt{2\omega_e\omega_{4\parallel}}$. The parameter $\tau(I,\omega)/\mu_s$ corresponds to the amplitude of the LOT field. If the Néel vector is only considered in the interval of its azimuthal angle $\phi \in [0, \pi/4]$, the critical field for infinitely long pulse lengths is $H_{crit} = \omega_{4\parallel}/(2\gamma)$: a factor of 2 larger than for SOT [72, 27], due to the $\sin 2\phi$ dependence of the LOT field. Analytically, our constants predict an $H_{crit} = 5.16$ mT, matching well with our simulations (see horizontal line in Fig. 3.5a).

For short pulse lengths the critical switching field can be evaluated as

$$\frac{H_{crit}}{H_{crit}(\tau \to \infty)} = \coth\left(\frac{2t_p}{\tau_e\sqrt{2\pi}}\frac{\omega_R}{\omega_e}\right), \tag{3.14}$$

where $\tau_e \approx \pi/(2\omega_e)$ is the timescale of the exchange interaction (characteristic precessional time for the Néel vector for rotation over 90-degrees), which is then scaled in Eq. (3.14) by $\sqrt{2\pi}/2$ to account for the Gaussian profile of the laser pulse. Then, τ_p can be called the characteristic pulse duration $\tau_p = 2\tau_e\omega_e/\omega_R$ such that $\coth(2) \approx 1$ [72, 27].

Importantly, only for high intensities and short pulse duration is the inertia generated by the exchange torque susceptible to overshooting, either to the $[-1-10]$ (180-degrees) or even $[1-10]$ (270-degrees) states (orange and light blue colour in Fig. 3.5). Qualitatively, this is illustrated by the gold track in Fig. 3.3 For pulse lengths beyond 1 ps: rather than continually drive the precessional switching using exchange enhancement, the long pulse duration has the Néel vector precessing along the laser polarisation axis (blue curve in Fig. 3.3). The timing of these precessions follows the characteristic exchange period, and can be modelled by modifying Eq. (3.14) to take into account the additional precessions around the LOT polarisation vector: for n precessions, the minimum pulse time to switch the Néel vector at high intensity is proportional to the exchange precession timescale and precession number, $4n\tau_e\sqrt{2\pi}$. This gives a rough approximation to the critical field and laser pulse time:

$$H_{crit}(\tau,n) = nH_{crit}^{\tau\to\infty}\coth\left(\frac{2t_p\omega_R}{n\tau_e\sqrt{2\pi}\omega_e} - \frac{4n\tau_e\sqrt{2\pi}}{t_p}\right) \tag{3.15}$$

The analytical estimates of fields and pulse durations are presented in Fig. 3.5a), showing a good agreement for $n \leq 3$ with the lowest damping value, especially considering the approximations made. Since the precession frequency of these excitations are determined by the exchange and anisotropy values, it represents an activation of the in-plane AFM THz mode–an unusual opportunity to activate a THz mode using optical excitation. Importantly, this represents an opportunity for all optical toggle switching where the driving mechanism is predicted to be induced fields, rather than thermal activation (see Sec. 3.3.4 for temperature simulations).

3.3.2 Preferential Switching

Eq. (3.6) shows that the quadratic reliance on the electric field polarisation of the generated torque in Eq. (3.8) allows a shift of the maximum torque away from the easy axis by rotation of the laser polarisation vector. Contrary to the toggle switching caused by $\varphi \parallel [\pm 100]$ or $[0 \pm 10]$ displayed in Fig. 3.4, shifting the azimuthal angle of the laser polarisation will create an asymmetric torque profile, influencing the Néel vector dynamical path from the four easy axes (see Fig.3.6).

Thus, the magnetisation will experience a larger torque when starting from only two of the four easy axis directions, giving a preference between clockwise and counter-clockwise switching (Fig. 3.6). This breaks the four-fold degenerate easy axis into "large" and "small" generated torques.

Fig. 3.7 shows the phase diagram of laser pulse intensity and duration which distinguishes between non-toggle (preferential) switching and toggle switching for starting orientations $[110]$ (Fig. 3.7a) and $[-110]$ (Fig. 3.7ab). The switching area labelled "toggle" switching in Fig. 3.7 is the region where both starting orientations switch either 90 or 180 degrees. Furthermore, Fig. 3.7a has preferential right-handed switching for the $[110]$ orientation at low fluence, with toggle switching for both orientations at higher fluence and middling pulse duration. A 45

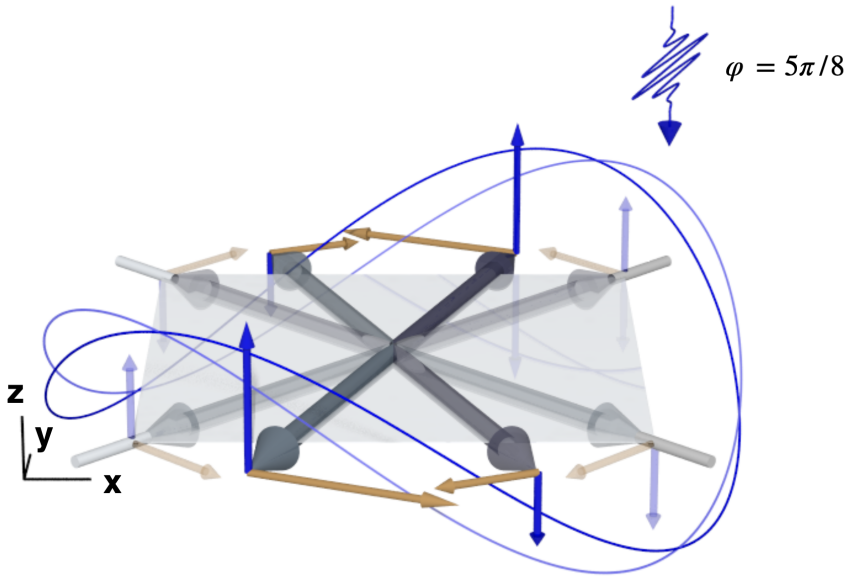

Fig. 3.6 Magnetisation trace of preferential switching under asymmetric torque. (Dark blue line): relative size and direction of the out-of-plane torque as a function of the magnetisation direction for electric field polarisation $\varphi \parallel 5\pi/8$. Opaque shows comparable torque and field sizes further along the path of motion from the easy axis. Note the unequal torque generated between clockwise and counter-clockwise motion. (Faded blue line): the same for $\varphi \parallel \pi/2$. Gold vectors denote relative field size and direction.

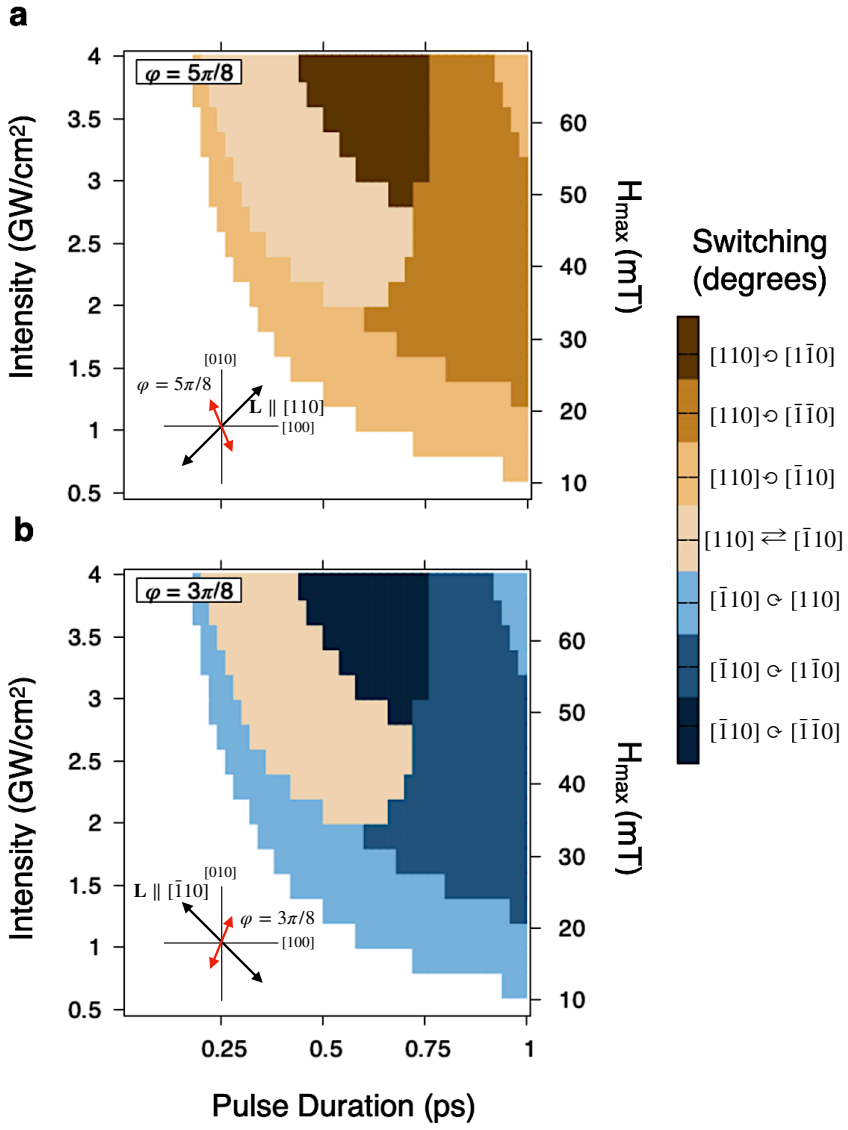

Fig. 3.7 Switching phase diagram for off-easy axis laser polarisations. (a)$\varphi = 5\pi/8$ and (b) $\varphi = 3\pi/8$ showing (a) preferential right-handed switching for starting magnetisation vector orientation $[110]$ vs (b) preferential left-handed switching for starting orientations $[-110]$. White spaces correspond to a lack of switching.

degree rotation of the laser polarisation changes the sign of the preferential torque, making left-handed switching from $[-110]$ easier at low fluence (Fig. 3.7b). Either laser orientation can be used to preferentially write the Néel vector to a desired orientation without changing the polarisation angle by using variable pulse duration/intensity (as shown in the next section).

3.3.3 Deterministic Switching

The preference for rotation direction and starting orientation can be used in combination with the toggle switching achieved by the same laser polarisation but with more intense pulses to deterministically control the Néel vector. Though the preferential switching provides only two control options: "small" and "large" torques, anisotropic magneto-resistance (AMR) measurements typically used to determine the magnetic state in antiferromagnets [13] depend only on the parallel component of the Néel vector "aligned" or "anti-aligned" with the resistance measurement vector in Hall devices. Thus, the $\pi/4$ and $-\pi/4$ ($3\pi/4$ and $-3\pi/4$) Néel states can be considered equivalent starting orientations for AMR measurements, so 90 or 180 degree switching from both starting orientations can be considered as toggle switching (the notation used in the previous section for Fig. 3.7). To demonstrate how preferential and toggle switching pulses from the same laser polarisation could be used to switch the Néel vector deterministically, we simulate a series of four laser pulses of varying intensity for each of the four starting orientations.

Fig. 3.8 details the Néel vector dynamics following sequential laser pulses with starting AFM order parameters along each of the MCA easy axes with laser polarisation parallel to the $5\pi/8$ azimuthal angle. The pulses are separated by 16 ps to allow the magnetisation to return to equilibrium. The second pulse is scaled to have more intensity than the others (Fig. 3.8a). Fig. 3.8b shows that the first, "small" pulse failed to switch the $3\pi/4$ and $-\pi/4$ orientations, but switching took place with the second, "large" pulse. Now that the magnetisation has been reoriented to the quadrant which experiences the maximal torque, it does successfully switch following a small pulse. This dependence is shown with the $\pi/4$ and $-3\pi/4$ orientations as well: since they start their magnetisation in the maximal torque quadrant, they show switching

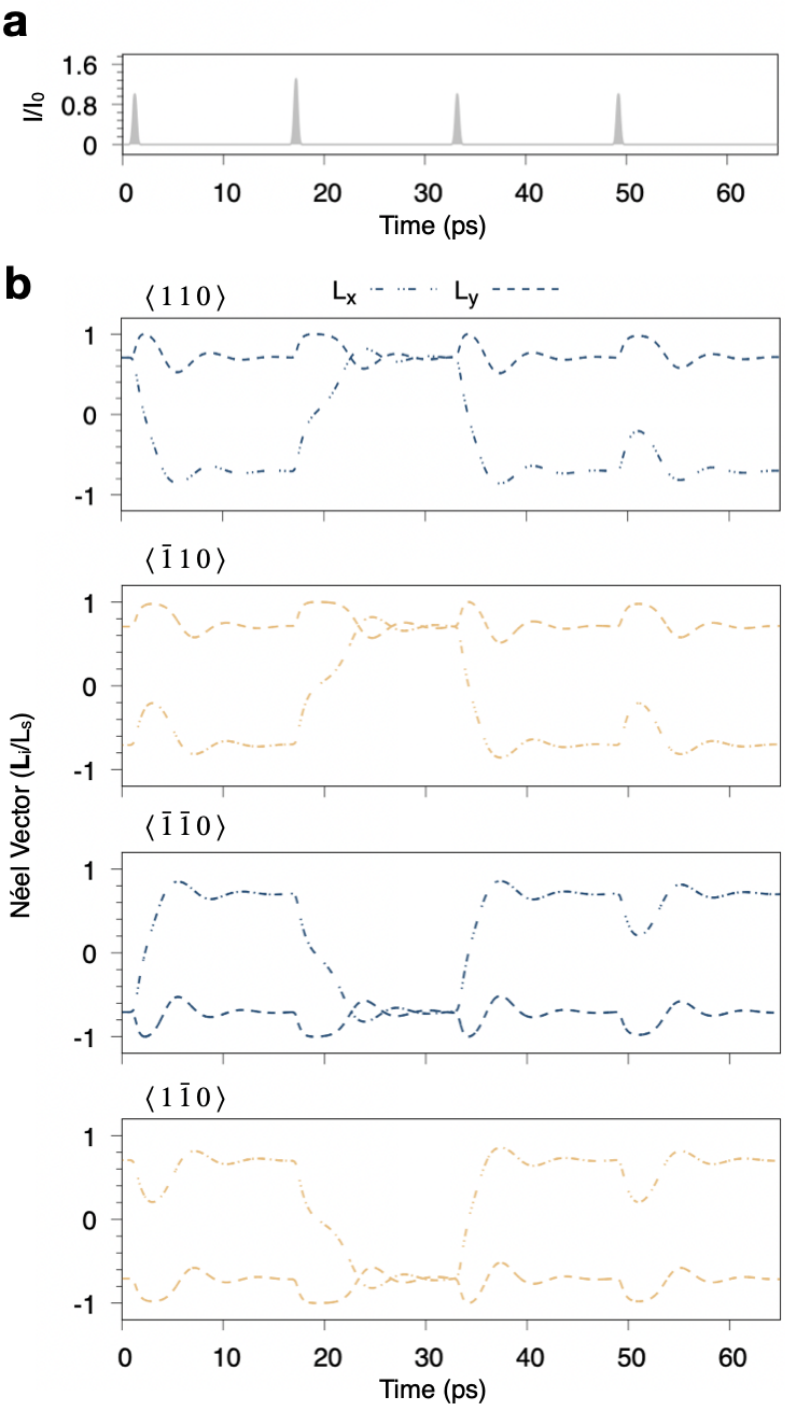

Fig. 3.8 Dynamics of the Néel order parameter showing deterministic switching. Four sequential pulses of 400 fs width and 16 ps apart. Each panel shows the Néel vector starting along each easy axis. The second pulse has an intensity of 2.6 GW/cm^2; all others are 2 GW/cm^2. Light polarisation is parallel to the angle $\varphi = 5\pi/8$.

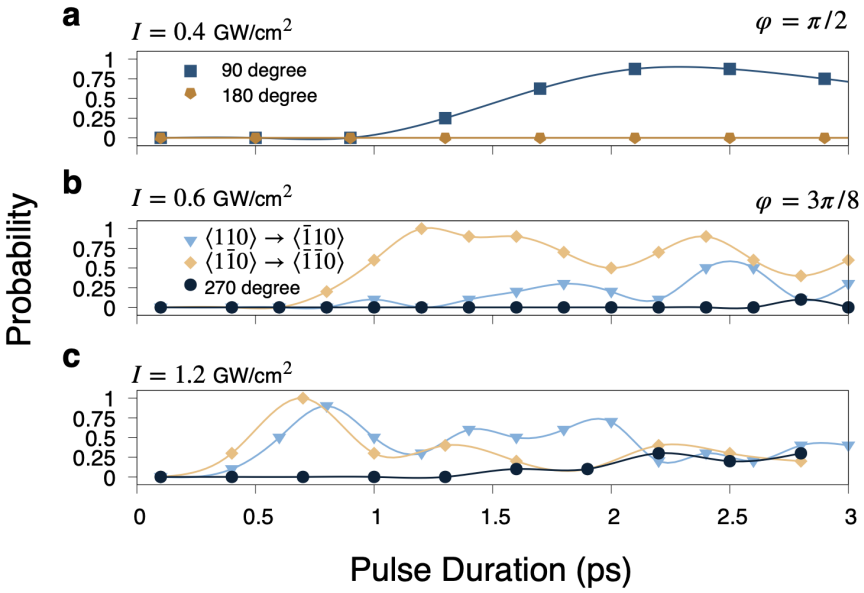

Fig. 3.9 Stochastic switching result for toggle, preferential, and deterministic laser polarisations. Switching probability for a grain $75 \times 75 \times 10$ nm^3. (a) with laser polarisation along $\varphi = \pi/2$. Laser intensity $I = 0.4$ GW/cm^2. Unpolarised (thermal-only) laser pulses (not shown) have very low switching probability. (b) Probability of switching depending on starting orientation. Laser polarisation along $\varphi = 3\pi/8$. Laser intensity $I = 0.3$ GW/cm^2. Blue and yellow data both represent 90 degree switching, but in different directions. (blue): left-handed switching. (yellow): right-handed switching. (c) Same laser polarisation as (b). Laser intensity increased to $I = 1.2$ GW/cm^2. Data legend the same as (b).

following the first, "small" pulse, as well as the second and third pulses, but not the fourth, since the magnetisation has moved to a minimum torque quadrant.

3.3.4 Temperature

A full analysis of temperature effects on LOT switching in multi-grain, multi-domain systems is beyond the scope of this article and would require a very large system size and large statistics. Here we consider a single domain, single crystal structure thin film, ($75 \times 75 \times 10$ nm^3) with periodic boundary conditions along $\hat{x}$ and $\hat{y}$, with thickness similar to the ones experimentally studied in [79, 78, 87]. As seen in other temperature switching models [56, 27, 82], the inclusion of temperature lowers the anisotropy barrier for switching and introduces the superparamagnetic effect, which is system-size dependent. To confirm the absence of the

superparamagnetic effect for our domain volume size, we ran ten LLG random seeds for 80 ps and observed no spontaneous switching. As is seen in Fig. 3.9a, in the absence of LOT and the presence of laser heating, this system does not present the superparamagnetic effect. Moreover, the transient heating from the laser pulse for intensities we consider is not enough to fully quench the magnetisation, and successive pulses do not raise the lattice temperature of the system substantially, which could potentially damage the sample. We calculate the switching probability for this grain. The results in Fig. 3.9a show the toggle switching with the probability approaching one in a range of pulse durations for a given intensity and $\varphi = \pi/2$ polarisation. Fig. 3.9b shows the preferential right-handed vs left-handed switching probabilities for a rotated $\varphi = \pi/3$ laser orientation on different Néel vector starting orientations. Thus, the addition of temperature to the simulations lowers the energy barrier for the system, but the laser heating for low fluence is not substantial enough to remove the anisotropy energy barrier and very high switching probability is obtained for our domain size consistent with the phase diagrams calculated at 0K.

3.4 Summary

By means of atomistic spin dynamics simulations with LOT we predict the possibility for metallic AFM all optical switching (AOS) on the sub- and low picosecond timescale. The unique symmetry relations of this torque prioritise 90-degree toggle switching for long pulse times, but also allow 180 or 270-degree switching provided sufficiently large pulse intensities are used.

Importantly, repeated laser pulses do not drive the order parameter continuously clockwise (counter-clockwise) like SOT/STT excitations, but instead provides toggle switching to the Néel vector.

We also predict that rotation of the laser polarisation to generate a quadrant-asymmetric torque introduces an additional level of control to the switching process, allowing for preferential, non-toggle switching. Temperature simulations which include the effects of laser heating on

the metallic sample show results consistent with the 0K diagrams. These results suggest the significant opportunity the LOT could provide for deterministic AOS in AFM spintronics.

The efficiency of the LOT may be preferred to other AOS methods. The minimum pulse intensity and fluence necessary to switch on the low sub-picosecond timescale using the LOT is estimated 1 GW/cm^2 and 0.65 mJ/cm^2, respectively. This is compared to the fluence for GdFeCo AOS in [75] of 4.4 mJ/cm^2 and the 6.51 mJ/cm^2 for Fe ultrafast demagnetisation generating spin current which is used for the STT switching in [63]. Additionally, the LOT has the advantage of not needing to be applied over short fs time scales to outpace the large laser heating effect from large intensities [82].

The category of the torque as an optical-frequency excitation also has direct implications for ease of experimental procedure: the generation of THz frequencies is a non-trivial procedure, and metallic AFM switching using THz excitation remains hampered by insufficient effective electric fields [20]. The LOT may thus offer a more accessible route to activating THz AFM modes for room-temperature spintronic devices, even with the large frequency discrepancy between the laser pulse and AFM mode. This application could be extended to Mn_2Au heterostructure systems with exchange bias or multi-domain systems used for neuromorphic computing [88] where THz activation through current or STT is less-preferable.

Applications of this torque method could be done in place of (or in conjunction with) spin-injected SOT/STT and intrinsic NSOT control methods to improve the efficiency of switching [72], domain wall driving [60], or THz generation [89, 90]. Moreover, this work seeks to expand the efficacy of second order laser coupling schemes for AFMs: while the results presented here are specifically for Mn_2Au, we extend the comment in Freimuth *et al.* that LOT is not unique to Mn_2Au [25]; second order terms with exotic and useful symmetries have been calculated to exist for altermagnets RuO_2 and CoF_2 [33] and even the 2D van Der Waals FM Fe_3GeTe_2 [91]. While the effects of second order optical coupling has been used to switch insulating AFMs at cryogenic temperatures [26, 92], their effects have not been studied for metallic AFMs. As the study and characterisation of asymmetric AFM responses to external stimuli continues, more materials of relevant symmetry should be included in the theoretical

and experimental study of optically generated spin torques beyond the first order coupling traditionally explored for metallic magnetic materials.

4

Domain Wall Driving Using Laser Optical Torque

4.1 Introduction

The study of domain walls (DWs) is of significant interest to spintronics for their potential applications in racetrack memory and computing, neuromophic computing, and reservoir computing [93, 88]. They can be naturally driven by unpolarised charge currents [94, 95], but are also sensitive to temperature [60, 96], temperature gradients [97, 19, 98], SOT and STT [99], and magneto-optical effects [100, 101]. Chapter 6 shows how a DW itself can be a useful tool for controlling spin injection in multilayer systems, but for neuromorphic computing they serve as a control feature for two disparate magnetic domains [88]. As with SOT-STT MRAM devices, the perpendicular resistance measurement will change as a ratio of the domains in the thin film [102]. AFMs are a natural choice for this category of device, as they avoid the high-power requirements to move FM DWs at fast-velocities without encountering Walker-breakdown of the magnetic texture [103, 104]. Numerous forms of DWs exist, especially for FMs, but for the case of AFM DWs we focus here on those with in-plane magnetisation. The most general definition of a DW is that it is the transition magnetic texture between two magnetic domains and will naturally take a form which minimises the energy of the texture. In our case we can describe the transition with an analytic solution based on the soliton solution of the Klein-Gordon equation (the so called sine-Gordon solution). The width of the DW is the determining factor for DW driving (in AFMs), and the width is governed by the gradient of

exchange interactions along the direction of the DW and the in-plane anisotropy stabilising the two domains [17]. This chapter serves to introduce the analytic background behind AFM DWs and their motion and demonstrate the ability of the LOT (introduced in Chapter 3) to efficiently drive and control these DWs, along with its possibility to nucleate additional magnetic textures beyond the original two domains in the system.

4.2 Methods

4.2.1 Analytic Domain Wall Description

The magnetisation landscape extant between two domains orientated at 90° to each other can be described by a solution to the Euler-Lagrange equation containing the exchange and anisotropy energy throughout the DW. To achieve this, we shall first rewrite the extended Heisenberg Hamiltonian for Mn_2Au in terms of orthogonal unit vectors $\mathbf{l} = \frac{1}{2}(\mathbf{S}_\mathrm{B} - \mathbf{S}_\mathrm{A})$ and $\mathbf{n} = \frac{1}{2}(\mathbf{S}_\mathrm{A} + \mathbf{S}_\mathrm{B})$, as done in similar fashion as [105, 106] and based on the pioneering work of [107, 108]. For this Hamiltonian we also make use of the tetragonal symmetry for the in-plane 4^{th} order anisotropy, rather than the rotational form in Eq. (2.25), in order to better match the analytic formalism of the previous works referenced above. This gives the Hamiltonian in this chapter as:

$$\mathcal{H}(\mathbf{n},\mathbf{l}) = \frac{1}{2}A\mathbf{n}^2 + \frac{1}{8}a(\partial_x \mathbf{l})^2 + |K_{2\perp}|(\mathbf{l}\cdot\hat{z})^2 - \frac{K_{4\perp}}{2}(\mathbf{l}\cdot\hat{z})^4 - \frac{K_{4||}}{2}\left[(\mathbf{l}\cdot\hat{x})^4 + (\mathbf{l}\cdot\hat{y})^4\right] + 2\gamma\hbar\mathbf{l}\cdot\mathbf{H}^{\mathrm{LOT}}, \tag{4.1}$$

where the first two terms encapsulate the exchange energy contributions in a continuum limit, given by the homogeneous exchange constant $A = 16|J_1^{atom}|$ and the inhomogeneous exchange constant $a = 8a_0^2(J_3^{atom} + |J_1^{atom}|/2)$, respectively. It is important to note the AFM J_2 interaction along the $\hat{z}$ axis of the tetragonal unit cell is disregarded in this analytical treatment, as it was shown previously to have a negligible influence on the in-plane 180° DW dynamics of a Mn_2Au thin film [106]. Also of note is the analytic distinction in the exchange constants of energy per atom, connected by a factor of $1/2$ to our constants defined as energy per link. We maintain

this assumption in the case of our in-plane 90° wall dynamics. The Zeeman-like energy term containing the H^{LOT} makes use of the relationship $\mu_0\mu_s = 2\gamma\hbar$.

Different to the description of 180° DWs in [17], our Hamiltonian includes the $K_{4||}$ anisotropy contribution in addition to the $K_{4\perp}$ and $K_{2\perp}$ terms, while it disregards the second-order, easy-axis contribution labelled $K_{2||}$ in [106]. For ease of calculation, in this analytical model we align the $K_{4||}$ easy-axes along $\hat{x}$ and $\hat{y}$, rather than the $\pm\pi/4$ axes of the crystal structure. This rotated symmetry does not affect the result of the formalism. Note another factor of $1/2$ in the definition between upper case anisotropy K defined as energy per unit cell volume, and the anisotropy defined in Table 2.1 with lower case k as energy per atom.

The LLG equation for a two sublattice magnetisation system ($\mathbf{S}_\mathrm{A}$, $\mathbf{S}_\mathrm{B}$) can in the limit $\alpha \ll 1$ be written in a Landau-Lifshitz (LL) form:

$$\dot{\mathbf{S}}_\mathrm{A} = -\gamma\mathbf{S}_\mathrm{A} \times \mathbf{H}^\mathrm{A}_\mathrm{eff} - \gamma\alpha\mathbf{S}_\mathrm{A} \times (\mathbf{S}_\mathrm{A} \times \mathbf{H}^\mathrm{A}_\mathrm{eff}), \tag{4.2}$$

$$\dot{\mathbf{S}}_\mathrm{B} = -\gamma\mathbf{S}_\mathrm{B} \times \mathbf{H}^\mathrm{B}_\mathrm{eff} - \gamma\alpha\mathbf{S}_\mathrm{B} \times (\mathbf{S}_\mathrm{B} \times \mathbf{H}^\mathrm{B}_\mathrm{eff}). \tag{4.3}$$

Coupling the two sublattices are the two effective magnetic fields $\mathbf{H}^{\mathbf{n},\mathbf{l}}_\mathrm{eff} = -\frac{1}{2\gamma\hbar}\frac{\delta\mathcal{H}(\mathbf{n},\mathbf{l})}{\delta(\mathbf{n},\mathbf{l})}$ defined with respect to the Hamiltonian in Eq. (4.1) and corresponding to the $\mathbf{n}$ and $\mathbf{l}$ vectors. $\mathbf{H}^{\mathrm{A,B}}_\mathrm{eff}$ in equations (4.2), (4.3) satisfy the following relationships:

$$\mathbf{H}^\mathrm{A}_\mathrm{eff} = \mathbf{H}^\mathbf{n}_\mathrm{eff} + \mathbf{H}^\mathbf{l}_\mathrm{eff}, \tag{4.4}$$

$$\mathbf{H}^\mathrm{B}_\mathrm{eff} = \mathbf{H}^\mathbf{n}_\mathrm{eff} - \mathbf{H}^\mathbf{l}_\mathrm{eff}. \tag{4.5}$$

Based on equations (4.2), (4.3), (4.4) and (4.5) it is possible to reduce the dynamics of our two sublattice magnetisation system in the exchange limit $|\mathbf{n}| \ll |\mathbf{l}|$ to the form below [109, 105, 106]:

$$\dot{\mathbf{l}} = \gamma \mathbf{H}^{\mathbf{n}}_{\text{eff}} \times \mathbf{l}, \tag{4.6}$$

$$\dot{\mathbf{n}} = (\gamma \mathbf{H}^{\mathbf{l}}_{\text{eff}} - \alpha \dot{\mathbf{l}}) \times \mathbf{l}. \tag{4.7}$$

Writing the explicit forms of the $\mathbf{H}^{\mathbf{n}}_{\text{eff}}$ terms in equation (4.6) removes the $\mathbf{n}$ vector dependence for the system. Hence, the system of equations (4.6), (4.7) can be rewritten solely in terms of the Néel order parameter $\mathbf{l}$ [109, 107, 108]:

$$\mathbf{l} \times \left[\partial_x^2 \mathbf{l} - \frac{1}{v_{\text{m}}^2} \ddot{\mathbf{l}} - \frac{4}{a} \frac{\partial \mathcal{H}_{\text{ani}}}{\partial \mathbf{l}} - \mathbf{h}_{\text{opt}} - \eta \dot{\mathbf{l}} \right] = 0, \tag{4.8}$$

where we collectively represent the distinct anisotropy contributions via the umbrella term $\mathcal{H}_{\text{ani}} = |K_{2\perp}|(\mathbf{l}\cdot\mathbf{z})^2 - \frac{K_{4\perp}}{2}(\mathbf{l}\cdot\mathbf{z})^4 - \frac{K_{4||}}{2}\left[(\mathbf{l}\cdot\mathbf{x})^4 + (\mathbf{l}\cdot\mathbf{y})^4\right]$. $\mathbf{h}^{\text{LOT}}$ is the reduced field $\mathbf{h}_{\text{opt}} = \frac{8\gamma\hbar}{a}\mathbf{H}_{\text{LOT}}$. a is the same inhomogenous exchange constant in Eq. (4.1). $v_m = \sqrt{aA}/(4\hbar) =$ 43.39 km/s is the so-called "magnon speed" governed by the exchange interactions. $\eta = 8\alpha\hbar/a$ is the dissipation constant containing the small damping constant α.

One last transformation is performed to describe the dynamics of the system in spherical coordinates. The relationship of the Cartesian coordinates to the coordinate of the system is:

$$\mathbf{l} \equiv \mathbf{u}_r = \cos\phi\hat{x} + \sin\phi\hat{y}, \tag{4.9}$$

$$\mathbf{u}_\phi = -\sin\phi\hat{x} + \cos\phi\hat{y}, \tag{4.10}$$

$$\mathbf{u}_\theta = -\hat{z}. \tag{4.11}$$

Finally, in this new coordinate system Eq. (4.8) reduces to the familiar SG-like equation below:

$$\partial_x^2\phi - \frac{1}{v_{\text{m}}^2}\ddot{\phi} - \frac{1}{4\Delta_0^2}\sin 4\phi = 0. \tag{4.12}$$

where $\Delta_0 = \sqrt{a/(8K_{4||})} = 50.8$ nm is now the DW width factor. Eq. (4.12) gives the time-varying and spatially varying solution for the Néel vector angle ϕ. At the moment, the

contribution from the driving field H^{LOT} and thus the dissipation factor η are not included in order to relate the DW width factor Δ_0 to the spatially-varying magnetisation solution by reducing the expression to a second-order differential equation in space. The configuration energy of the DW at rest is now expressed as:

$$E = \frac{a}{8}\left(\partial_x \phi\right)^2 - K_{4\parallel} \sin 4\phi, \tag{4.13}$$

We can now reintroduce the $\pm\pi/4$ easy axes of the system with no loss of generality and apply the boundary conditions of the two domains $\partial_x \phi\left(x \to \pm\infty\right) = 0$ and $\phi\left(\pm\infty\right) = \left(\pm\pi/4\right)$ to reduce the second-order differential equation above to first-order in space:

$$\sqrt{\frac{p}{K_{4\parallel}}}\left(\partial_x \phi\right) = 8\,Q \sin 2\phi, \tag{4.14}$$

where $Q = \pm 1$ represents the DW chirality. Integrating the previous expression, taking into account that the DW centre position x_0 can be defined as $\phi\left(x = x_0\right) = 0$, it can be found that:

$$\int_{\pi/4}^{\phi(x)} \frac{\partial \phi}{\sin 2\phi} = 8\,Q \sqrt{\frac{K_{4\parallel}}{a}} \int_{x_0}^{x} \partial x \tag{4.15}$$

which allows us to obtain the spatial dependence of the in-plane azimuthal angle, ϕ:

$$\phi\left(x\right) = \arctan\left(\exp\left\{\frac{Q\left(x - x_0\right)}{\Delta_0}\right\}\right) - \frac{\pi}{4}. \tag{4.16}$$

For our simulations we analyse a DW with Q value $+1$. The sin of the azimuth can now give the magnetisation component m_y of the DW:

$$m_y = m_e \sin\phi = m_e \sin\left(\arctan\left(\exp\left\{\frac{x - x_0}{\Delta_0}\right\}\right) - \pi/4\right) \tag{4.17}$$

4.2.2 Laser Optical Torque

To obtain the time-dynamic solution for Eq. (4.12), we reintroduce the LOT field H^{LOT} and dissipation term η. For ease of calculation in the analytical model above, we performed a 45° in-plane rotation such that the easy-axes point along the $\hat{x}$ and $\hat{y}$ Cartesian directions instead.

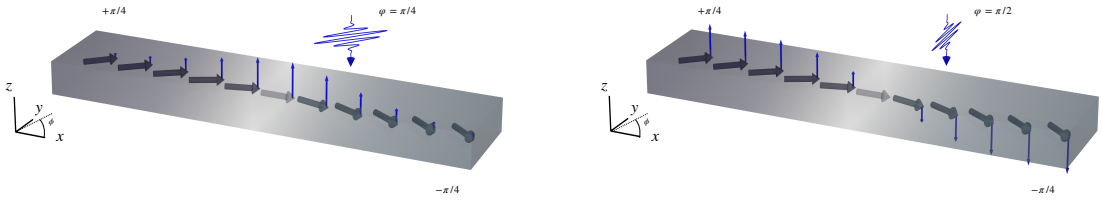

(a) $\varphi = \pi/4$ **(b)** $\varphi = \pi/2$

Fig. 4.1 Diagram of the LOT symmetry across a 90° DW.

For this reason, the angular variation of the LOT acting on the Néel vector $\mathbf{l}$ from Eq. (3.8) in Chapter 3 also needs to be adjusted here to:

$$\mathbf{H}_{\mathrm{LOT}} = \frac{1}{\mu_s}\mathcal{T}(I)\cos(2\varphi - 2\phi)\hat{z}\times\mathbf{l} \tag{4.18}$$

The symmetry of the induced fields from Eq. (4.18) follows the same relationship as in Fig. 3.1. To drive a 90° DW, care must be taken in choosing the laser polarisation angle φ. Because of the change in torque sign, the only polarisation angle which gives uniform torque across the domains and DW is $\varphi = \pm\pi/4$, which results in maximal torque at the centre of the DW where $\phi = 0$ (Fig. 4.1a). Alternative polarisations along $\varphi = \pi/2$ or $\varphi = 0$ result in mismatched torque on the domains (Fig. 4.1b). This can have the result of widening or contracting the DW without a change in position x_0. These results are considered later, but not in the context of the sine-Gordon solution. For now, the polarisation angle is fixed to $\varphi = \pi/4$.

A unique consequence of the LOT torque symmetry is its apparent inability to drive 180° DWs. This can be understood as a consequence of the same polarisation requirements to drive 90° walls, except there is no polarisation angle which produces uniform torque on the system. This is visualised in Figs. 4.2b and 4.2a. Again, the LOT could be used to widen or contract these 180° DWs, but their appearance in Mn_2Au is not supported by experiment [13, 110].

The laser polarisation can be oriented along $\pm\pi/4$ to produce equal but opposite torques to drive the DW forward or reverse, depending on the handedness of the DW configuration rotation (Q factor in Eq. (4.16)). Because of the four-fold anisotropy symmetry, there are thus eight combinations of DW configuration and laser polarisation. Fig. 4.3 shows three

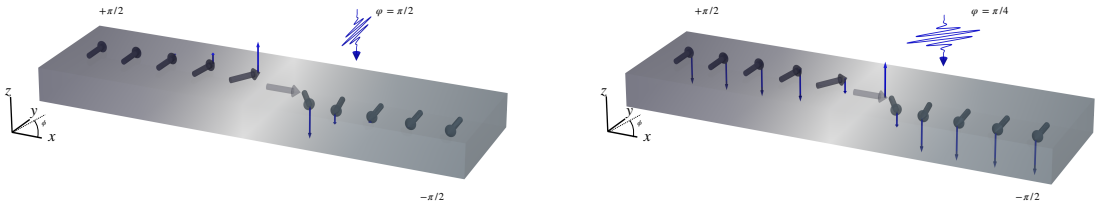

(a) $\varphi = pi/2$ **(b)** $\varphi = pi/4$

Fig. 4.2 Diagram of the LOT symmetry across a 180° DW.

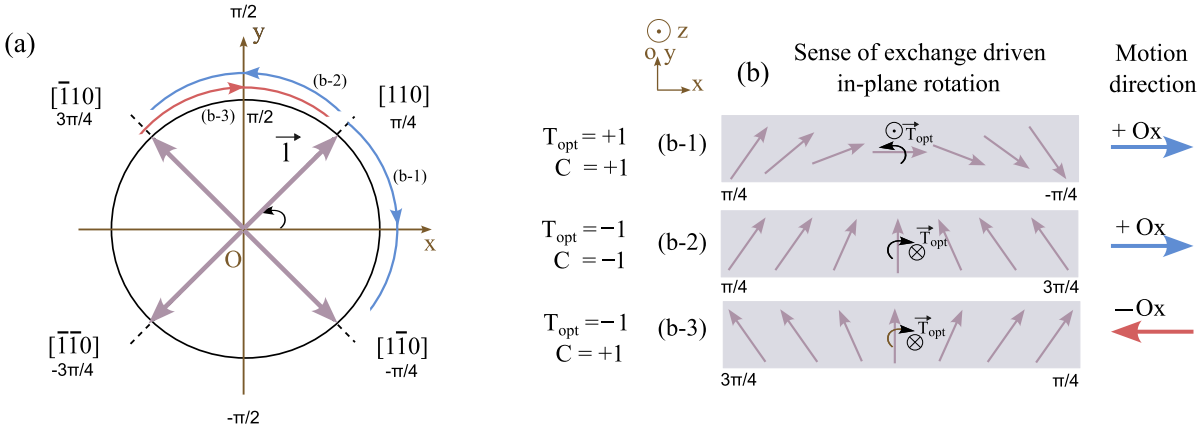

Fig. 4.3 DW and torque configurations. (a) Mapping the in-plane Néel vector orientation in the magnetic track along the unit circle. We display the four possible 90° DW boundaries corresponding to the $K_{4||}$ easy directions. Taking as reference the Néel vector parallel to the [110] diagonal, we can obtain two DW geometries with right and left handedness, labeled (b-1) and (b-2) respectively. The corresponding spin configurations are displayed in subplot (b). Distinctly, the (b-3) wall geometry is driven towards $-\hat{x}$. Figure courtesy of P. Gavriloaea in [23].

example calculations of the torque and configuration symmetry to describe the forward or reverse motion.

Mapping the spin configuration along the unit circle, one can trace the eight possible 90° DW geometries in our bi-axial AFM. The direction of motion depends on the sign of the torque relative to the handedness of the wall. We assign $C = +1$ for right-hand side DW handedness (clock-wise spin rotation) and $C = -1$ for left-hand side DW handedness (counter clock-wise spin rotation). Since the torque maintains its sign across the DW configuration, we can distinguish two situations, positive and negative torque $T^{\mathrm{LOT}} = \pm 1$. If the product $T^{\mathrm{LOT}}C$ is positive, the DW will displace towards $+\hat{x}$, otherwise the motion will take place

in the opposite direction. In Fig. 4.3b we exemplify this behaviour for three distinct DW configurations. Taking as a reference the Néel vector parallel to the $\langle 110 \rangle$ direction in subplot (a), we construct two 90° DW configurations following a right or left-hand side rotation along the unit circle. The corresponding spin arrangements labeled (b-1) and (b-2) can be observed in subplot (b) of Fig. 4.3. Both T^{LOT} and C change their sign in between the two geometries, hence the product $T^{\mathrm{LOT}}C$ remains positive and the DW displacement direction is preserved. Depending on the sign of T^{LOT}, the resulting in-plane rotation of the Néel vector will take place in opposite directions. $T^{\mathrm{LOT}} = +1$ gives rise to counter clock-wise rotation, while $T^{\mathrm{LOT}} = -1$ promotes clock-wise rotation. To maintain the DW direction of motion, the handedness of this in-plane rotation must oppose the handedness of the wall. Therefore the T^{LOT} change of sign in between configurations (b-1) and (b-2) matches this requirement and thus preserves the direction of motion towards $+\hat{x}$.

The situation changes if we compare the (b-2) and (b-3) 90° DW profiles. Here the $T^{\mathrm{LOT}}C$ product changes sign which promotes displacement in opposite directions as confirmed by our ASD simulations. Taking as reference any other 90° DW configuration along the unit circle in Fig. 4.3a, we observe the same behaviour.

4.2.3 Domain Wall Driving

For the sine-Gordon solution then, steady-state motion is achieved when the Zeeman energy from the induced field is balanced by the dissipation term η. The reduced field h^{LOT} is then described as:

$$\mathbf{h}^{\mathrm{LOT}} = \frac{8\gamma\hbar}{a}\mathbf{H}^{\mathrm{LOT}} = \frac{8\gamma\hbar}{a}\mathbf{T}_{\mathbf{l}}^{\mathrm{LOT}} \times \mathbf{l} = -\frac{8\gamma\hbar A \sin(2\phi)}{a}\mathbf{u}_{\theta} \times \mathbf{u}_{r} = -h^{\mathrm{LOT}}\mathbf{u}_{\phi}. \tag{4.19}$$

This gives the full macrospin solution for the DW:

$$\partial_x^2\phi - \frac{1}{v_{\mathrm{m}}^2}\ddot{\phi} - \frac{1}{4\Delta_0^2}\sin 4\phi - h^{\mathrm{LOT}}\sin(2\phi) - \eta\dot{\phi} = 0. \tag{4.20}$$

The velocity of the DW under steady-state motion is $v_0 = 4\Delta_0 h^{\mathrm{LOT}}/\eta$, with the exchange components a ultimately cancelling to give the velocity dependent only on the width factor, field, and damping constant. The factor of four comes from the 90° DW. In real simulation variables, the steady-state velocity in the linear regime from a driving H^{LOT} is:

$$v_0 = 4\gamma\Delta_0 H^{LOT}/\alpha \tag{4.21}$$

Beyond the linear regime approaching the saturation velocity, the relationship is more complex. A well known behaviour of AFM solitons, mainly discussed previously for 180° DWs [99, 16, 17], is the Lorentz invariance of Eq. (4.20). Since the magnon limit v_m functions as the "speed of light" for the medium, a soliton velocity at an appreciable percentage of this limit must undergo the appropriate Lorentz transformations:

$$\Delta(v) = \Delta_0\sqrt{1-\frac{v^2}{v_m^2}} \tag{4.22}$$

which is the traditional length contraction. Since the width of the DW affects the steady-state velocity, the contracted width must be used to calculate the resultant velocity. This can be rearranged to solve for the velocity in terms of the width factor at rest Δ_0 and the effective field H^{LOT}:

$$v = \frac{v_m}{\sqrt{1+\frac{v_m^2}{v_0^2}}} \tag{4.23}$$

For 90° DWs under traditional SOT driving, the Lorentz contraction in Eq. (4.22) is much more difficult to derive due to non-zero torque on the boundaries changing the boundary conditions used to derive Eq. (4.16). Methods to address this are discussed in Chapter 6, but is not applicable here under LOT driving.

The driving mechanism comes from the staggered fields induced on the Mn sublattices generating a non-staggered torque on the Néel vector. This engages the exchange enhancement from the AFM exchange to rotate the spins, driving the DW.

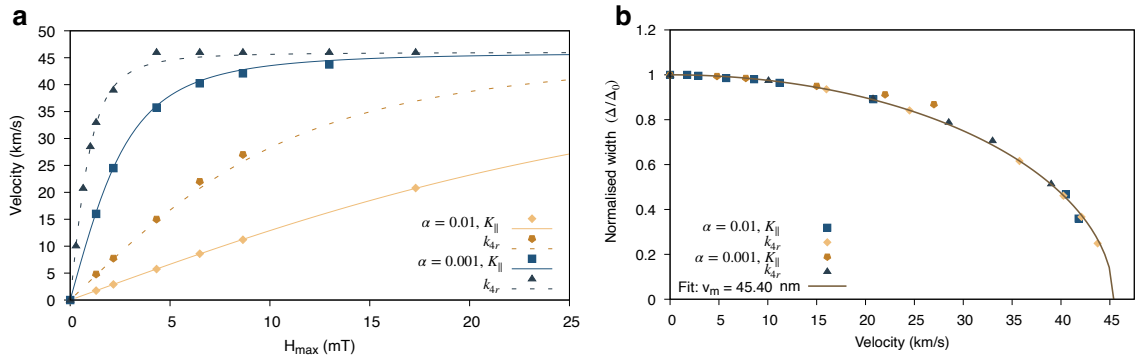

Fig. 4.4 Numerical results and SG predictions of steady-state 90° DW dynamics. (a) Steady-state velocity for simulation LOT field for damping parameters $\alpha = 10^{-2}$ and $\alpha = 10^{-3}$ and tetragonal and rotational forms of the anisotropy. Points represent the data and lines the analytic calculation from Eq. (4.23). (b) Contraction of the DW width as a function of the propagation velocity.

4.3 Results

For our atomistic simulations we use thin wire one unit cell tall ($z = 0.86$ nm) and two unit cells wide ($y = 0.66$ nm) with periodic boundary conditions along y only. The laser pulse follows a square profile with 30 ps maximum intensity and a half Gaussian profile of 8 ps to give the DW smooth excitation to reach the steady-state velocity in order to compare with the analytic expressions (Fig. 4.5c, Fig. 4.7c). The track length was 5000 nm to prevent the DW being driven out of the system. ASD simulations with a larger cross-section were performed at 0 K to confirm agreement with our unit cell track.

Fig. 4.4 shows our results for maximum steady-state velocity and minimum width factor for increasing laser intensities (converted to field for Fig. 4.4a) for better comparison with [99, 17]). In this result we also perform simulations with the rotational in-plane anisotropy described in Eq. (2.25), rather than the tetragonal form used in the sine-Gordon derivation for the DW motion. The results show no serious deviation from the analytic model once the change in rest width is used for Eqs. (4.22) and (4.23) (17.39 nm vs 50.9 nm), showing clear Lorentz invariance of the rotational anisotropy (an analytic discussion of the impact of rotational and tetragonal forms of anisotropy on the DW is in Chapter 5). The saturation velocity is slightly larger than the calculated magnon speed of 43.39 km/s. For the tetragonal form, the fit to Eq.

(4.22) for the data in Fig. 4.4b gives $v_m = 45.4$ km/s. The rotational form has a slightly higher $v_m = 45.79$ km/s (better seen in the saturated velocity of Fig. 4.4). This slight deviation in v_m could be from asymmetries in the DW profile which are a departure from the sine-Gordon soliton solution.

Another application of the LOT to DWs could be its use in proliferating new, additional textures beyond the starting two domains. Fig. 4.5 shows this occur for a DW accelerated with a field beyond the magnon limit. Emanated spin waves moving at v_m trail behind the supermagnonic DW (see Fig. 4.5a) in an effort for the DW to lose effective mass (see [16, 111]). The DW is no longer following the soliton solution for Eq. (4.20), as both the leading and trailing edge of the DW no longer follow Eq. (4.16). This enhances the LOT driving, forming a resonance effect to further increase the velocity of the magnetic texture. Nucleation occurs when the energy of the texture overcomes the energy barrier necessary to nucleate an additional DW pair [16]. The topological nature of this new texture depends on the LOT symmetry and DW configuration, as in Fig. 4.3. Fig. 4.5e shows this new DW pair configuration. The original wall and the new 90° wall function as an effective 180° wall, and are thus locked in place by the LOT (see Fig. 4.2a). Larger laser intensities affect the equilibrium distance between the pair of DWs, and the system will relax into a stable pair provided they do not overlap other textures. This result confirms the possibility from Figs. 4.2b and 4.2a for the LOT to manipulate, but not drive, 180 ° textures.

The second 90° wall continues to propagate in the same direcction as the original, steadily building up new effective mass (see Fig. 4.5b). Continued driving of the DW, or driving with higher laser intensities, sees further nucleation of magnetic texture. The stability of these textures after laser excitation is determined by their distance and topological character [16]. The pair of spin textures are stable in a reasonable time frame achieved by atomistic simulations after the laser pulse is stopped, provided they do not overlap.

Since the Zeeman energy contribution always remains zero in our case, as the geometry in Eq. (4.18) maintains $\mathbf{H}_i^{\text{opt}}$ always perpendicular to the local spin direction $\mathbf{S}_i$, the question is, therefore, from where does the energy required for the nucleation of additional magnetisation textures arise? In subplot (a) of Figure 4.5, we represent the azimuthal angle ϕ along the

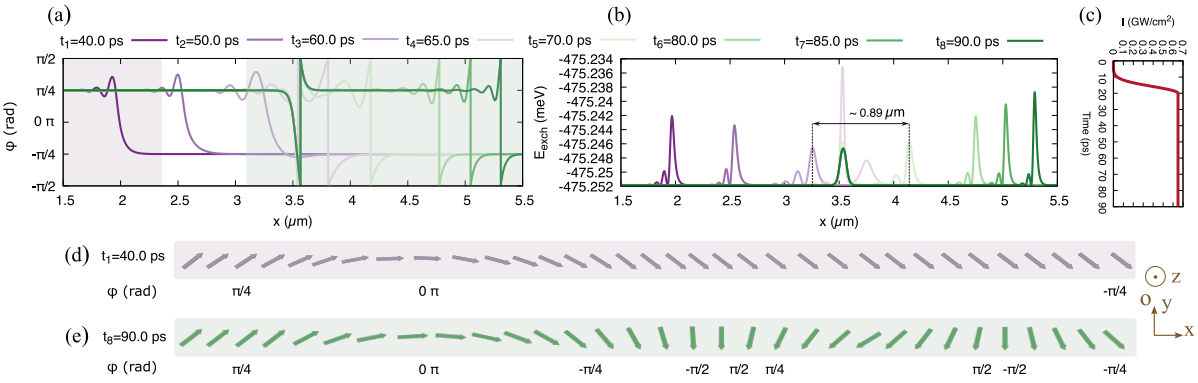

Fig. 4.5 Proliferation event in the supermagnonic regime. (a) $\phi(x,t)$ variation along the track during the 90° DW displacement and nucleation. (b) Energy variation during the nucleation. Subplots (a) and (b) share the time legend. (c) Laser intensity protocol with peak laser intensity of $I = 0.65$ GW/cm^2. (d-e) Schematics of the Néel vector configuration corresponding to the purple and green shaded regions in (a), at $t_1 = 40$ ps and $t_8 = 90$ ps respectively. Figure courtesy of P. Gavriloaea in [23].

track during a 90° wall displacement excited via a half-Gaussian, laser pulse of peak intensity $I = 0.65$ GW/cm^2 (see laser profile in subplot c). Time-steps t_1, t_2, t_3 show the characteristic low-frequency SW, lagging behind and broadening the width of the 90° DW as it is pushed beyond the magnonic barrier. A gradual, corresponding decrease in the exchange energy is evidenced by subplot (b). Due to the competition between the anisotropy and exchange energies, this broadening cannot indefinitely take place, forcing a rebound process characterised by a contraction of the wall. A drastic reduction of the DW width can be observed between t_3 and t_4 along with a large increase in the exchange energy. This continuous deformation leads to the appearance of oscillatory patterns at the front of the propagating wall, which on a ps time-scale invest part of the relativistic energy carried by the DW towards the nucleation of an additional magnetisation texture, as evidenced at t_4 and t_5. Visible at t_6, t_7 and t_8, the initial spin structure morphs into a static magnetisation texture pinned around the $x = 3.5$ μm mark, while its surplus, relativistic energy is invested towards pushing ahead a novel spin structure.

The physical origin of the effect relies on the rapid transfer of relativistic energy from a propagating DW near the magnonic barrier into new stable magnetisation textures. Comparing snapshots t_3 and t_5, we estimate the energy transfer across the track from the parent to the child magnetic texture takes place with an average velocity of 89 km/s (0.89 μm travelled in 10 ps),

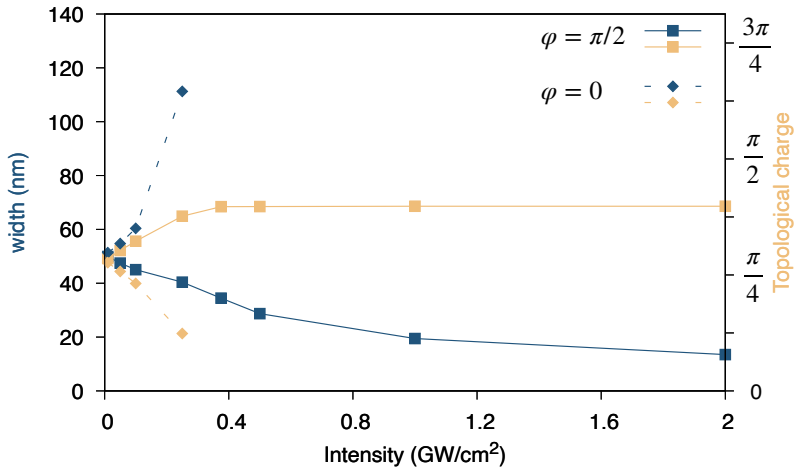

Fig. 4.6 DW expansion and contraction under rotated laser polarisation. The steady-state topological charge of the DW under

largely exceeding the magnonic limit for a pure soliton or spin wave. Further work is needed to characterise the critical intensity needed to nucleate these new textures in a deterministic manner, as the addition of temperature to the DW is likely to make nucleation a stochastic process (see Chapter 5). Likewise are the effects of temperature and laser heating on the DW driving investigated in the next chapter.

We have also investigated the use of the LOT to manipulate static DWs, rather than drive them. Fig. 4.1b shows a laser polarisation which does not produce torque to drive the DW. Instead, a laser polarised along $\pm\pi/2$ will either expand or contract the DW, depending on the configuration handedness. Fig. 4.6 shows this effect as a function of the laser intensity. Unlike the laser polarisation angles used to drive the DW in Fig. 4.2, the angles used to expand/contract the DW do exert a non-zero torque on the domain boundaries of the system–leading to the non-conserved topological charge seen in Fig. 4.6. This makes describing the system using the SG solution difficult. Qualitatively, it can be observed that the width expansion/contraction (also reported in Fig. 4.6 as the topological charge) shows an asymptotic approach to the limits of the DW geometry. For the expansion, this limit is given by the critical switching field (see Chapter 3. For contraction, the theoretical limit is given by the exchange of the system, and is

far beyond a reasonable laser intensity. The DW width under contraction reaches an appreciable minimum value at a larger intensity than the expansion polarisation overcomes the in-plane anisotropy of the system. This has interesting effects for systems with multiple domains–each experiencing expansion or contraction–which will be studied in more detail at a later date, as it has implications for AFM spin pumps and DW springs using optical control [112–114].

Fig. 4.7 displays the DW width vs. time for this phenomenon for three increasing laser intensities. The oscillation frequencies of the DW widths are independent of the laser intensities. The phase of the frequency, however, changes between the laser polarisations expanding/contracting the DW. The opportunity for the LOT to excite DWs without driving them presents new opportunities for AFM characterisation. Recent experiments with Mn_2Au|NiFe bilayers have shown the ability to differentiate the relative Néel orientation distribution in a multidomain sample between all four in-plane easy axes using THz excitation [113]. With the additional level of symmetry in the LOT compared to the SOT driven by THz excitation, the use of optical frequency characterisation of AFMs is of significant interest to AFM spintronics.

4.4 Summary

In conclusion, our simulations and analytic model reveal the possibility to drive a 90° AFM DW under the novel LOT introduced in Chapter 3. Interestingly, this excitation protocol does not allow the motion of 180° DWs, but can affect the width. In the same way, 90° DW walls can be manipulated without driving depending on the laser polarisation and DW configuration. Since the contracted DW is at an elevated soliton energy, the relaxation will mimic a relaxing magnetic spring, emanating spin waves as it decays to the ground state. This could be used for sensing or memory applications, or to generate THz emissions. Chapter 6 explores the effect DWs have on spin currents, so an oscillating DW in combination with an injected or intrinsic spin current could be a source of THz charge currents.

An important result of our simulations is the driving efficiency of the LOT for 90° DWs. Typical experiments of laser-induced DW dynamics in FMs make use of fluences in the range of a few mJ/cm^2 which amount to intensities normally in the 1 and 10 GW/cm^2 interval for

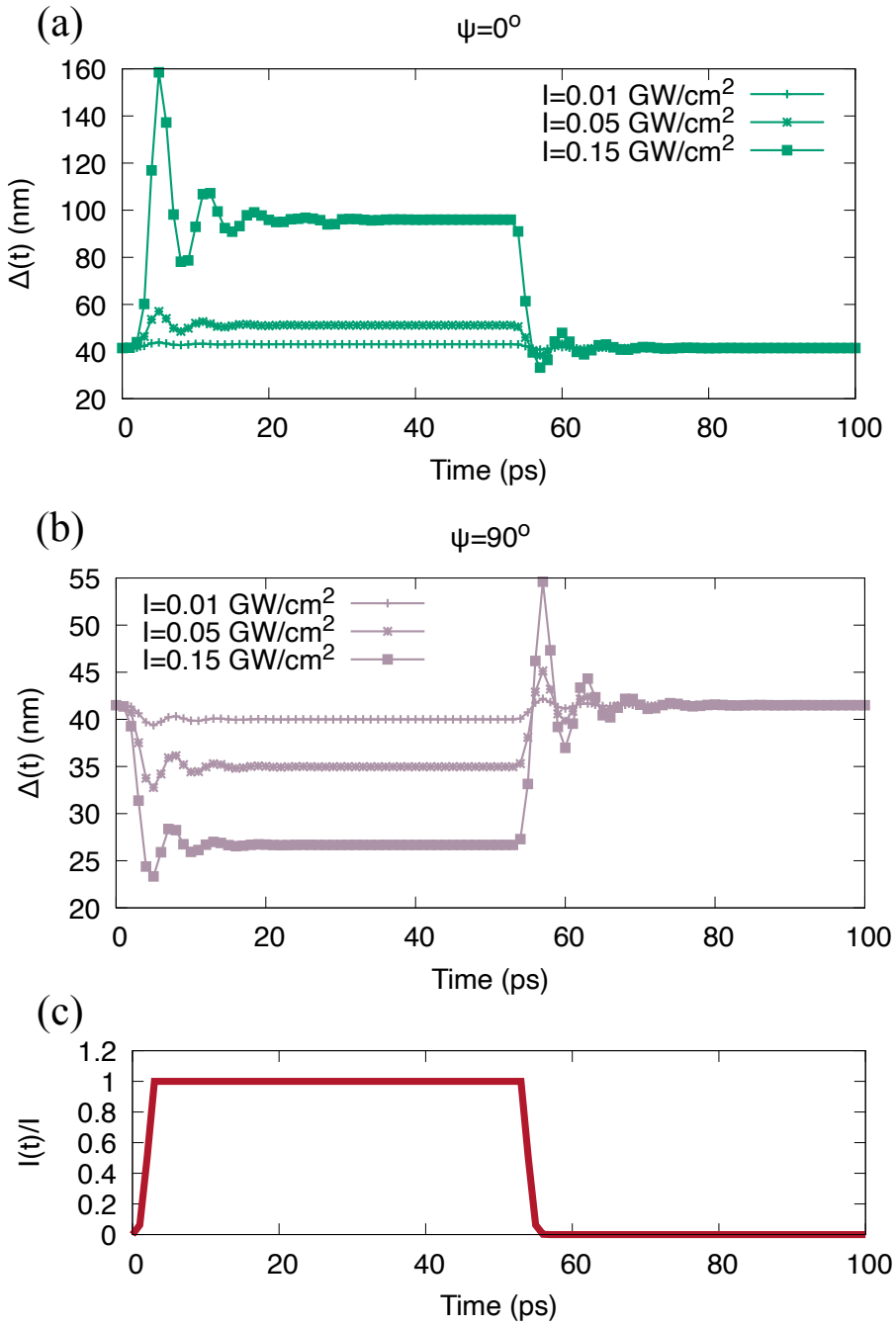

Fig. 4.7 DW expansion and contraction dynmics under varying laser intensities. Figure courtesy of P. Gavriloaea in [23].

DW motion on the order of m/s [115, 116]. In comparison, we predict kinematics up to the supermagnonic limit ($v = 46$ km/s) by single pulse excitation below 0.3 GW/cm^2, though effort will need to be made to control the thermal heating generated by the laser pulse (see Chapter 5). Manipulating highly non-linear dynamics in magnetic systems may play an important role in the development of future reservoir computing archetypes [117–119]. We envision thus a combined, opto-electronic experimental scheme towards the realisation of a multiple-node reservoir. Driven by an optical input, fast and periodic nucleation events could be manipulated in an AFM DW fabric [120]. The anisotropic magnetoresistive effect [121] allows an output electrical signal to be correlated to changes in the magnetic texture, thus posing an interest for pattern recognition and prediction applications. The use of LOT in AFM materials could be an opportunity for ultra-low energy driving and reading of AFM textures at room temperature.

5

Temperature-dependent magnetic properties of the antiferromagnet Mn_2Au

5.1 Introduction

Antiferromagnetic (AFM) materials are a key feature in nearly all magnetic recording devices. More recently, it has been discovered that using the AFM as the active element, instead of a ferromagnet, could massively outperform conventional devices in terms of mechanism speed and energy consumption/dissipation [122, 123, 66, 124–127]. AFMs are especially interesting due to their intrinsically ultrafast dynamics and higher data density. One of the most promising materials for these devices is Mn_2Au due to its high Néel temperature [10], low in-plane anisotropy [128], and high conductivity [20]. In electrically driven switching of AFMs the necessary current densities are very high, and the resultant Joule heating thermal effects become especially important [129–132, 13]. Thus, it is essential to understand the role of thermal spin fluctuations and temperature dependent magnetic properties of AFM materials. A correct account of the thermal effects is especially important when modelling spin-orbit-torque magnetisation dynamics and switching in nanoscale systems, which can be done with atomistic [133, 134, 60, 135, 136] or micromagnetic [137–140] simulations. For the latter, effective models (where thermodynamic averages of the sublattice spin order are used), the knowledge of the temperature scaling of the magnetic anisotropy–the micromagnetic

exchange stiffness–and the domain wall width become crucial for a realistic modelling of electrically-induced spin-orbit-torque magnetic switching.

In this Chapter, we present atomistic spin dynamics (ASD) simulations of the intricate temperature dependent magnetic properties of Mn_2Au, guided by previous *ab initio* calculations [141, 142]. Taking into account the description of two-ion anisotropy in Shick *et al.* [142], we introduce a modified uniaxial term to the exchange tensor for 2^{nd} order anisotropy. Likewise, we calculate the different temperature scaling of the azimuthal and rotational anisotropies governing the domain wall dynamics of the system. Through calculation of the temperature dependent domain wall width we reconfirm the temperature dependence of the micromagnetic exchange energy simulated from constrained Monte Carlo modelling. This provides an exact analytical expression for the domain wall profile with rising temperature for low temperature up to the thermal breakdown of the 4^{th} order anisotropy at $\approx$ 800K. Our findings strengthen our understanding of Mn_2Au and open the door to an accurate theoretical exploration that can pave the way to all-AFM spintronic applications.

5.2 Methods

5.2.1 Hamiltonian

In developing spin Hamiltonians it is important to consider the thermodynamic context in which they are used. In particular, it is important to take note of the origin of the anisotropy itself. For example, in the case of uniaxial anisotropy of order l and azimuthal angle θ, if the anisotropy has a single site origin, the usual form $E(\theta) \propto \sin^l \theta$ will be applicable for all temperatures. However, if the anisotropy has a 2-site origin as in Mn_2Au (usually from an exchange anisotropy) the above form will be applicable only at 0 K, where the spins are fully aligned. In this case the temperature-dependence of the anisotropic contribution to the Hamiltonian will not be physically reproduced by a single-ion term. The departure comes from the treatment of temperature-dependent anisotropy and exchange in the atomistic Hamiltonian. The formalism for anisotropy allows for two implementations:

- As an anisotropic exchange term describing its fundamental origin, or
- with isotropic exchange and single-ion anisotropic contribution

As discussed in Chapter 2, the origin of the anisotropy is distinct between the two implementations, but are equivalent at 0 K. The intrinsic link between exchange, lattice, and temperature, however, makes the effect of temperature on anisotropic exchange difficult to untangle for both DFT and experimental fields. For atomistic Hamiltonians and single-ion anisotropy, there is little difference between the two implementations above, as the exchange and anisotropy are not temperature-dependent constants. But for macroscopic Hamiltonians, careful parametrisation is necessary in order to produce constants which accurately reflect the effect of temperature on exchange and anisotropy for both inter- and intra-cell constants. For bimetallic systems with large two-ion anisotropic contributions to exchange (e.g., Mn_2Au, IrMn [41], and FePt [143]), the origin of the anisotropy must be respected even for the atomistic Hamiltonian. Thus, this sections presents construction of our atomistic spin Hamiltonian guided by the physical origin of the anisotropic contributions for each order of crystal symmetry in the phenomenological Hamiltonian [41]:

$$E(\theta,\phi) = K_{2\perp}\sin^2\theta + K_{4\perp}\sin^4\theta + K_{4\parallel}\sin^4\theta\cos 4\phi, \tag{5.1}$$

The tetragonal lattice symmetry phenomenologically follows the symmetry orders presented in the equation above (Eq. (5.1)), giving three non-zero anisotropy symmetry contributions. To distinguish our atomistic Hamiltonian constants from the macroscale constants in Eq. (5.1), we will use lower case k for atomistic constant and upper case K for macroscale. A note is first made about the unit conversion from *ab initio* calculations to this work: the foundational anisotropic contributions calculated by Shick *et al.* in [41] utilise a tetragonal lattice symmetry with two fundamental unit (f.u.) cells per crystal lattice. Since the anisotropy constants are reported as energy density, we convert from energy per volume to energy per atom by noting four magnetic atoms present in the tetragonal lattice, giving two atoms per f.u.. This factor of two has already been taken into account for the constants in Table 2.1.

Experimentally, it has been observed that the Akulov-Zener-Callen-Callen [144–146] relation (ZACC):

$$k(m_e) = m_e^{l(l+1)/2} \tag{5.2}$$

where l is the power order of the anisotropy (e.g. 2^{nd}, 4^{th}, etc.) often describes the macroscopic parametrisation of the anisotropy with reduced magnetisation $m_e = \langle m \rangle / m_s$ from increased temperature. In order to allow our atomistic spin Hamiltonian to produce anisotropy and exchange constants which follow the ZACC relation, we describe the phenomenological Hamiltonian in Eq. (5.1) using orthogonal functions which maintain the power order l of the symmetry. The usual $\sin^l \theta$ power expansion of anisotropies in Eq. (5.1) are not orthogonal functions and so do not produce accurate temperature-dependent constants with our ASD simulations. For time-dynamic solutions using the LLG equations of motion, this is especially important due to the torque derivatives necessary to produce the effective field creating anisotropy terms of different order. Specifically, this is a problem for the 2^{nd} and 4^{th} order uniaxial contributions $K_{2\perp}$ and $K_{4\perp}$, respectively, in Eq. (5.1). We therefore express the uniaxial anisotropies as an orthogonal function following the spherical harmonic expansions shown in [147]. The 4^{th} order in-plane term corresponding to $K_{4\parallel} \sin^4 \theta \cos 4\phi$ is already orthogonal in the Cartesian basis, and can be expressed in Cartesian coordinates the following way:

Substituting into the energy density expression $E = K_{4\parallel} \sin^4 \theta \cos 4\phi$ using $\cos 4\phi = 8\cos^4 \phi - 8\cos^2 \phi + 1$ gives

$$\begin{aligned} E =& K_{4\parallel} \sin^4 \theta \left(8\cos^4 \phi - 8\cos^2 \phi + 1\right) \\ E =& K_{4\parallel} \left[8\sin^4 \theta \cos^4 \phi - 8\sin^4 \theta \cos^2 \phi + \sin^4 \theta\right]. \end{aligned}$$

The polar coordinate substitution uses $\sin^2 \theta = 1 - \cos^2 \theta$, giving:

$$E = K_{4\parallel}\left[8\sin^4\theta\cos^4\phi - 8(1-\cos^2\theta)\sin^2\theta\cos^2\phi + (1-\cos^2\theta)^2\right]$$
$$E = K_{4\parallel}\left[8\sin^4\theta\cos^4\phi - 8(1-\cos^2\theta)\sin^2\theta\cos^2\phi + 1 - 2\cos^2\theta + \cos^4\theta\right].$$

Substituting for $S_z = \cos\theta$, $S_x = \sin\theta\cos\phi$ then gives

$$E = K_{4\parallel}\left[8S_x^4 - 8S_x^2(1-S_z^2) + 1 - 2S_z^2 + S_z^4\right]$$
$$E = K_{4\parallel}\left[1 + 8S_x^4 - 8S_x^2 + 8S_x^2S_z^2 - 2S_z^2 + S_z^4\right].$$

Equivalently, the energy can be expressed in terms of S_y through the substitution $S_z^2 = 1 - S_x^2 - S_y^2$:

$$E = K_{4\parallel}\left[1 + 8S_x^4 - 8S_x^2 + 8S_x^2(1-S_x^2-S_y^2) - 2(1-S_x^2-S_y^2) + (1-S_x^2-S_y^2)^2\right].$$
$$E = K_{4\parallel}\left[1 + 8S_x^4 - 8S_x^2 + 8S_x^2 - 8S_x^4 - 8S_x^2S_y^2 - 2 + 2S_x^2 + 2S_y^2 - 2S_x^2 - 2S_y^2 + 2S_x^2S_y^2 + S_x^4 + S_y^4\right].$$

which reduces to give

$$E = k_{4r}(S_x^4 - 6S_x^2S_y^2 + S_y^4) \tag{5.3}$$

where $k_{4r} = K_{4\parallel}/2$ is the atomistic, rather than macroscopic, constant.

The 4$^{\text{th}}$ order uniaxial term follows a straightforward transformation to Cartesian coordinates using the identity $\sin^2\theta = 1 - \cos^2\theta$ and $S_z = \cos\theta$:

$$E = K_{4\perp}(1 - 2\cos^2\theta + \cos^4\theta)$$
$$E = K_{4\perp}(1 - 2S_z^2 + S_z^4)$$

Orthogonality is maintained by adding a small 2$^{\text{nd}}$ order contribution to match the spherical harmonic form in [147]. This shifts the anisotropy into the form:

$$E = k_4(S_z^4 - \frac{6}{7}S_z^2) \tag{5.4}$$

where $k_4 = K_{4\perp}/2$ and the constant value has been removed because it does not contribute to the energy landscape of the Hamiltonian. The contribution $\frac{40}{35}k_4S_z^2$ added to the 4$^{\text{th}}$ order term must be subtracted from the 2$^{\text{nd}}$ order term.

	$K_{2\perp}$	$K_{4\perp}$	$K_{4\parallel}$
Mn_2Au	-2.44	0.02	0.01
Au	-2.72	0.01	0.01
Mn_2	0.28	0.01	0.00

Table 5.1 Element resolved anisotropy constants from Shick *et al.* [148]. Units in meV per f.u..

The dominant anisotropy is the two-ion, 2$^{\text{nd}}$ order, uniaxial term with a negative component, giving a large in-plane preference for the magnetisation. The two-ion contribution occurs from large spin-orbit coupling in the Au layers enhancing the $3d-5d$ exchange splitting [41]:

$$E = -k_{2\perp}^{5d}\chi^2 \sum_{\alpha,ij} J_{3d-5d}^{i,\alpha} J_{3d-5d}^{j,\alpha} M_{3d,z}^{i,\alpha} M_{3d,z}^{j,\alpha}$$

χ is the local spin susceptibility and $k_{2\perp}^{5d}$ is proportional to the spin-orbit coupling parameter ξ_{5d}^2, determined through self-consistent second-variational procedure. Table 5.1 gives the element resolved contribution to the three anisotropies in Eq. (5.1). The $J_{3d-5d}^{i,\alpha} M_{3d,z}^{i,\alpha}$ term above suggests that the two-ion contribution is proportional to the Au and Mn bonds. We have used this proportionality and the J_1 and J_2 exchange couplings to describe the calculated anisotropy constant $K_{2\perp}$ as a tensorial correction to the exchange constants [143]. (While Shick *et al.* do not report the SOC parameter for the Au species, [56] estimate an effective SOC coupling parameter $\xi = 46$ meV from the energy shift between the $d_{3/2}$ and $d_{5/2}$ resonances).

This is done by relative weight of the exchange constants J_1 and J_2. First, the easy plane anisotropy is given by $K_{2\perp} = 2.44$ meV/f.u which becomes -1.95444×10^{-22} J/atom. Removing the 2$^{\text{nd}}$ order component added to the 4$^{\text{th}}$ order term $k_{2\perp} = -1.95444 \times 10^{-22} - 1.60218 \times 10^{-24} * 40/35 = -1.9727506 \times 10^{-22}$ J / atom. Note this value is already the

one shown in Table 2.1. Then, the relative exchange contributions determine the two-ion distribution: the total isotropic AFM exchange is $-(4*1.0942959+1*1.469234)\times10^{-20}=-5.8464176\times10^{-20}$ J/atom. The fractional contributions to the exchange are:

$$J_1/J_{AFM}=\varepsilon_1=1.0942959/5.8464176=0.18717374893$$
$$J_2/J_{AFM}=\varepsilon_2=1.4692340/5.8464176=0.25130500428$$

The contribution of the anisotropy to each exchange value is then

$$k_{2\perp}J_1/J_{AFM}=0.18717374893*1.9727506\times10^{-22}=0.00369247125\times10^{-20}\text{ J/atom}$$
$$k_{2\perp}J_2/J_{AFM}=0.25130500428*1.9727506\times10^{-22}=0.00495762097\times10^{-20}\text{ J/atom}$$

An exchange tensor incorporates the isotropic and 2-ion exchange contributions $\mathbf{J}_{ij}^T$, with $J_{xx},J_{yy},J_{zz}+\varepsilon_j k_{2\perp}$ for inter-sublattice interactions as an addition to the usual isotropic terms [149]. Note that the anisotropic contribution values $<10^{-26}$ can be truncated due to the time-step size.

We combine the exchange tensor above with Eqs. (5.4) and (5.3) to give the new atomistic spin Hamiltonian:

$$\mathcal{H}=-\sum_{i<j}\mathbf{S}_i\mathbf{J}_{ij}\mathbf{S}_j-k_4\sum_i\left(S_{i,z}^4-\tfrac{6}{7}S_{i,z}^2\right)-k_{4r}\sum_i(S_{i,x}^4-6S_{i,x}^2S_{i,y}^2+S_{i,y}^4). \tag{5.5}$$

We make two notes regarding the two-ion anisotropy composition above. First, for a more complete description of the effect of the two-site polarisation on exchange, one would have to redo the *ab initio* calculations of Schick *et al.* with site-resolved contributions for exchange and construct the spin Hamiltonian from those data. This would include the effect of the two-ion source on the 4$^{\text{th}}$ order uniaxial and in-plane anisotropies. This effect, however, is minimal compared to the dominant 2$^{\text{nd}}$ order anisotropy. Second, Shick *et al.* calculate element specific contributions to the anisotropy orders. With minimal spin-orbit coupling on the Mn terms (see column $K_{4\|}$ in Table 5.1), it is likely that only the Au contribution is enhanced by the Mn exchange splitting. Thus, the 2$^{\text{nd}}$ order anisotropy is likely a combination of single and two-ion

contributions, though the two-ion contribution (-2.72 meV/f.u.) is larger than the single-ion (0.28 meV/f.u.).

5.2.2 Domain Wall Analysis

In Chapter 4 we previously gave the formalism describing a 90° DW. That formalism is extended to this chapter in order to study the temperature-dependent magnetic properties of our new Hamiltonian, as well as the effects of DW driving at elevated temperatures. The fundamental Hamiltonian used in Chapter 4, expressed here for reference, described the in-plane 4^{th} order anisotropy using a tetragonal form:

$$\mathcal{H}(\mathbf{n},\mathbf{l}) = \frac{1}{2}A\mathbf{n}^2 + \frac{1}{8}a(\partial_x\mathbf{l})^2 + |K_{2\perp}|(\mathbf{l}\cdot\hat{z})^2 - \frac{K_{4\perp}}{2}(\mathbf{l}\cdot\hat{z})^4 - \frac{K_{4\parallel}}{2}\left[(\mathbf{l}\cdot\hat{x})^4 + (\mathbf{l}\cdot\hat{y})^4\right], \tag{5.6}$$

This can be shown to be equivalent to the Hamiltonian in Eq. (5.5) by returning to the generic tetragonal basis. Then, considering only the in-plane anisotropy due to the sine-Gordon dependence only on k_{4r}, the in-plane tetragonal form for a generic basis is:

$$E = \frac{K_{4\parallel}}{2}\left[(\mathbf{S}_i\cdot\hat{\mathbf{u}}_1)^4 + (\mathbf{S}_i\cdot\mathbf{u}_2)^4\right] \tag{5.7}$$

$\hat{x}$, $\hat{y}$ and $\hat{z}$ represent the unit Cartesian basis with $\hat{\mathbf{u}}_1 = \frac{1}{\sqrt{2}}(\hat{x}+\hat{y})$ and $\hat{\mathbf{u}}_2 = \frac{1}{\sqrt{2}}(\hat{x}-\hat{y})$ for the easy axes along $\pm\pi/4$. This can be re-written in spin-component form as

$$E = \frac{K_{4\parallel}}{2}\left[\left[\frac{\mathbf{S}_i\cdot(\hat{x}+\hat{y})}{\sqrt{2}}\right]^4 + \left[\frac{\mathbf{S}_i\cdot(\hat{x}-\hat{y})}{\sqrt{2}}\right]^4\right]$$

This leaves

$$E = \frac{K_{4\parallel}}{8}\left[(S_{ix}+S_{iy})^4 + (S_{ix}-S_{iy})^4\right]$$

$$E = \frac{K_{4\parallel}}{8}\left(S_{ix}^4 + 4S_{ix}^3S_{iy} + 6S_{ix}^2S_{iy}^2 + 4S_{ix}S_{iy}^3\right) + \left(S_{iy}^4 + S_{ix}^4 - 4S_{ix}^3S_{iy} + 6S_{ix}^2S_{iy}^2 - 4S_{ix}S_{iy}^3 + S_{iy}^4\right)$$

which after gathering terms reduces to the the Cartesian expression in Eq. (5.5) and inserting the atomistic anisotropy for the macroscopic constant gives:

$$E = \frac{k_{4r}}{8}\left(S_{ix}^4 + 6S_{ix}^2 S_{iy}^2 + S_{iy}^4\right). \tag{5.8}$$

The rotated easy axes in Eq. (5.6) can be recovered directly from Eq. (5.7) by letting $\hat{\mathbf{u}}_1 = \hat{x}$ and $\hat{\mathbf{u}}_2 = \hat{y}$. By comparing the coefficients in Eqs. (5.8) and (5.6) to the expression in Eq. (5.3), it is apparent a factor of eight connects the two formalism. This exists as a factor of two between the macroscopic and atomistic constant and a factor of four between the Cartesian expressions. Thus, while the analytic descriptions of the DWs in Chapter 4 apply to the results in this Chapter, a factor of eight is needed in the DW width factor to bring parity between the spherical description in Eqs. (5.1) and (5.3) and the tetragonal description in Eq. (5.7). Since this change in coefficients occurs at the level of the Hamiltonian, the DW width itself is affected, rather than it being a superficial change to the analysis. As such, this Chapter will continue under the Hamiltonian introduced in Eq. (5.5), with the relevant changes made to the coefficients in the sine-Gordon solution. This factor can be introduced to the sine-Gordon Hamiltonian in Eq. (5.6) with a change only in the coefficient of the resultant DW width factor Δ_0. Since we are interested in the temperature-dependent properties of the DW, we include in our notation now the temperature-variable exchange and anisotropy parameters for the DW width factor.

$$\Delta(0) = \sqrt{\frac{A(0)}{4 \cdot 8K_{4\|}(0)}} = 8.65 \text{ nm} \tag{5.9}$$

The DW width factor enters into the spatial dependence of the in-plane azimuthal angle the same way in Eq. (4.16), repeated here for reference:

$$\phi = \left(\arctan\left(\exp\left\{\frac{x - x_0}{\Delta(0)}\right\}\right) - \pi/4\right) \tag{5.10}$$

For comparison with experimental results, the solution given by the sine-Gordon equation may no longer reflect the physical nature of the DW. In particular, the Bloch definition given

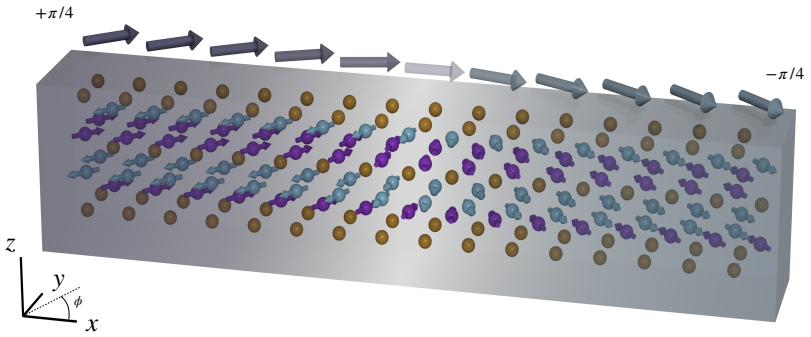

Fig. 5.1 90° DW lattice profile. Arrows above show the Néel vector along the DW direction $\hat{x}$.

by $\Delta(0)$ does not reflect the length that the magnetic texture occupies extent between the two domains. As a consequence of this, it is possible to represent the DW width in such a way that it accounts for the slope of the in-plane azimuthal angle, ϕ, which translates into a value δ_{dw} through the conversion $\delta_{\mathrm{dw}} = 2\pi\Delta(0)/\sqrt{2}$. These scaled values are the ones reported in the results and so called the DW width, as opposed to $\Delta(0)$ the DW width factor.

5.2.3 Simulations

Computationally, we perform ASD simulations on systems with variable length along x and set width and height of $(l \times 7.7 \times 7.7)$ nm^3 with periodic boundary conditions along y and z. For systems without excitation, we use a 1000 nm track. For DW driving, we use up to 3000 nm. The DW direction along x gives no variation in y or z, and we confirm our operation in the exchange limit by fitting the DW width factor to the magnetisation of atomically thin slices along y and z with minimal statistic variance. In order to better collect thermodynamic data in the microcell approximation, we fit Eq. (5.11) to the average magnetisation in atomically thin microcells with dimensions $0.65 \times 7.7 \times 0.14$ nm^3. This allows an approximation for the sublattice magnetisation expectation value $\langle m_e(T)\rangle = \langle \mathbf{m}\rangle / \mathrm{m}_s$ above 0 K. To fit the microcell magnetisation to the DW width factor and DW centre x_0, we use a modified Eq. (4.17) from Chapter 4:

$$m_e(T)\sin\phi = m_e(T)\sin\left(\arctan\left(\exp\left\{\frac{x-x_0}{\Delta(T)}\right\}\right)-\pi/4\right) \tag{5.11}$$

where $m_e(T)$ is either the microcell average or the calculated value from the modified phenomenological Curie-Bloch law in Eq. (2.17). The modified Curie-Bloch law gives excellent agreement to the experimental magnetisation (see Fig. 2.5), and allows for rescaling of the temperature term in the Langevin thermostat to better reflect the quantum nature of the stochastic field (Eq. (2.16)).

For the DW, we initially directed half of the Mn sublattices of the system along the $[110]$ and $[-1-10]$ directions, while the other half have been defined between the $[1-10]$ and $[-110]$ axes. The spatially inhomogeneous region between both domains was initialised according to the expected soliton solution given in Eq. (4.17). Subsequently, the system was first thermalised using a Monte Carlo preconditioning algorithm, then allowed to equilibrate for 20 ps, followed by 80 ps of data collection (250 ps for driving simulations). At elevated temperatures, the DW becomes highly diffusive. We compensate for this by fitting Eq. (5.11) to each configuration snapshot, allowing the determination of the wall width parameter $\Delta(T)$. At $T = 0$ K we find $\Delta(0) = 8.64$ nm, in very good agreement with the analytic value $\Delta(0) = 8.65$ nm.

Experimental measurements of the macroscopic Gilbert damping suggest a low value of $\lambda_G = 0.008$ [20]. Due to the high degree of crystalline order, we explore a range of atomistic damping constants $\lambda = 0.1 - 0.001$.

5.3 Results

5.3.1 Temperature-dependent anisotropy

For the temperature dependence of the anisotropy and exchange stiffness, we use a constrained Monte Carlo calculation [50] with an adaptive move [49] (see Chapter 2). 5000 averaging MC steps per temperature point gives low variance in the magnetisation. Due to the symmetry of the system, we are able to separate the rotational anisotropy in the $x-y$ plane from the polar contributions along the z-axis by choosing special constraint angles in the CMC simulations. The restoring torques for the rotational anisotropy are given by $\boldsymbol{\tau} = -\nabla E_{4r}$ which for the special

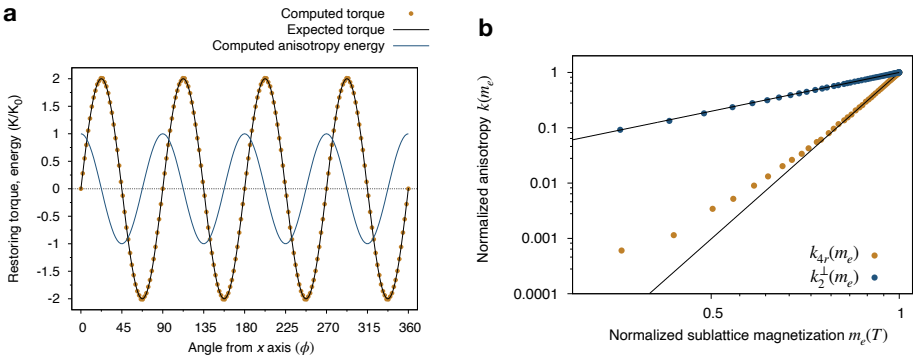

Fig. 5.2 Anisotropy geometry and temperature scaling. (a) Simulated torque curve and anisotropy energy for the rotational anisotropy of Mn_2Au at $T = 0$ K, normalised to the rotational anisotropy constant k_{4r} compared to the analytical result. (b) Computed temperature dependent normalised anisotropies (points) $k_2^{\perp}$ and k_{4r} plotted against the normalised sublattice magnetisation $< m_e >$. Lines show low-temperature fits to the expected temperature dependent scaling of $k_2^{\perp}(n) = n^{2.32}$, expected for pure 2-ion anisotropy [150, 149], and $k_{4r}(n) = n^{9.77}$, expected for 4$^{\text{th}}$ order rotational anisotropy from the ZACC scaling law.

case of $\theta = 90°$ is $\tau_z|_{\theta=90°} = 4k_{4r}\sin 4\phi$. For the case of $\theta = 90°$, the azimuthal anisotropies $k_2^{\perp}$ and k_4 both have zero torques $dE/d\theta, \phi|_{\theta=90°} = 0$ and so do not contribute to the torque curve. The simulated total torque and corresponding anisotropy energy are shown in Fig. 5.2a. It can be seen that there is a maximum for the torque at $\phi = 22.5°$ and so we use this point to calculate the temperature dependent anisotropy, applying a quadrature rule [50] to determine the integral of the torque using a single constraint angle.

Uniquely determining the temperature scaling of the large easy-plane anisotropy using quadrature as above is not possible due to the presence of a finite torque from the rotational 4$^{\text{th}}$ order component; however, it is possible to remove the torque arising from the 4$^{\text{th}}$ order uniaxial anisotropy by choosing a suitable angle of theta where the 4$^{\text{th}}$ order torque is zero, given by $\theta = \arccos\left(\sqrt{15/35}\right) \approx 49.1°$. Since the easy-plane anisotropy $k_2^{\perp}$ is an order of magnitude larger than the rotational torque, removing the uniaxial torque allows us to uniquely determine the scaling of the easy-plane anisotropy, using a single angle calculation at $\theta = 49.1°, \phi = 0$ and applying the quadrature rule.

The scaling of the anisotropies with the sublattice magnetisation m_e is shown in Fig. 5.2b. At low temperatures the anisotropies follow the expected scaling relations, fit by $k'_{2\perp}(m_e) = k_{2\perp} m_e^{2.32}$ for two-ion [150] and $k'_{4r}(m_e) = k_{4r} m_e^{9.77}$ for the 4$^{\text{th}}$ order anisotropy. Although not presented here, the 4th order uniaxial anisotropy k_4 follows the same scaling relation as the rotational term, with $k'_4(m_e) = k_{4r} m_e^{10}$. The temperature-dependent sublattice magnetisation follows the modified Curie-Bloch scaling law Eq. (2.17), allowing parametrisation of the anisotropy scaling $(K(T))$ with temperature instead of magnetisation.

5.3.2 Temperature-dependent exchange stiffness in Mn_2Au

Due to the different directionality of the exchange interactions in the unit cell, where the AFM contribution denoted by J_1 contributes both along the thickness of the sample and through a non-zero projection on the xy FM basal planes, it becomes complex to find constriction angles to isolate their individual effects as we did with the anisotropy-based contributions. Instead, the effective single-moment exchange stiffness can be calculated by sampling the thermodynamic energy landscape of a Néel vector fixed *in-plane*, rotated through its antiparallel to perpendicular state along the $\hat{x}$ coordinate to produce a spin-spiral, at increasing temperatures. In the exchange limit that the magnetic texture along $\hat{y}$ and $\hat{z}$ remains uniform and the spin gradient along $\hat{x}$ is small, this method gives the exchange stiffness $A(T)$ for increasing temperature.

Fig. 5.3 shows the scaled anisotropy constant and exchange stiffness with increasing temperature. Our calculation gives an $A(0)$ value of 2.91×10^{-11} J/m–a value dependent on the exchange constants used. The temperature dependence of A gives a good fit to the scaling law $m_e(T)^{1.83}$. This scaling matches well with the expected FM-like trends in AFM materials with 2-ion anisotropy according to Rózsa and Atxitia [150]. We note that this exponent arises from a fit over the whole temperature range, which is used later to parametrise the temperature dependence of the domain wall width. A fit at low temperatures (< 200 K) gives an exponent of 1.68, agreeing with the value given in Ref. [150]. From spin wave theory, the departure from the FM exponent $2-\varepsilon$ by a value of $\varepsilon = 0.32$ ought to appear in the two-ion exponent as $2+\varepsilon$. A result which is indeed shown in Fig. 5.2. Combining our calculations for the temperature-dependent anisotropy and the exchange stiffness we are able to investigate the

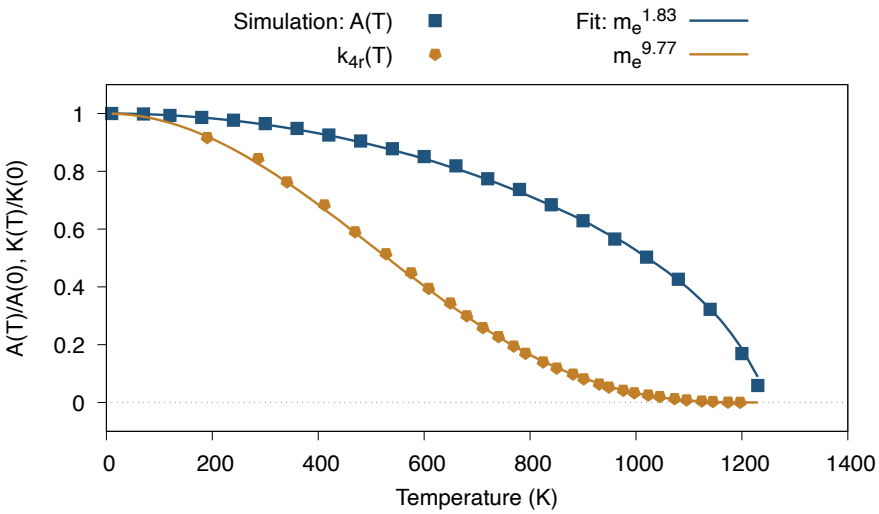

Fig. 5.3 Exchange stiffness and anisotropy stiffness calculations scaling with temperature. Low Temperature (< 200 K) fit for exchange stiffness returns an exponent of 1.68.

temperature dependence of the DW width for a direct comparison with the computational results in the following section.

5.3.3 Temperature dependent domain wall width

Sapozhnik *et al.* [128] report a DW best fit using the ratio $0.5 \times 10^{-4} \leq 8K_4/(|J_1|+2J_3) \leq 2 \times 10^{-4}$. A difference in the configurational energy based on the f.u. cell (Sapozhnik *et al.* Eq. 2) vs geometric unit cell (Eq. (5.6)) gives a factor of 2 between the analytic results. This scales the Sapozhnik *et el.* fit for the f.u. cell correction ($1 \times 10^{-4} \leq 4k_{4rot}/(J_3^{xx} + |J_1^{xx}|/2) \leq 4 \times 10^{-4}$), giving a domain wall width w range of 7.37 to 30.37 nm. This relates to a δ_{dw} value of 14.73 to 60.74 nm. At 300 K our simulations calculate a DW width $\delta_{dw}(300K) = 2\pi/\sqrt{2}\Delta(300K)$ of 42 $\pm$4.5 nm, well within the experimental margin. It is important to note that Shick *et al.* calculate their $K_{4\|}$ value with an uncertainty of $\pm$50%. This gives an *ab initio* range of $27.17 \leq \delta_{dw} \leq 54.33$ nm. Recent, more precise, DFT calculations with a 25% uncertainty report $k_{4r} = 6.321 \times 10^{-25}$ [151]. Still well within our range of values.

In view of Eqs. (5.11) and (2.17) and the results in Sec. 5.3.1, a non-zero temperature will not only weaken the in-plane anisotropy-based energy landscape–blurring the magnetic soliton transition–but also reduce the sublattice magnetisation in the domains. Atomistically, this is

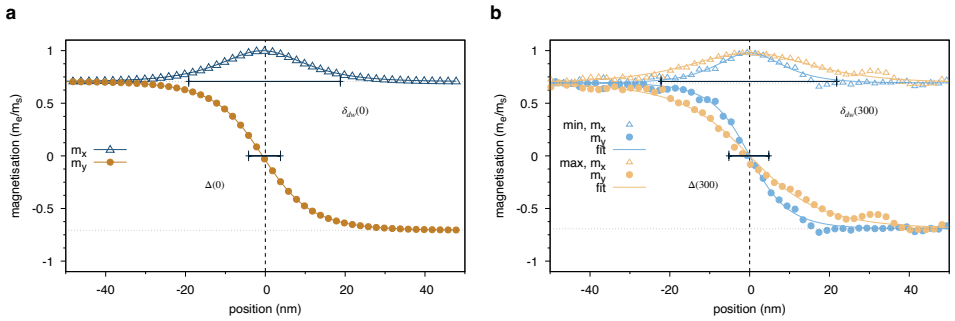

Fig. 5.4 DW sublattice magnetisation component profile for a) 0K, b) 300K. (light blue): minimum fit width and points. (gold): maximum fit width and points.

caused by fluctuating moments away from the easy axes. This has a result that as the thermal effects increase the DW spatial extent characterisation becomes less accurate, as it can be seen in Fig. 5.4. In addition, both the DW widths and positions must be extracted from the data, lest a time average of the magnetisation fail to capture the hard axis magnetisation profile.

Fig. 5.5 shows time resolved data averaged for several random seeds. The standard deviation is of the time-averaged positions for increasing damping constants, and is comparable to the DW diffusivity. The need for averaging over several random seeds to calculate the diffusivity is an artefact of the size of the simulation system: even small thermal field exerting an uncompensated torque at the DW centre–where the rotational anisotropy torque is maximum–will generate large in-plane fluctuations of the atomic magnetisation [152]. This is the same exchange enhancement phenomenon used to switch domains and drive DW walls in Chapters 3 and 4, respectively. Such excitations are also the cause of the sizeable variation of the average DW widths seen in Fig. 5.6.

MC simulations, by their very nature, minimise this broadening through a different thermal activation process than the Langevin thermostat, avoiding strong uncompensated fields. The MC simulations produce results analogous to LLG simulations with large damping in Fig. 5.5. Provided the DW is at thermodynamic equilibrium, the magnetisation averaging process in the MC simulation can reduce variations in width. The intrinsic a-dynamic nature of MC simulations can, however, lead to problems where the DW is stuck in a high energy configuration. Thus, at high temperature the large number of MC steps required for a sufficient average is computationally comparable to LLG simulations. A Fourier transform of the LLG

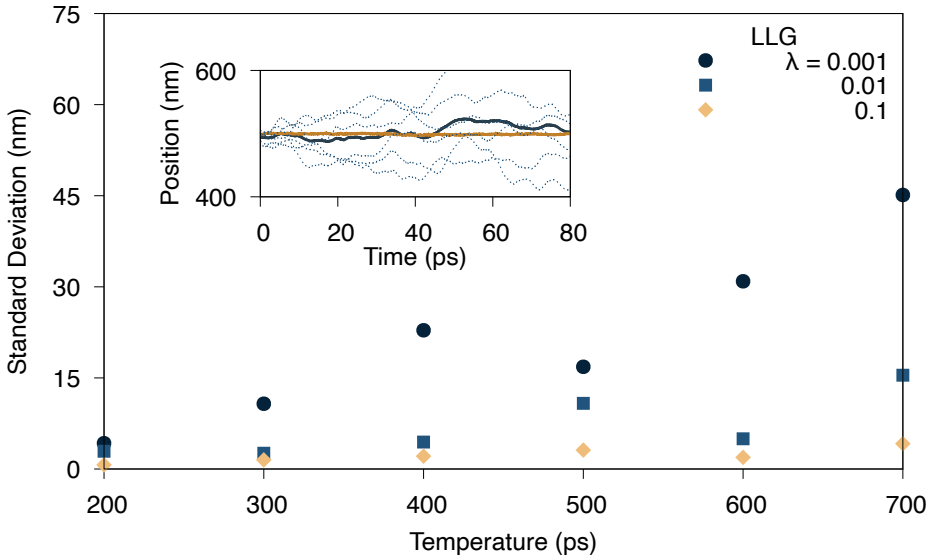

Fig. 5.5 DW random motion under thermal activation. Main: Standard deviation of the time-averaged positions for different random seeds for different damping parameters. Inset: Fit DW position at 300K for LLG random seeds with damping parameter $\lambda = 0.001$ and MC simulation. (Blue line): averaged LLG position. (Gold line): MC position. (Blue dashed): LLG random seeds.

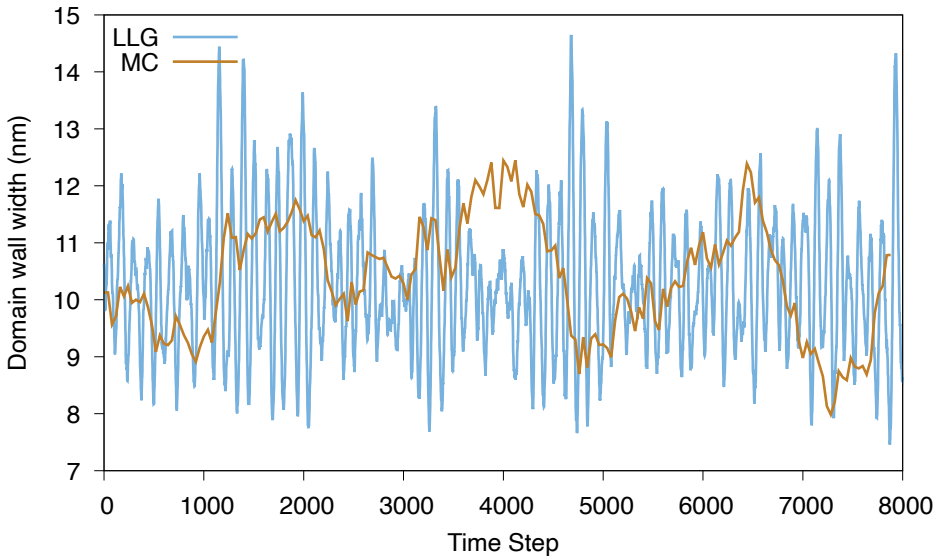

Fig. 5.6 Fit DW width factor during simulation for LLG and MC simulations. Temperature: 400K. $\alpha = 0.001$.

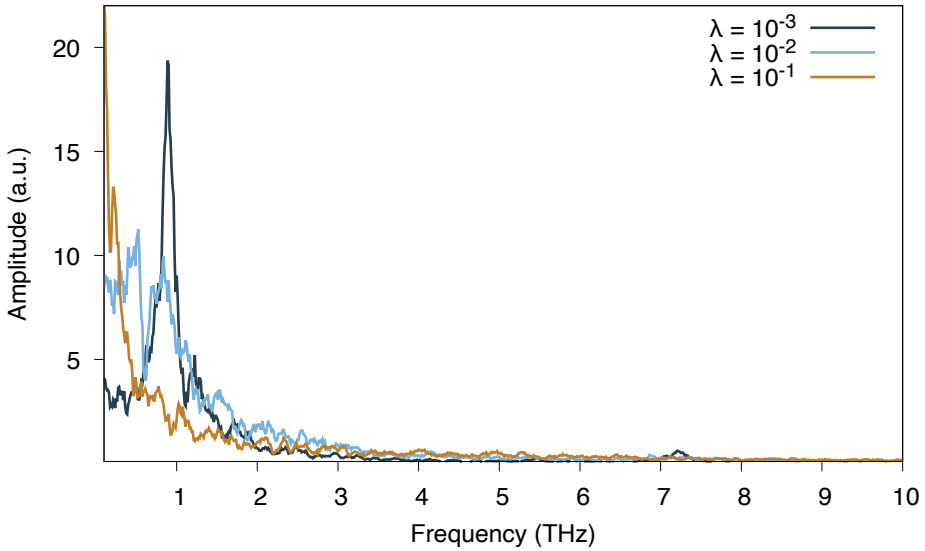

Fig. 5.7 FFT of the DW width for various LLG damping parameters.

simulation time resolved data from Fig. 5.6 shows clear activation of a THz mode at 0.88 THz (Fig. 5.7), which is a DW–rather than AFM–mode proportional to $\sqrt{k_{4r}}$ [104] (despite its close value to the THz AFM mode in Eq. (2.26)). The FFT in Fig. 5.7 for $\alpha = 0.001$ and $\alpha = 0.01$ show peaks at ≈ 0.88 THz. Increasing damping contributes larger thermal noise and suppresses the lifetime and effect of the excitation.

Analytically, the results in Secs. 5.3.2 and 5.3.1 make their way into the DW width factor by way of Eq. (5.11). When discussing the exchange stiffness and anisotropy scaling with DWs, however, it is more common to utilise hyperbolic solutions for the spatial dependence of ϕ [153–155]. There, the DW width factor is a direct calculation from $A(T)$ and $K(T)$:

$$\Delta(T) = \frac{2}{\pi}\sqrt{\frac{A(T)}{K(T)}}. \tag{5.12}$$

where the factor of $\pi/2$ allows conversion between the width factor in Eq. (5.12) and the width factor derived for the sine-Gordon Hamiltonian used in Eq. (5.10).

For comparison between the simulations and parametrised results in Fig. 5.8 we normalise the width factor to the $T = 0$ K value of $\Delta(0)$ from Eq. (5.9). Taking the fit values from Fig. 5.3, we describe the DW width factor as a parametrised function of temperature:

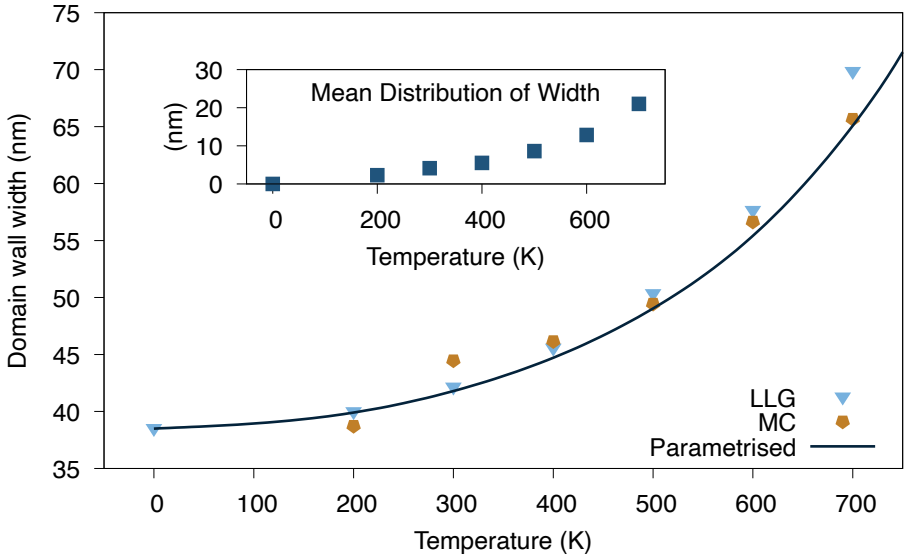

Fig. 5.8 Temperature dependence of the average domain wall width for a 90° domain wall. We see no statistical difference between fit DW widths for various damping constants. Inset: mean of the distribution of the fit widths from thermal activation for $\lambda = 0.001$. Larger damping reduces these distributions, rather than the width itself.

$$\Delta(T) = \Delta(0)\sqrt{\frac{m_e(T)^{1.83}}{m_e(T)^{9.77}}}. \tag{5.13}$$

The average DW width factors at finite temperature during 80 ps of simulations thus give good agreement with the width factor calculated from Eq. (5.14). For easy description of the DW width factor based only in temperature and not the magnetisation, the modified Curie-Bloch law which gives the sublattice magnetisation as a function of temperature (Eq. (2.17)) can be inserted into Eq. (5.13) and reduced to give:

$$\Delta(T) = \Delta(0)\left(1 - \left(\frac{T}{T_N}\right)^2\right)^{-1.318} \tag{5.14}$$

where for our constants $T_N = 1225$ K. It is important to note, however, that the parametrisation above may not be true for cases where the magnetisation does not follow the modified Curie-Bloch law in Eq. (2.17), as will be shown later for TTM simulations.

Fig. 5.8 shows the average DW widths for increasing temperature for LLG and Monte Carlo simulations compared to the equation parametrised from the exchange and anisotropy scaling

with temperature Eq. (5.14). We see no significant difference in the average widths calculated from the Monte Carlo simulations or LLG simulations with varying damping parameters. Thermal activation of the DW boundary causes oscillations to the soliton's instantaneous width profile, giving a distribution of values which increases with temperature. The averaged data agrees strongly with the parametrised calculation, up to the temperature threshold where thermal activation can overcome the in-plane anisotropy barrier ($\approx$ 800 K).

5.3.4 Domain Wall Motion

The effect of increasing temperature on DW motion can be qualified into two categories: diffusion, which is the nature of the DW to drift under stochastic conditions, and viscosity, which is how easily the DW moves under a driving force. Qualitatively, it is understood that DWs become more mobile at increased temperature. The velocity for 90$\circ$ DWs driven by the LOT in Chapter 4 can be given by:

$$v_{LOT} = 2\gamma H^{LOT} \Delta(T)/\alpha \tag{5.15}$$

Approximating the minimal temperature impact to α, this equation should scale with the DW width factor. To compare with the 0 K results presented in Chapter 4, we equilibrate then excite a DW using the anisotropy constant $k_{4\parallel}$ and the tetragonal Hamiltonian in Eq. (5.6). This has a 0 K DW width factor $\Delta(0) = 50.2$ nm (giving a DW width δ_{dw} far outside the experimental bounds [57, 156]). The width, however, does not change the analytic form of the equations to describe the DW at 0 K (as shown in Fig. 4.4), so we have not changed the results of Chapter 4 in light of the improved constants and Hamiltonian derived here.

At 300 K, the DW width factor $\Delta(300K)$, according to Eq. (5.14), is 54.46 nm. Eq. (4.21) then gives a steady-state, linear regime velocity of 30.7 km/s. Since this is an appreciable value of v_m, the steady-state Lorentz transformed velocity is only $\approx$ 25 km/s. The exact relationship between temperature and the magnon limit v_m–determined by exchange–is not known, as thermal excitation now involves the out of plane exchange constant J_2, previously irrelevant to the sine-Gordon solution, as well as the reduction of the exchange stiffness with

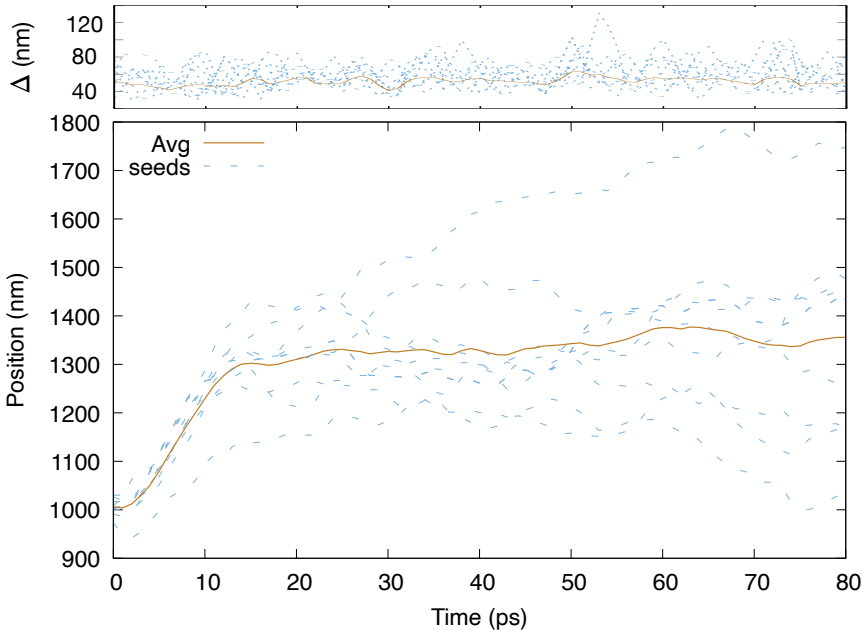

Fig. 5.9 LOT excitation position and width without laser heating effects. Laser excitation $I = 0.01$ GW/cm^2 follows a 10 ps Gaussian profile with no temperature change. The upper portion shows the average width (gold) and seed widths (blue).

decreased magnetisation at temperature. Thus, for simplicity we note only the comparison that the maximum velocity achieved in Fig. 5.9–a static temperature simulation–is ≈ 30 km/s, an apparent improvement in the driving efficiency predicted by the 0 K analytic descriptions.

As shown in Chapter 3, however, the effects of transient laser heating on the metallic system can have considerable impact to the magnetisation dynamics. To better simulate the effects of long pulse times on the DW, we involve the TTM introduced in Chapter 2 and utilised in Chapter 3. For pulse times beyond 10 ps, temperature dynamics between the magnetic thin film and the substrate need be taken into account. The TTM simulates this effect by phenomenologically cooling the phonon temperature to the starting temperature of the substrate (modelled as an infinite heat sink due to the large difference in heat capacities). The characteristic cooling time τ_e used in Eq. (2.23) is the time for the system to cool to half its maximum temperature. Since different substrates for Mn_2Au exist, we show the effect various characteristic cooling times have on the temperature dynamics in Fig. 5.10. $\tau_e = 100$ ps corresponds to slow cooling typical

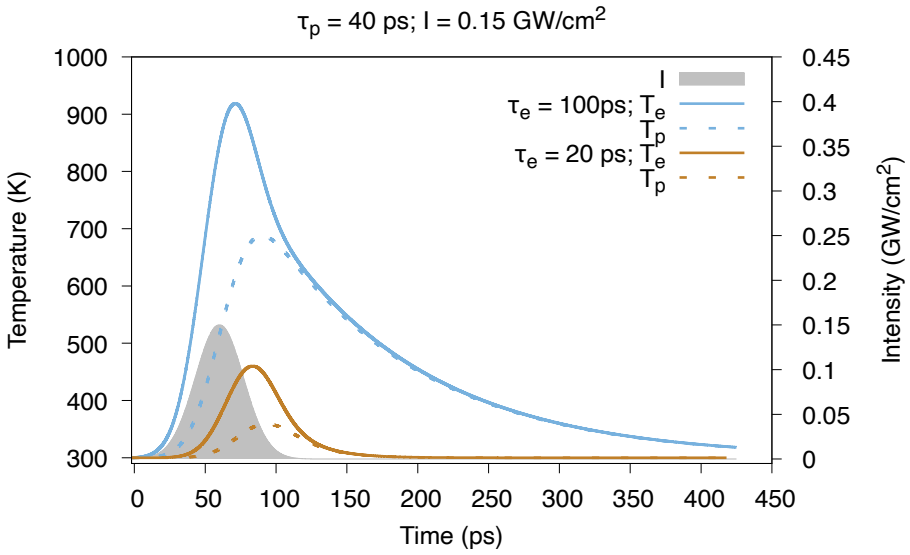

Fig. 5.10 TTM for two characteristic cooling times τ_e. Example laser intensity $I = 0.15$ GW/cm^2. The laser profile follows the second y axis.

of an insulating substrate [61], while $\tau_e = 20$ ps is more in line with a metallic HM substrate [157].

Moving towards simulating more physical DW models, we use the in-plane anisotropy constant k_{4r} and Hamiltonian in Eq. (5.5) which gives a DW width at 300 K $\delta_{dw}(300K) = 43$ nm. The commensurate width factor is $\Delta(300K) = 9.78$ nm. For a laser intensity $I = 0.075$ GW/cm^2, the induced H^{LOT} is 2.2 mT, giving a linear velocity of 15 km/s according to the 0 K results in Chapter 4. The resultant velocity in Fig. 5.11b shows the average DW velocity failing to meet this prediction, even when taking into account the larger width during laser heating. The diminished actual velocity compared to the calculated value could be a result of uncompensated stochastic fields in the Langevin term larger than the relatively minimal H^{LOT} causing nonphysical DW drift. However, removing the more spurious random seed paths shown in Fig. 5.11 increases the maximum velocity to only 7 km/s, compared to 3 km/s.

This suggests that rather than non-physical motion skewing the data, the diminished velocity is a result of finite size effects, akin to the super-paramagnetic effect for small magnetic domains. Since the driving mechanism for the DW is inertial rotation generated from exchange enhancement, even small changes to the S_z atomistic moments can overshadow the LOT. Larger

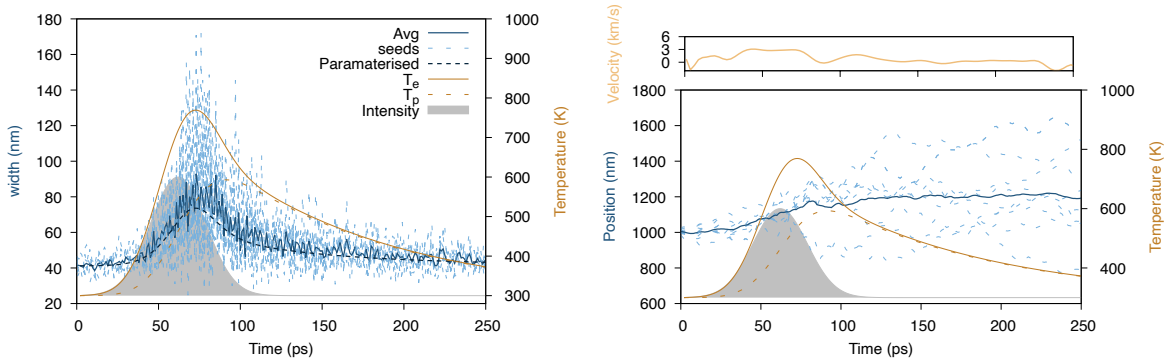

(a) Width **(b)** Position

Fig. 5.11 LOT driving including TTM for laser intensity $I = 0.075$ GW/cm^2 (total fluence $J = 12$ J/m^2). The parametrised width is according to Eq. (5.14) using the time resolved TTM electron temperature T_e.

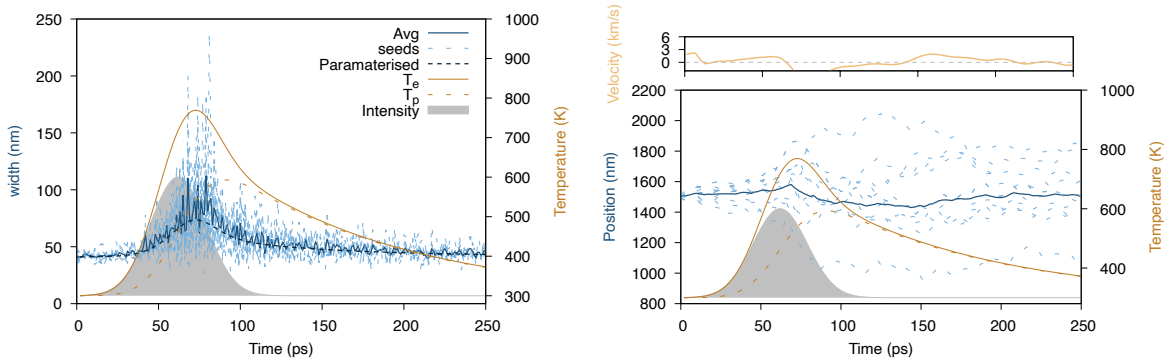

(a) Width **(b)** Position

Fig. 5.12 TTM with unpolarised light for laser intensity $I = 0.075$ GW/cm^2 (total fluence $J = 12$ J/m^2). The parametrised width is according to Eq. (5.14) using the time resolved TTM electron temperature T_e.

DW volume simulations are necessary to remove this effect, with increased lattice parameters along $\hat{y}$ and $\hat{z}$, rather than $\hat{x}$, in order to increase the DW volume. For comparison, we simulate a laser excitation using *unpolarised* light to study the effect of transient TTM heating on the DW without generated torque.

The TTM heating in Fig. 5.12 without LOT shows remarkable similarity to the LOT driving simulation in Fig. 5.11. The fit widths both show significant broadening which follows the parametrised prediction using the transient T_e from the TTM. The unpolarised simulation, however, does not show the same driving velocity in the LOT simulation, revealing there is a net effect of the LOT, even with finite size effects.

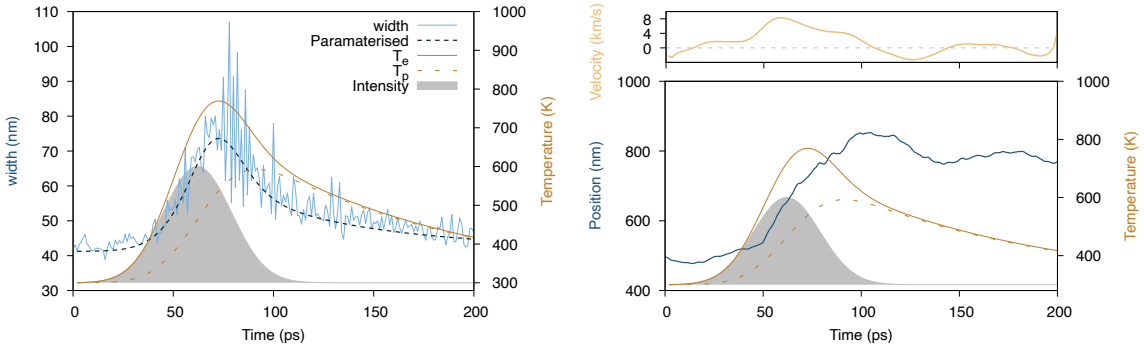

(a) Width **(b)** Position

Fig. 5.13 Largescale simulations with LOT driving including TTM for laser intensity $I = 0.075$ GW/cm^2 (total fluence $J = 12$ J/m^2). The parametrised width is according to Eq. (5.14) using the time resolved TTM electron temperature T_e.

Largescale simulations increasing the volume of spins around the DW reduce these excitations attributed to finite size effects. By increasing the depth of the lattice from 8 nm to 40 nm, spurious torques in the DW can be reduced. The width in Fig. 5.13a fits well the parametrised value using the TTM T_e, even without the averaging effect from many starting seeds. The effect of the LOT, by contrast, is clearly visible in the DW velocity (Fig. 5.13b) of the largescale simulation, reaching a peak velocity of 8 km/s.

The larger simulation size also allows simulation of increasing laser intensities. Despite multiple random starting seeds, the transient temperature increase from a $I = 0.1$ GW/m^2 laser pulse causes spontaneous nucleation of additional domains in the 8 nm deep simulations. Increasing the system depth to 40 nm removes this effect and shows increased DW velocity from the LOT, up to 12 km/s (Fig. 5.14). These velocities are still short of the predicted values from Chapter 4, and especially the values from Eq. 5.15 using the TTM width expansion. It is possible this is a continued effect of spurious torques on the DW–and thus larger simulations volumes would again see an increase in the velocity–but those results have not been confirmed.

5.4 Summary

We have analysed the temperature-dependent properties of Mn_2Au using ASD simulations using a robust first principles Hamiltonian and applied it to simulations involving dynamic temperature

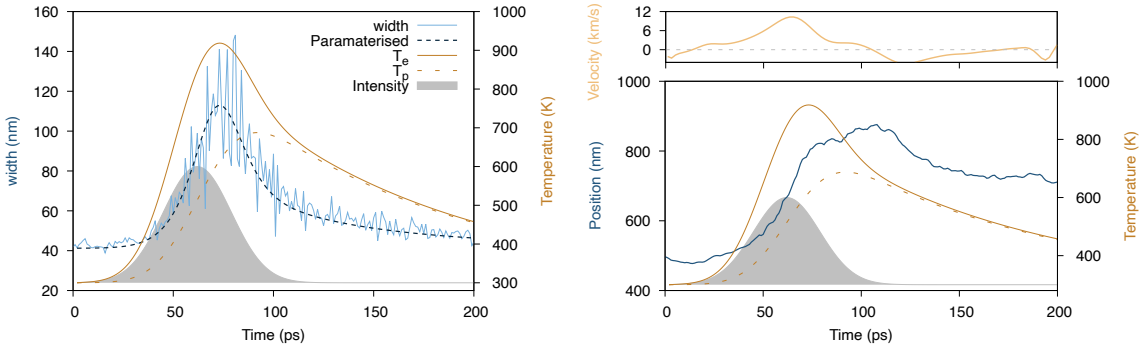

(a) Width **(b)** Position

Fig. 5.14 Largescale simulations with LOT driving including TTM for laser intensity $I = 0.1$ GW/cm^2 (total fluence $J = 16$ J/m^2). The parametrised width is according to Eq. (5.14) using the time resolved TTM electron temperature T_e.

and laser excitation. We first develop a magnetic spin Hamiltonian reflecting the origin of the dominant 2-ion anisotropy demonstrated in *ab initio* calculations in Ref. [142]. The temperature scaling for anisotropy and exchange–a critical component for micromagnetic simulations and traditionally difficult to calculate for AFMs–is calculated for Mn_2Au using a CMC spin-spiral at increasing temperatures. This method is confirmed by MC and LLG finite-temperature simulations of 90° DWs. Interestingly, increasing the value of the damping parameter does not affect the simulated width, but rather decreases the thermal width fluctuations around the average. The calculated exchange and anisotropy stiffness follows the well-known temperature-dependence for ferromagnets, as well as the AFM corrections present in literature [149, 150]. These calculations can allow large-scale micromagnetic simulations with high precision. The LOT used to drive DWs in Chapter 4 was also introduced to simulations at finite and dynamic temperature. These reveal the robust efficiency of AFM DWs even at elevated temperature, with low intensity pulses driving the DW at km/s speeds. With its high Néel temperature, metallic properties, and intrinsic spin-orbit torque response, Mn_2Au represents a crucial material for next-generation spintronic devices. With research pointing towards the critical role temperature plays in metallic spintronic devices [129], there is a growing need for accurate, finite-temperature simulations of DW and switching processes.

6

Spin Transport Model of the Intrinsic SOT in Mn_2Au

6.1 Introduction

Spin transport theory lies at the very heart of spintronics, providing the mechanism for coupling charge, spin, and the magnetic moment for non-equilibrium time-dependent processes. At a foundational level, spin transport is responsible for the giant magneto-resistance (GMR) effect which serves as the basis for magnetic memory storage in modern computers. Increasingly complex heterostructures utilizing atomically thin material layers allow for a staggering range of material combinations, with transport modelling theory a crucial tool for understanding the equivalently vast range of material parameters. Gone are the days of tri-layer FM/metal/FM systems. Now, metals, semi-metals, and semi-conductor stacks containing all range of ferromagnetic, ferrimagnetic, antiferromagnetic, spin polarising, and non-magnetic materials are possible. While the focus of this thesis is not on spin transport, we do devote a chapter of the results to work done on describing the intrinsic SOT phenomena for Mn_2Au using a spin transport formalism. Traditionally, the SOT arising from intrinsic CISP in Mn_2Au and CuMnAs is modelled using a Néel field-like torque–a staggered field addition to the LLG equation on each spin sublattice. At its source, however, the CISP inducing the staggered field is a spin transport phenomena, not a magnetic field phenomena. For bulk modelling, the distinction is

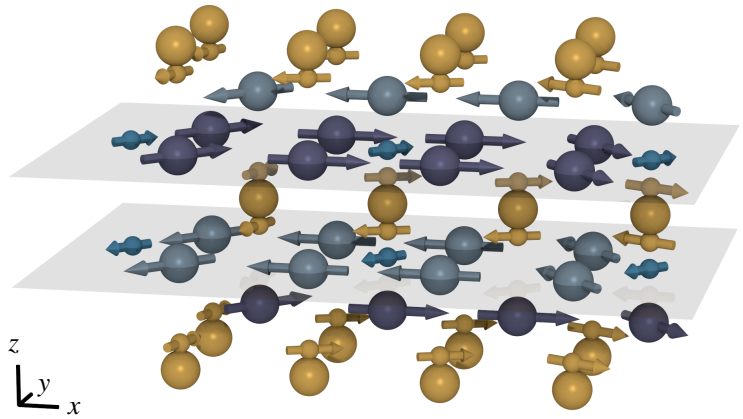

Fig. 6.1 Diagrammic representation of spin accumulation from a driving charge current polarised by the Mn moments (teal arrows) and Au SOI (gold arrows) across a domain wall.

irrelevant; for multilayer structures, or non-simplistic magnetic textures, the mechanisms differ widely. It is the latter scenario this chapter investigates.

DWs in traditional AFMs without intrinsic SOT can be driven using in-plane charge currents (which exert a torque on the DW from spin polarisation of the current passing through the magnetic domain) or from HM injected SOT (which exert a torque on the DW as well as the domains). For Mn_2Au, an in-plane charge current will do both, and the mechanism to simulate each phenomenon using ASD is the same. This chapter presents a description of our adapted spin transport model for describing coupled spin-magnetisation and current induced spin interactions–a result on its own–as well as the results of our model applied to simulations of DW driving in Mn_2Au.

6.2 Theory

To construct a model of the Néel vector-dependent and charge current vector-dependent induced spin accumulation leading to the intrinsic spin-orbit torque, we apply the Zhang-Levy-Fert

(ZLF) drift-diffusion formalism for spin transport to the Rashba-Edelstein effect responsible for the intrinsic SOT in Mn_2Au. This spin accumulation-based description is then applied to domain wall driving and single domain switching. Two mechanisms exist in the spin transport dynamics for domain wall driving. Firstly, the above mentioned intrinsic spin-orbit torque generated in Mn_2Au from a charge current. And secondly, the spin polarisation of the sublattice magnetisation driven by the charge current (i.e., spin motive force). While each mechanism operates through $s-d$ exchange coupling from spin polarisation at the Fermi level, the physical source differs between them. Here, the theoretical background for each mechanism is explored before being combined into our model.

6.2.1 Current Induced Spin Polarisation

At its source, the intrinsic SOT in Mn_2Au arises when a non-polarised charge current, moving in-plane, generates a staggered current induced spin polarisation (CISP) on each magnetic sublattice which results in a non-staggered torque (and consequently activating the exchange enhancement useful for switching). Traditionally, such a torque was achieved in AFMs through an extrinsic SOT generated by a heavy metal base layer (called the spin Hall effect (SHE)). Also available for broken inversion symmetry interfaces is the inverse spin Galvanic effect (ISGE). Qualitatively, the SHE and ISGE can both generate non-equilibrium spin polarisations which can exert a torque on the magnetic moment [1]. What differs is the underlying physical phenomena driving the interactions: while the SHE is a bulk effect from SOC, the ISGE occurs at the interface [159]. Fig. 6.2 gives a diagrammatic comparison between the SHE and ISGE. While naturally occurring (in some magnitude) for any interface with broken inversion symmetry at the band-structure level, the ISGE can exist for bulk materials as well, either through SOC or noncentrosymmetric crystal symmetry [12]. For FMs–where efficient switching and DW driving are highly dependent on torque symmetry and damping–often the ISGE is too weak for spintronic applications. For AFMs relying on exchange enhancement for efficient

[1] For the magnetic moment, there is no difference for ASD implementations between torques generated by the inverse SHE and ISGE other than that of symmetry: the SHE induces a predominately anti-damping-like torque, while the ISGE induces a predominately field-like torque. But field-like and anti-damping-like contributions to the SHE and ISGE, respectively, exist beyond the zero-order approximation [158]

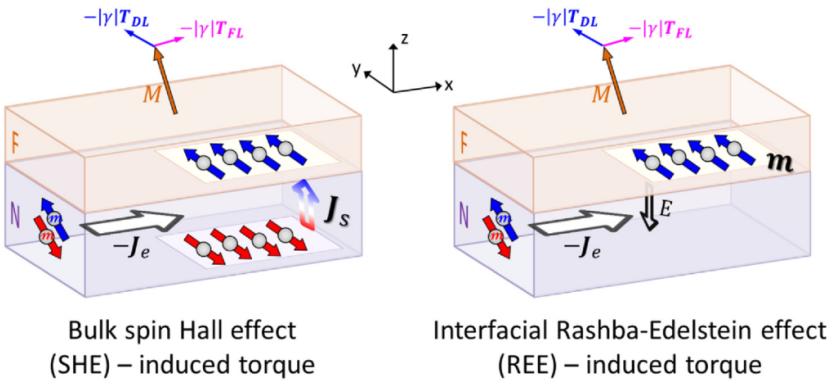

Fig. 6.2 Diagram of heterostructure-based spin torques arising from the SHE (left) and ISGE (right)–here called the interfacial Rashba-Edelstein effect. For the SHE, the SOC present in the 'N' non-magnetic layer induces a spin current perpendicular to the direction of the charge current. For the ISGE, a spin accumulation is generated only at the interface with broken inversion symmetry. Figure from [159].

driving, the ISGE allows an in-plane current to generate a torque on the magnetisation without heterostructures (i.e., heavy metal bilayers to inject spin polarised currents), though Mn_2Au and CuMnAs are so far the only metallic AFMs to exhibit this effect at room temperature [9].

At the DFT level, the change to the spin accumulation is not calculated by equations of motion (EoM) but by response functions. The quantum mechanical description of spin current $\mathbf{J}_s$–more accurately, the spin polarised flux density, but referred to as spin current here and in the literature–is described by the tensor product of the Pauli spin operator (related to spin operator $\mathbf{S} = \hbar\sigma/2$) and velocity operator $\mathbf{v}$ on the electron density ψ [159]:

$$\frac{\hbar^2}{4e}\mathbf{J}_s = \mathcal{R}e\left(\langle\psi|\sigma\otimes\mathbf{v}|\psi\rangle\right). \tag{6.1}$$

The Kubo linear response formalism expands the generic expression of Eq. (6.1) to include non-equilibrium changes to the charge density from the applied electric field $\mathbf{E}$ through the susceptibility tensor χ (such that $\delta\mathbf{m} = \chi\mathbf{E}$) [160]:

$$\delta\mathbf{m} = \frac{e\hbar}{2\pi V}\mathrm{Re}\sum_{\mathbf{k},a,b}\langle\psi_{\mathbf{k},a}|\hat{\mathbf{s}}|\psi_{\mathbf{k},\mathbf{b}}\rangle\langle\psi_{\mathbf{k},b}|\mathbf{E}\cdot\hat{\mathbf{v}}|\psi_{\mathbf{k},a}\rangle\times\left[G^R_{\mathbf{k},a}G^A_{\mathbf{k},b} - G^R_{\mathbf{k},a}G^R_{\mathbf{k},k}\right] \tag{6.2}$$

where $G^R_{\mathbf{k},a} = (G^A_{\mathbf{k},a})^* = (E_F - E_{\mathbf{k},a} + i\Gamma)^{-1}$, E_F is the Fermi energy, $E_{\mathbf{k},a}$ is the energy dispersion of band a, V is the system volume, and Γ is the broadening parameter connected to the finite lifetime $\tau = \hbar/(2\Gamma)$. $\delta\mathbf{m}$ ($\delta\mathbf{S}$ in Ref. [12, 160, 11] and Fig. 6.3 but changed in our text to avoid confusion with the atomic moment $\mathbf{S}$) is the current induced spin polarisation. The summation in Eq. (6.2) contains both $a = b$ (intraband) and $a \neq b$ (interband) contributions. Qualitatively, if the broadening parameter is small, Eq. (6.2) can be expanded into intra- and interband terms, with the interband terms further expanded to real and complex contributions, as $\delta\mathbf{m} = \delta\mathbf{m}^{\text{intra}} + \delta\mathbf{m}^{\text{inter}}_1 + \delta\mathbf{m}^{\text{inter}}_2$. Though the formalism in [160] is in the context of FMs, their use is extended by Železný *et al.* in [12] to Mn_2Au (or any AFM or FM with multiple sublattice species). With no loss of generality, we transition our notation to the description in [12] in terms of the susceptibility tensors $\delta\mathbf{m} = \chi\mathbf{E}$. For AFMs or multiple sublattice species, the susceptibility tensor χ becomes the susceptibility tensor χ_a for sublattice a. As with Eq. (6.2) χ_a is given as $\chi_a = \chi^{\text{I}}_a + \chi^{\text{II}(a)}_a + \chi^{\text{II}(b)}_a$:

$$
\begin{aligned}
\chi^{\text{I}}_{a,ij} &= -\frac{e\hbar}{2\Gamma}\sum_{\mathbf{k},n}\langle\psi_{n\mathbf{k}}|\hat{S}_{a,i}|\psi_{n\mathbf{k}}\rangle\langle\psi_{n\mathbf{k}}|\hat{v}_j|\psi_{n\mathbf{k}}\rangle \times \delta\left(\varepsilon_{\mathbf{k}n} - E_f\right) \\
\chi^{\text{II}(a)}_{a,ij} &= e\hbar\sum_{\mathbf{k},n\neq m}\text{Im}\left[\langle\psi_{n\mathbf{k}}|\hat{S}_{a,i}|\psi_{m\mathbf{k}}\rangle\langle\psi_{m\mathbf{k}}|\hat{v}_j|\psi_{n\mathbf{k}}\rangle\right] \times \frac{\Gamma^2 - (\varepsilon_{\mathbf{k}n} - \varepsilon_{\mathbf{k}m})^2}{((\varepsilon_{\mathbf{k}n} - \varepsilon_{\mathbf{k}m})^2 + \Gamma^2)^2}\left(f_{\mathbf{k}n} - f_{\mathbf{k}m}\right) \\
\chi^{\text{II}(b)}_{a,ij} &= 2e\hbar\sum_{\mathbf{k},n\neq m}\text{Re}\left[\langle\psi_{n\mathbf{k}}|\hat{S}_{a,i}|\psi_{m\mathbf{k}}\rangle\langle\psi_{m\mathbf{k}}|\hat{v}_j|\psi_{n\mathbf{k}}\rangle\right] \times \frac{\Gamma(\varepsilon_{\mathbf{k}n} - \varepsilon_{\mathbf{k}m})}{((\varepsilon_{\mathbf{k}n} - \varepsilon_{\mathbf{k}m})^2 + \Gamma^2)^2}\left(f_{\mathbf{k}n} - f_{\mathbf{k}m}\right)
\end{aligned}
\tag{6.3}
$$

where n, m are band indices, $\psi_{n\mathbf{k}}$ and $\varepsilon_{n\mathbf{k}}$ are Bloch eigenfunctions and eigenvectors, respectively, $f_{\mathbf{k},n}$ the Fermi-Dirac distribution, and $\hat{\mathbf{S}}_{a,i}$ the dimensionless spin-operator projected on sublattice a.

The separation of Eq. (6.2) into $\delta\mathbf{m} = (\chi^{\text{I}}_a + \chi^{\text{II}(a)}_a + \chi^{\text{II}(b)}_a)\mathbf{E}$ allows a qualitative understanding of the physical response to the applied field $\mathbf{E}$. The intraband term χ^{I}_a represents the electric field modification of the Fermi-Dirac carrier distribution. The susceptibility is inversely proportional to Γ, and diverges in the $\Gamma \to 0$ limit, analogous to the conductivity diverging in a perfectly periodic crystal [12]. As in Freimuth *et al.* in Chapter 3, at room temperature $\Gamma \approx 25$ meV

for an ordered metallic system with low impurities. This relates to a momentum scattering time $\tau = \hbar/(2\Gamma) \approx 13$ fs. Železný *et al.* extend the note that the susceptibility tensor χ_a^{I} can be obtained from the Boltzmann transport equation with constant scattering time.

The interband terms $\chi_a^{\mathrm{II}(a)}$, $\chi_a^{\mathrm{II}(b)}$ can be considered not as the distortion of the Fermi-Dirac distribution, but the distortion of the carrier particle wavefunctions (i.e., Berry curvature) [160]. While χ_a^{I} decays with increasing Γ, $\chi_a^{\mathrm{II}(b)}$ is directly proportional to increasing Γ, and thus has minimal contribution in the low Γ consideration. The final term $\chi_a^{\mathrm{II}(a)}$ is independent of the broadening parameter provided $(\varepsilon_{n\mathbf{k}} - \varepsilon_{m\mathbf{k}} \gg \Gamma)$. Thus, $\chi_a^{\mathrm{II}(a)}$ is the only *intrinsic* susceptibility tensor, not dependent on thermal or impurity scattering. Though the results for this chapter are simulated at 0 K (minimal broadening), the results utilising the LOT in previous chapters use a broadening value of $\Gamma = 25$ meV. For brief comparison, such a broadening value (comparable to 300 K) shifts $\chi_a^{\mathrm{II}(b)}(\Gamma = 25\text{ meV}) = -0.1\chi_a^{\mathrm{II}(a)}(\Gamma = 0\text{ meV})$, $\chi_a^{\mathrm{II}(a)}(\Gamma = 25\text{ meV}) = 0.75\chi_a^{\mathrm{II}(a)}(\Gamma = 0\text{ meV})$, and $\chi_a^{\mathrm{I}}(\Gamma = 25\text{ meV}) \approx 0.05\chi_a^{\mathrm{I}}(\Gamma = 0.0013\text{ meV})$ [12]. While the reduction to χ_a^{I} from increased broadening appears substantial, it is important to remember that the susceptibility tensors in Eq. (6.3) calculate only the CISP and provide rough estimates on the resulting generated torque. More comprehensive DFT calculations for the SOT using the Keyldish formalism estimate a torkance between 2-8 mT per 10^7 A/cm^2 [9, 161, 25]–matching well with experimental measurements [20]–compared to the CISP estimated value of 0.22 mT per 10^7 A/cm^2 [12]. Experimentally, charge current pulses have indeed been successful in switching the Néel vector at room temperature [13, 129, 14, 162].

The advantage of the tight-binding models (as opposed to full DFT calculations) is the tractable analytic descriptions of the resulting $\delta\mathbf{m}_a$ predicting the symmetry of the induced fields [11, 160, 12]. While the ISGE discussed above does not make explicit mention of the AFM order parameter, it is a critical factor when determining the torque symmetry, with the Néel vector naturally having a strong effect on the SOC mediated by the Au atoms (see Chapter 5). Fig. 6.3 shows the CISP for the tight binding 3D model and the 2D AFM model containing only a Rashba SOC. Generally, these follow the normal symmetries of injected SOT: the intraband ($\chi_{a,ij}^{\mathrm{I}}$) component follows $\hat{z} \times e\mathbf{E}$, with the interband ($\chi_{a,ij}^{\mathrm{II}(a)}$) component following

$\mathbf{m} \times (\hat{z} \times e\mathbf{E})$, where $\hat{z}$ is the Cartesian coordinate, usually out of plane. The current induced spin polarisation $\delta\mathbf{m}_a$ induces a field according to [12]:

$$\mathbf{B}_a = -J_{sd} \frac{\delta\mathbf{m}_a}{\mathbf{S}_a} \tag{6.4}$$

which produces a torque $\mathbf{T}_a$ perpendicular to the atomic moment $\mathbf{S}_a$:

$$\mathbf{T}_a = \mathbf{S}_a \times \mathbf{B}_a. \tag{6.5}$$

The work of Selzer *et al.* calculate the current induced spin and orbital polarisation using the linear response formalism [56]. There, the induced orbital moment is orders of magnitude larger than the induced spin moment and follows the zeroth-order Rashba symmetry in [12]. This results in staggered fields more than 10x larger than the torque calculated in [163]. Since we are interested in developing a model for spin currents, however, we do not consider the orbital contribution. A more developed model which takes into account spin and orbital accumulation (and the spin and orbital current interactions) is of interest for future research.

The CISP Mn sublayer specific response follows the Onsager relations for symmetry (i.e., $\chi_A^{\text{even}} = -\chi_B^{\text{even}}$; $\chi_A^{\text{odd}} = \chi_B^{\text{odd}}$). The Néel vector dependent spin accumulation induced on each Mn moment has been calculated, and is in line with the symmetry expected for the adiabatic (precessional) and non-adiabatic (damping-like) terms in the Slonczewski formalism.

Fig. 6.3a and c show the results of Eqs. (6.3) using the 3D Mn_2Au tight binding Hamiltonian described in [12], while b and d show the 2D AFM Rashba model. The 3D Hamiltonian calculation shows the accumulation deviating from the $\hat{z} \times e\mathbf{E}$ symmetry in the 2D model. We can parametrise the CISP (including the numerical deviations from the zeroth-order symmetries) using higher-order trigonometric functions:

$$\begin{aligned} \delta m_x/\delta m_\infty &= 0.5 \sin 2\phi \\ \delta m_y/\delta m_\infty &= 1.4 + \sin^2\phi \\ \delta m_z/\delta m_\infty &= -0.14 \cos\phi \end{aligned} \tag{6.6}$$

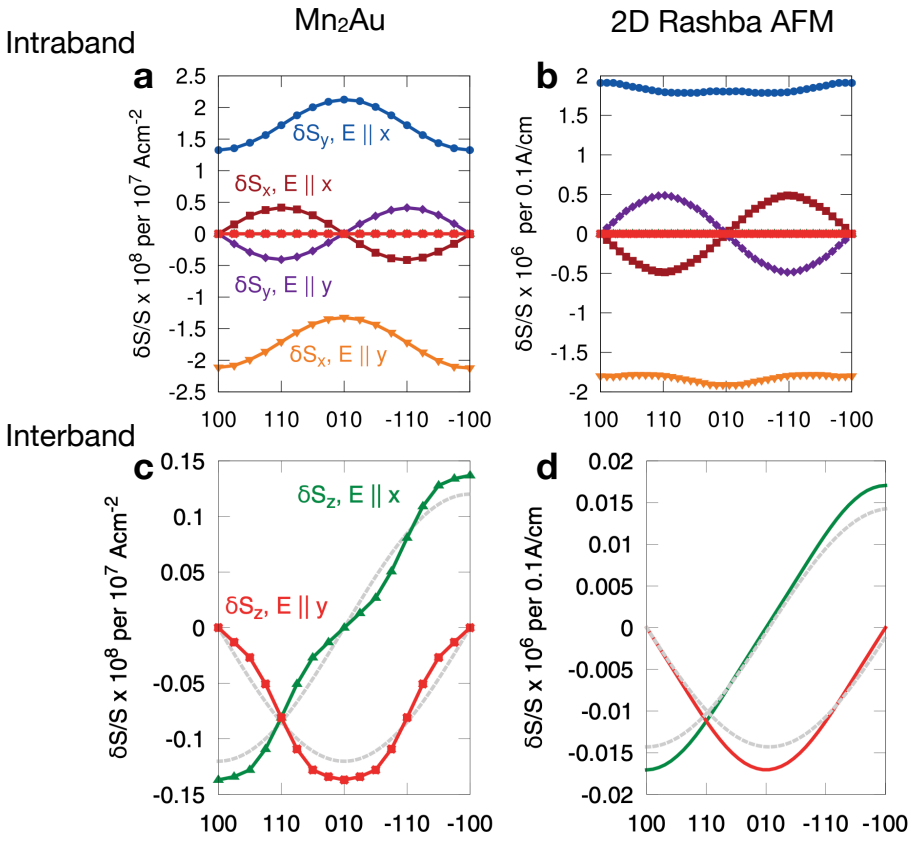

Fig. 6.3 Non-equilibrium spin polarisation for Mn_2Au and 2D AFM Rashba models. CISP induced from electric field $E \parallel x,y$ for intraband contribution (a, b) and interband contribution (c,d). x axis is the orientation of $\mathbf{S}_a$. Figure from [12].

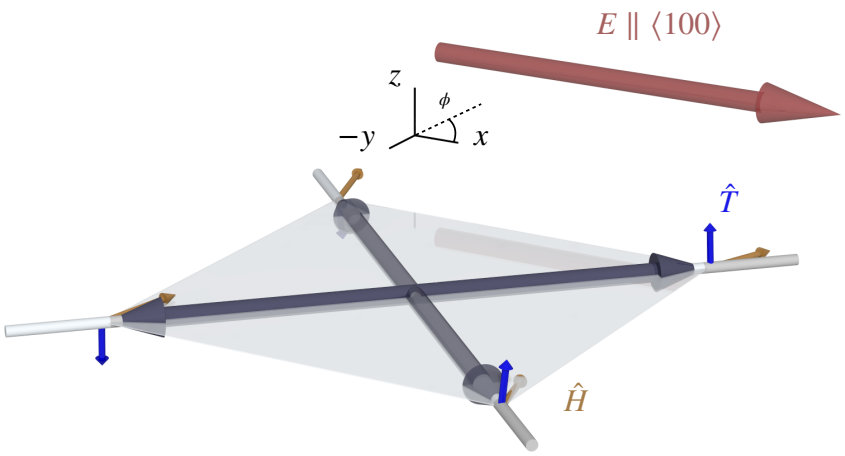

Fig. 6.4 CISP symmetry and resultant torque specifically for electric field $E \parallel \langle 100 \rangle$. The field vectors change sign with a reverse in current direction. A field $\parallel \langle 010 \rangle$ swaps the x and y accumulation.

The δm_z component changes sign between sublattices to preserve the Onsager relation. Since the unit vector of the induced field follows the unit vector of the spin accumulation, we can see the symmetry of the induced fields (gold) and generated torque (blue) as a function of the magnetisation angle ϕ, shown in Fig. 6.4, by use of Eq. (6.5). Though sharing a similar symmetry relationship as SOT for adiabatic (intraband) and non-adiabatic (interband) torque, the driving physics behind the CISP in Mn_2Au introduces higher-order corrections not present or adequately represented in the 2D tight-binding model containing only Rashba SOC [12, 160] (see Fig. 6.3). While quantitative agreement is not anticipated between the simplistic 2D model's analytic calculation and the more comprehensive 3D model requiring numerical calculations, it does demonstrate the inherent complexity present in modern magnetic materials.

The results in Fig. 6.3 calculate the spin polarisation magnitude normalised by the charge current density. Two factors, however, prevent us from implementing directly into the LLG equation the values shown in Fig. 6.3: first, the CISP represents a change to the equilibrium spin accumulation, but it is unknown how that change interacts with spin currents beyond the

calculation. Second, the Kubo response formalism calculates the spin accumulation response from the expectation value of the equilibrium spin density. In order to properly calculate the torque from the induced spin accumulation, the expectation value of the torque operator would need to be taken from the non-equilibrium spin density self-consistently calculated with the resultant change to the atomic moment exchange splitting [83, 24]. These two factors make the parametrisation in Eqs. (6.6) a poor method to implement in the same manner we used for the field-like torque of the LOT in Chapter 3. Instead, we apply the microscopic ZLF drift-diffusion equations to the spin polarisation of the *spin current* flowing between the Au and Mn layers in order to generate the non-equilibrium spin accumulation, rather than directly assuming the spin accumulation itself. For all further results, the CISP will reference the induced fields generated from the changing spin accumulation calculated by the following ZLF drift-diffusion formalism, rather than Eqs (6.6). We will reference Eqs. (6.6), however, to discuss the symmetry of the calculated spin accumulation for ease of discussion.

6.2.2 Domain Wall Driving using STT

While the mechanism for driving AFM 180° DWs using SOT was mentioned in Chapter 4, the effect on 90° DWs is more nuanced, as torque is exerted not just on the DW itself, but also each domain. Likewise is the torque generated from the STT mechanism when driven by an in-plane charge current: the torque profile is non-linear, non-adiabatic, and asymmetric across the DW, making straightforward analytic descriptions difficult. Modelling the movement of DWs from the intrinsic SOT has so far ignored the contribution of polarised in-plane spin currents exerting a non-adiabatic torque on the DW (called here the STT due to its similarities to current driven DWs in FMs), despite it being a chief mechanism for current driven FM DWs, in favor of intrinsic or injected SOT being more efficient for driving DWs in AFMs. The inclusion of the STT caused by the non-adiabatic spin accumulation moving through the DW in-plane is not expected to greatly modify the driving dynamics. The purpose of this section, however, is less on the impact the spin accumulation of the intrinsic SOT has on the DW, and more on how the DW profile changes the spin accumulation of the intrinsic SOT. The Néel SOT–when implemented as a field-like torque–does not account for the small, but significant, spin currents

acting in-plane through the domain wall. Thus, analysis of DWs driven using the field-like SOT is performed only insofar as to compare between the two models.

Utilising the same DW formalism introduced in Chapter 4, the effect of an in-plane STT on an AFM is described by a combination of the precessional torque terms–used to activate the dominant exchange enhancement–and the non-adiabatic terms–which exert an asymmetric torque on the DW chiefly described by the spin-diffusion λ_J or spin-flip length λ_{sf}. A third term describes the additional precession of the electron out of plane, The Lamor spin precession length ω_L and spin coherence length $\omega_\perp$ are used to describe the transverse damping term λ_ϕ, and is on the order of magnitude of λ_{sf}. At a simple level ignoring additional sources of spin accumulation or spin currents other than what the charge current generates moving through the DW, the torque on a DW using a macrospin approach, expressed as $-\tau = \dot{\mathbf{M}}/\gamma$, can be expressed analytically as [159]:

$$-\tau = \frac{\hbar\beta}{2eM_S^3(1+\zeta^2)}\mathbf{M}\times[\mathbf{M}\times(\mathbf{J}_e\cdot\nabla)\mathbf{M}] + \frac{\hbar\beta\zeta}{2eM_S^2(1+\zeta^2)}\mathbf{M}\times(\mathbf{J}_e\cdot\nabla)\mathbf{M}. \tag{6.7}$$

The first term on the rhs gives the damping-like torque, and the second term gives the field-like torque caused by the non-adiabatic contribution. ζ in this case is the spin-misstracking parameter, and helps to qualitatively compare the ratio of damping-like to field-like torque by representing the ratio of spin-diffusion vs. spin flip scattering through $\zeta = (\lambda_J/\lambda_{sf})^2$. When a large amount of spin-orbit coupling is present, the additional factor of the spin dephasing length must be included $\zeta' = (\lambda_J + \lambda_\phi)^2/\lambda_{sd}^2$. The ratio of damping-like to field-like torque can then generally be given by ζ or ζ'. For materials with low spin-orbit coupling $\zeta << 1$; materials with large spin-orbit effects have $\zeta' >> 1$. As we will see in the results of Sec. 6.4.2, the STT effect is not a significant driving force in Mn_2Au DWs. It is, however, a dependent factor for the spin currents generated out-of-plane by the DW. Thus, we will consider the effects $\zeta \approx 1$ and $\zeta' > 1$ have on the generated spin currents by the DW.

Since the formalism of 90° DWs was introduced in Chapter 4, we will include only the relevant results equations here for easier reference. Recall, the width factor of a 90° DW at rest Δ_0 is a combination of the effective exchange a and the in-plane anisotropy (given by the 4$^{\text{th}}$ order rotational term k_{4r}):

$$\Delta_0 = \sqrt{a/(8k_{4r})} = 17.79\text{nm} \tag{6.8}$$

If the boundary domains are fixed at $\pm\pi/4$, this gives an azimuthal angle solution for the extant of the DW:

$$\phi(x) = \arctan[e^{(x-p_0)/\Delta}] - \frac{\pi}{4} \tag{6.9}$$

The saturation velocity for the pure soliton solution in Eq. (6.9) is the magnon limit, determined by the lattice parameter a_0 and relevant exchange interactions:

$$v_m = \frac{\sqrt{8a_0^2|J_1|(J_3 + |J_1|/2)}}{\hbar} \tag{6.10}$$

In the linear regime at 0 K, the steady state DW velocity is related to the damping constant, DW width, and staggered field H through $v_0 \propto \Delta_0 H/\alpha$. For velocities nearing the magnon limit, the Lorentz invariant relationship between velocity and width (Eq. (6.11)) delivers a contraction of the width, reducing v_0. For the velocity beyond the linear regime v, the Lorentz contracted width is:

$$\Delta = \Delta_0\sqrt{1 - \frac{v^2}{v_m^2}} \tag{6.11}$$

Thus, for a driving staggered field H, the velocity v beyond the linear regime in terms of invariant width Δ_0 is:

$$v = v_m \frac{1}{\sqrt{1 + \frac{v_m^2}{\mathbf{h}\Delta_0}}} \tag{6.12}$$

where $\mathbf{h}$ is the reduced field $h \propto \gamma H/\alpha$, where parity is determined by a coefficient from the symmetry of the torque.

Complicating matters is the non-zero torque present on the boundary domains (see Fig. 6.5) changing the soliton solution in Eq. (6.9). To minimise this effect and recover a fit which matches the analytic descriptions in Eqs. (6.11) and (6.12), we allow the solution in Eq. (6.9) to vary the boundary condition set by $\pi/4$ in Eq. (6.9) whilst fitting Δ and φ to the m_y

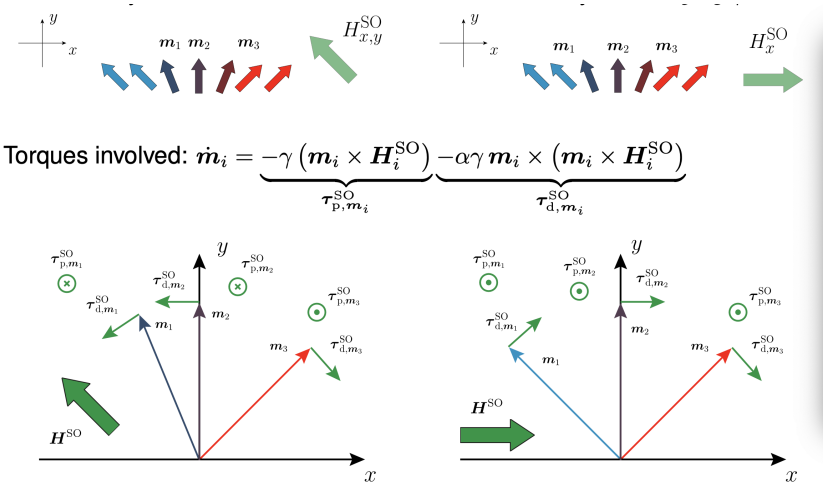

Fig. 6.5 SOT torque symmetry for 90° DWs for two different $\mathbf{H}^{so}$ orientations: a) $H^{so} \perp \pi/4$ and b) $H^{so} \parallel \hat{y}$ and thus perpendicular to the magnetisation at the DW centre. Figure courtesy of collaborator J. Vélez.

magnetisation component:

$$m_y(x) = \sin\Big(\arctan[e^{(x-p)/\Delta}] - \varphi\Big) \tag{6.13}$$

This form of Eq. (6.9) allows for a fitting of Δ which delivers a DW width factor applicable to Eqs. (6.11) and (6.12), even under the changing boundary conditions creating an asymmetric DW profile.

Fig. 6.5 shows two relevant $\mathbf{H}^{so}$ symmetries for 90° DW driving. Fig. 6.5b corresponds to our simulation geometry (with a 90° rotation so the boundary domains are along $\pm\pi/4$ giving identical symmetry).

6.3 Method

In the two-current model, where the electron spin is restricted to project purely on the up ($\uparrow$) and down ($\downarrow$) quantisation axes, the charge current and spin current are conveniently expressed as $\mathbf{j_e} = \mathbf{j}^{\uparrow} + \mathbf{j}^{\downarrow}$ and $\mathbf{j_s} = \mathbf{j}^{\uparrow} - \mathbf{j}^{\downarrow}$, respectively. This can be extended into the continuum approach with a three dimensional Cartesian projections of the net moment by a rank 2 tensor to describe the polarised current moving in each Cartesian coordinate. Then, j_d^s is the spin current with spin

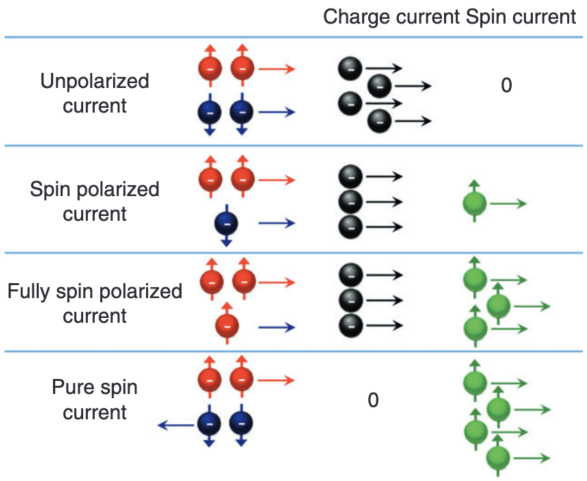

Fig. 6.6 Representation of pure and mixed spin and charge currents. Image from Y. F. Feng *et al.,* [164].

polarisation along s and direction of propagation d. This tensor can likewise be decomposed into "up" and "down" currents, though now the spin polarisation and current direction must be taken into account. Instead, it is helpful when visualising the combination of multiple layers of spin injection into one magnetic layer. Fig. 6.6 gives a diagrammatic representation for pure charge, pure spin, and partial spin polarised currents in a material.

What is not represented in Fig. 6.6 is the static case of no spin current flux density but remaining spin polarisation. This is of course the spin accumulation **m**. The distinction between the itinerant moment generated by **m** and the static atomic moment **S** is a convenient one: the atomic moment **S**–which has the majority of its density around -3 eV below the Fermi level–remains largely unperturbed by charge currents and spin-flip scattering events. This is due to its energetic distance from the carrier density at the Fermi surface, located at the high symmetry point X in the band structure (corresponding to the k-space vector $\langle 1/2, 1/2, 0 \rangle$) in Fig. 6.7. The flat dispersion around the X point is due to the high degree of crystalline symmetry in-plane. The spin accumulation **m**, however, must be described using a combination of electronic and magnetic means. These equations of motion for the spin accumulation are given by Zhang, Levy, and Fert in Ref. [165] (and expanded in Ref. [166]), and implemented into the VAMPIRE code in Ref. [167]. The full derivation of this solution is detailed in the appendix of this chapter (6.5).

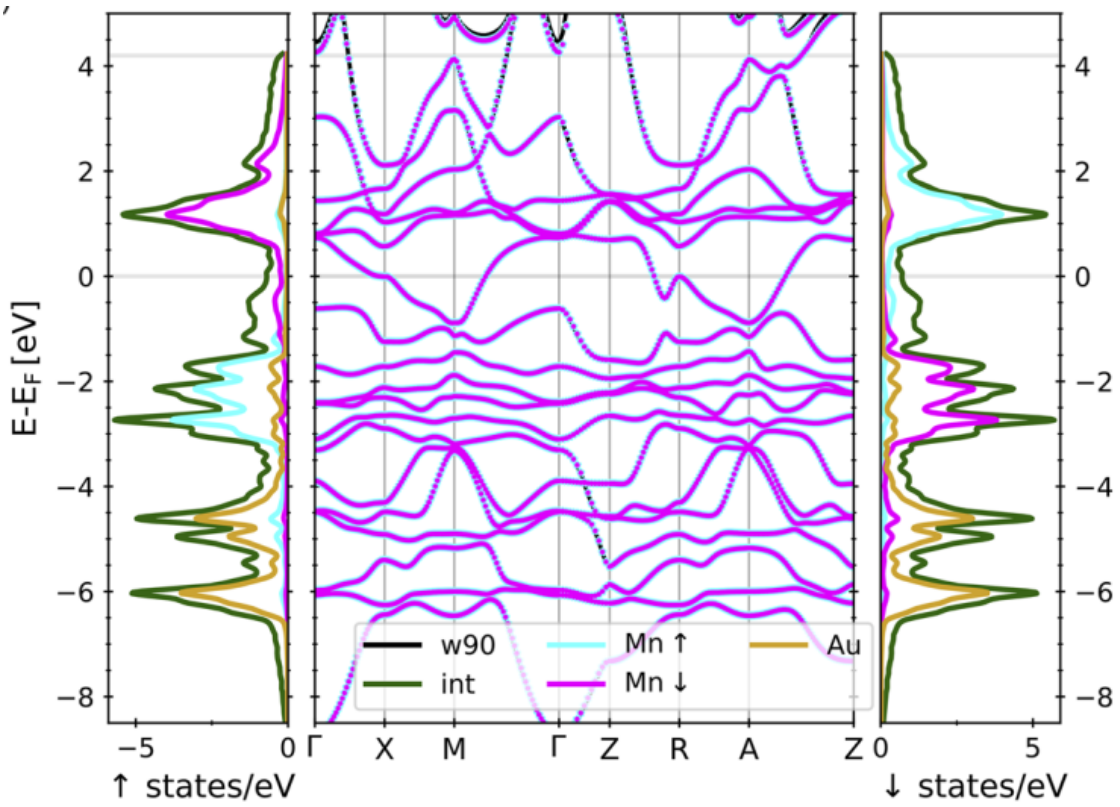

Fig. 6.7 Density of states and band structure for Mn_2Au from Merte *et al.* [83]. The high symmetry point X corresponds to the k-space vector $\langle 1/2, 1/2, 0 \rangle$.

To take into account the ISGE described above, we consider a spin current polarised along the $\pm y$ axis and injected in the $\pm z$ direction from each Au sublayer (blue and red arrows in Fig. 6.8). This in-plane polarised spin current propagating out-of-plane is proportional to the charge current magnitude j_e and Θ_{ISGE}, which is analogous to the spin Hall angle Θ_{SH} in that it parametrises the conversion of charge to spin. The spin accumulation caused by the spin current at the Au-Mn interface will experience EoM described by Eq. (6.17). The component of the spin accumulation now transverse to the atomic moment will exert a torque on the magnetisation. In other words, we allow the drift-diffusion solution in Eq. (6.14) to recreate the CISP symmetry described above. This requires a modification to the standard ZLF EoM (traditionally used only for the direction of the flowing current (grey arrow)) to consider perpendicular spin currents. For our case, we separate the orthogonal directions of the spin current travelling into the $\pm z$ axis–the currents induced from the ISGE–and the $+x$ axis–the spin currents driven by the charge current $j_e \parallel x$, which will be approximated to pick up no intrinsic spin polarisation other than what is traditionally caused by the magnetic moment (βj_e) (i.e., ignoring SOC from the Mn). This is done by separating the lattice into atomically thin stacks along x (blue rectangles in Fig. 6.8) and z (atomically thin planes with grey planes to guide the eye). These stacks contain the microcells necessary to solve the spin accumulation EoM using a finite difference method [167, 168]. For the decomposition along the z axis, the height is given as the average vertical distance between atomic sites ($h = c/6 \approx 2.69$ Å; for the decomposition along the x axis, we choose a spacing of 1 nm (which amounts to an increment $< 10\%$ of the DW width). Since the spin currents propagating in the y axis are symmetric in the exchange-limit of our system, they are not considered for this case.

Then, the two directions of spin current propagation are given by:

$$j_s^{\pm z} = \Theta_{ISGE} j_e \hat{y}^{\mp} - 2D_0 \left[\frac{\partial \mathbf{m}}{\partial \pm z} - \beta\beta' \mathbf{S} \left(\mathbf{S} \cdot \frac{\partial \mathbf{m}}{\partial \pm z} \right) \right] \tag{6.14}$$

and

$$j_s^{x} = \beta j_e \mathbf{S} - 2D_0 \left[\frac{\partial \mathbf{m}}{\partial x} - \beta\beta' \mathbf{S} \left(\mathbf{S} \cdot \frac{\partial \mathbf{m}}{\partial x} \right) \right] \tag{6.15}$$

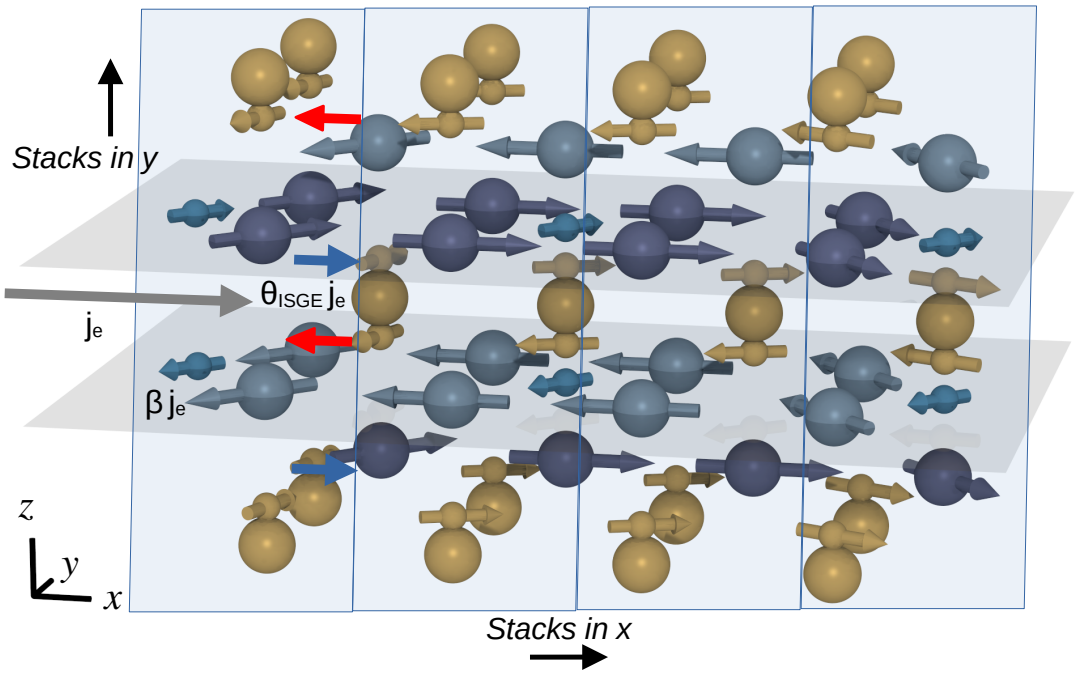

Fig. 6.8 Diagram of ISGE and spin polarised charge currents in Mn_2Au. Grey arrow is the direction of the charge current. The bright blue and red arrows are the in-plane polarised spin accumulation from the ISGE. The green arrows are the charge currents polarised by the Mn sublattice magnetisation. The large blue rectangles represent the microcell decomposition for solving the spin accumulation EoM.

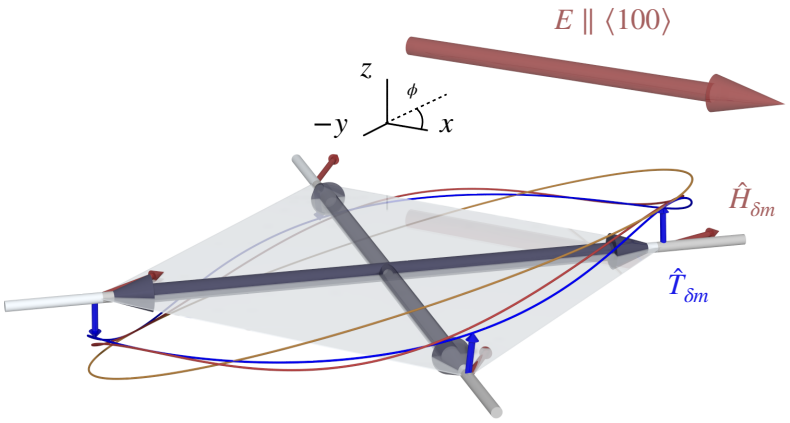

Fig. 6.9 Torque curves for in-plane magnetisation with staggered SOT field from (gold) standard field-like SOT, (blue) modified field-like torque using Eq. (6.18), and (red) spin accumulation parametrised using Eqs. (6.6).

where the second term in each equation is the drift-diffusion solution to the spin current generated by spatial gradients in the spin accumulation. The first term in Eq. (6.14) is the modelled spin current generated by the ISGE, and is parametrised as a fraction Θ_{ISGE} of the charge current j_e polarised along the $\pm\hat{y}$ directions. The corresponding $\beta j_e \mathbf{S}$ term in Eq. (6.15) gives the non-polarised charge current converted into spin from the equilibrium spin polarisation β at the Fermi level parallel to the magnetic moment $\mathbf{S}$. The density of states (DoS) (see Fig. 2.4a) at the Fermi level for spin up and spin down electrons give an equilibrium spin accumulation $m_\infty = n(\uparrow) - n(\downarrow) = 1.48 \pm 0.78 \times 10^7$ C/m^3 [55, 56, 83]. The spin conversion factor then is $\beta = n(\uparrow) - n(\downarrow)/(n(\uparrow) + n(\downarrow))$.

The equation of motion for the spin accumulation $\mathbf{m}$–without spin currents–contains the transverse damping term dependent on the spin dephasing length $(J/\hbar\omega_L\omega_\perp)$, the precession term dependent on s-d exchange $(J/\hbar)$, and the spin-flip relaxation time (τ_{sf}):

$$\frac{\mathrm{d}\mathbf{m}}{\mathrm{d}t} = -\frac{\mathbf{m}}{\tau_{sf}} - (J/\hbar)\,\mathbf{m}\times\mathbf{S} - (J/\hbar)\,\frac{\omega_L}{\omega_\perp}\mathbf{S}\times(\mathbf{m}\times\mathbf{S}) \tag{6.16}$$

The solution for the self-consistent EoM is given in [167]. For the spin current direction along $\pm z$, we solve the system of equations using the alternating direction scheme (applied to a similar system in [168]). Since the spin current along x is only in one direction, we use the initial boundary condition $j_j^x = \beta j_e \mathbf{S}$ to propagate the solution along $+x$.

The combined solution for the spin accumulation EoM and spatially varying spin current is:

$$\frac{1}{2D_0}\frac{\partial \mathbf{m}}{\partial t} = \frac{\partial^2 \mathbf{m}}{\partial x^2, \pm y^2} - \beta\beta' \mathbf{S}\left(\mathbf{S}\cdot\frac{\partial^2 \mathbf{m}}{\partial x^2, \pm y^2}\right) - \frac{m\times \mathbf{S}}{\lambda_J^2} - \frac{\mathbf{S}\times(\mathbf{m}\times\mathbf{S})}{\lambda_\phi^2} - \frac{\mathbf{m}}{\lambda_{sf}^2} \tag{6.17}$$

where $\lambda_J = \sqrt{2\hbar D_0/J}$, $\lambda_\phi = \sqrt{2\hbar D_0 \omega_\perp/(J\omega_L)}$, and $\lambda_{sf} = \sqrt{2D_0\tau_{sf}}$. The Lamor spin precession length ω_L and spin coherence length $\omega_\perp$ are used to describe the transverse damping term λ_ϕ, and is on the order of magnitude of λ_{sf}. The diffusion term D_0 and spin diffusion term β' are not apparent from *ab initio* calculations, and are usually fit from experiment. Since the physical constants in Eq. (6.16) differ for the direction of propagation, we use different values for the $\pm z$ and $+x$ equations. D_0, β', J_{sd}, and λ_{sf} for x are the usual values for metallic AFM in-plane [63, 169].

Since the ZLF drift-diffusion model is usually used to describe in-plane transport and torque for microscale systems, its use in calculating the CISP from the ISGE of a bulk material is pushing the limits of the model approximations. Two requirements for the drift-diffusion solution in Eqs. (6.15), (6.14) are that i) the gradient of the spin accumulation be smooth over the spatial discretisation [167], and ii) the length-scale of the spin current evolution be larger than the discretisation [170, 171]. Since we are investigating a perpendicular spin transport *across*–rather than along–the AFM coupled layered Mn sublattices, the gradient of the spin accumulation varies sharply with each spatial step. Since we are interested in modelling the CISP from the ISGE caused by the Au-Mn interface, the spin current must naturally evolve to the steady-state over a single interatomic distance (≈ 2.6Å). In order to stabilise the spin current across the AFM layered sublattices, we solve the spin current diffusion using the two channel model (where by symmetry in the DoS in Fig. 6.7 $\mathbf{m}_\infty^A = -\mathbf{m}_\infty^B$). Thus, the gradient along the z axis is able to vary gradually for each separate spin current propagating along $\pm z$,

respectively. The final spin current leading to the spin accumulation exerting a torque is the difference of the up/down channels.

For the short length-scale of the CISP, it is necessary to approximate the diffusion between the Au and Mn layers using a large volume. Since the height between the layers is so narrow, this requires a commensurately large surface area. In the zero temperature limit and with no spin current propagating along the y axis, we can normalise the spin accumulation by volume to remove this dependence. The solution to Eq. (6.17) likewise requires a steady-state solution ($\partial \mathbf{m}/\partial t = 0$ in the time-scale of the atomic moment precession). As discussed above, the broadening parameter Γ used to calculate the susceptibility tensors in Eq. (6.3) can correspond to the non-equilibrium lifetime of the carrier particle's excited state, and for low broadening can be on the order of 10s fs. Since the time-scale of the magnetisation dynamics are on the order of 100s fs-10 ps, we hold the evolution of the CISP are entirely driven by the magnetisation, with no time solution. It is unclear if allowing the CISP lifetimes to interact on the time-scale of the varying magnetisation will produce new symmetry features, but a comprehensive time-dependent DFT analysis beyond the approximate model used here would certainly be required.

The advantage of incorporating the CISP in this way is the ability to self-consistently calculate the resulting spin accumulation torque from spin currents with varying symmetries, either in the case of a DW (as simulated below), or a combined in-plane charge current and out-of-plane spin injected current (for future research). The later is of interest for heterostructure experiments using heli-domain Mn_2Au/Pt bilayers [172].

The constants in the $\pm z$ column of Table 6.1 have been empirically adjusted such that the spin accumulation induced field when $\mathbf{E} \parallel \hat{x}$ matches the estimated field torkance in [163, 20] and CISP symmetry in [12] (shown in Fig. 6.3). The empirical values do, however, match experimental trends well. Measurements using Mn_2Au as a source for spin polarised current injection into a FM calculate a large $\Theta_{SH} = 0.22$ [15], compared with the $\Theta_{ISGE} = -0.16$ (the sign of the conversion angle can change depending on symmetry convention). The *sd* exchange parameter for the out-of-plane direction has been increased, reflecting the stronger torque for *s* band spins moving out of plane. Likewise the spin flip length is much decreased compared

to in-plane. The diffusion constant D_0 and the spin diffusion constant β', however, represent non-physical values. This is necessary to enhance the spin current. The following table details the used constants:

Direction	$+x$	$\pm z$	Unit
β	0.23	0.23	–
β'	0.56	3.65	–
D_0	0.001	0.007	m^2/s
J_{sd}	0.05	0.3	eV
λ_{sf}	3.6	0.9615	nm
ω_L	1	–	–
$\omega_\perp$	1	–	–
Θ_{ISGE}	–	-0.16	–

Table 6.1 Drift-Diffusion constants.

To compare between the traditional model of including the intrinsic SOT as a field-like torque into the LLG Eq., we generate 90 degree switching (Fig. 6.10) and DW driving data (Fig. 6.12) for a staggered SO field $\mathbf{H}_{so} \parallel \hat{y}$. To better match the higher order ϕ dependence of the CISP, we involve an asymmetry factor to the $\mathbf{H}_{so}$ of the form:

$$\mathbf{H}_{so}^{asym} = \mathbf{H}_{so} \frac{1}{1 + l[\mathbf{S} \cdot (\hat{z} \times (\hat{z} \times \mathbf{E}))]^2} \tag{6.18}$$

Eq. (6.18) corresponds to the blue line in Fig. 6.9. $l = 0.80$ is a constant from the best fit to the red curve in Fig. 6.9. This asymmetry factor is of a higher order correction to the traditional STT asymmetry factor used in [173]. Additionally, the asymmetry factor mimics the reduced net torque generated from the induced field's varying $\hat{x}$ and $\hat{z}$ component (see Fig. 6.9). According to Eqs. (6.4) and (6.6), at $\phi = \pi/4$ the CISP produces a field $\mathbf{H}_{\delta\mathbf{m}}|_{\phi=pi/4}/J_{sd} = (0.5\sin 2\pi/4, 1.4 + 0.8\sin^2 \pi/4, -0.14\cos \pi/4)^{\mathbf{T}}$. Compared to a $H_{so} \parallel \hat{y}$ with equivalent field magnitude $|H_{so}| = |H_{\delta\mathbf{m}}|$, the effective torque decreases by a factor of 0.603, by numerical calculation. For the asymmetric torque in Eq. (6.18), the effective torque decreases by a factor of 0.563. This approximation is confirmed in the switching phase diagrams in Fig. 6.10, where the critical switching field H_{crit} is scaled by $\lambda = 1/0.603$.

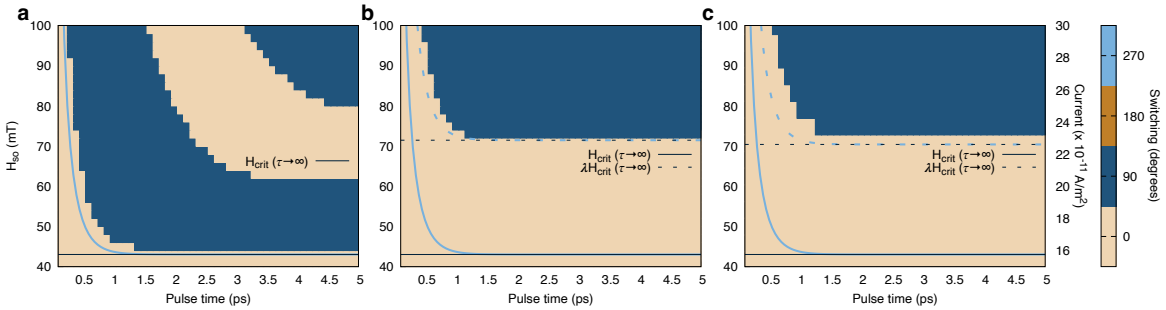

Fig. 6.10 Switching phase diagram for SOT as function of field and pulse duration. Lines correspond to the analytic solution described in [27]. a) field-like SOT. b) field-like SOT with 2^{nd} order asymmetry factor in Eq. (6.18). c) SOT from spin accumulation model.

6.4 Results

6.4.1 Switching

The spin injection from the atomic Au layers into each Mn sublayer causes a shift in the spin accumulation away from equilibrium. The normalised polarisation of the resultant spin accumulation $\delta\mathbf{m}_i/m_\infty = (\mathbf{m}_i' - \mathbf{m}_i)/m_\infty$ is compared to the *ab initio* calculations from Železný *et al.* [12]. To avoid *ab initio* differences in methodology in regards to atomic-sized magnetic moment spin currents and torque, we find it is more reasonable to compare between the direction and magnitude of the induced field, rather than the non-equilibrium spin accumulation. The magnitude of the induced spin accumulation differs widely from the tight-binding model, but the effective induced field from the non-equilibrium spin polarisation is comparable due to a difference in the used $s-d$ exchange value. We use a J_{sd} constant on the order of the Mn-Mn ferromagnetic exchange (0.5 meV), rather than Železný *et al.*'s 1 eV. Due to a larger magnitude of spin accumulation from our model, both constants produce a staggered field near 2 mT per 10^7 A/cm^2, in line with recent experimental measurements in [20].

We construct phase diagrams for $H_{so} \parallel \hat{y}$ with and without the asymmetry factor in Eq. (6.18). The asymmetry weakens the total torque experienced during the switching but does not significantly change the $\coth(t_p)$ relationship between field and pulse duration. As mentioned

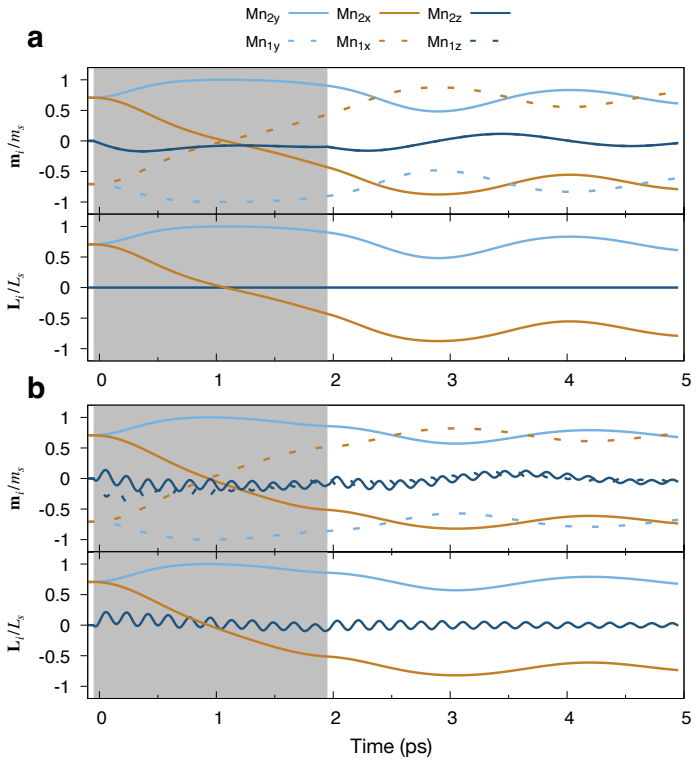

Fig. 6.11 Time dynamics for field-like SOT and CISP SOT for sublattice magnetisation $m_s = (m_1 + m_2)/2$ and Néel vector $L_s = (L_1 - L_2)/2$ for a) field-like SOT with asymmetry factor and $H_{so} \parallel \hat{y} = 0.82$ mT and b) CISP $j_e = 24 \times 10^{11}$A/m^2. Pulse duration 2 ps. m_z and L_z scaled by factor 100x for visibility.

above, the phase diagrams for the SOT mechanism using the spin accumulation model increase the critical switching field by a factor of 1.66, calculated from the reduced effective torque due to a weaker magnitude induced field, as well as a field no longer aligned $\parallel \hat{y}$. The introduction of the 2$^{\text{nd}}$ order asymmetry factor cannot reproduce the changing field direction, but does reproduce the reduced effective torque.

Fig. 6.11 shows the time dynamic sublattice magnetisation and Néel vector for a 2 ps pulse for the asymmetric field-like H_{so} and the CISP model. Both cases display nearly identical switching dynamics, with both switching on the picosecond scale for induced fields moderately above H_{crit}. The CISP switching, however, displays an additional resonance pattern in the z components due to the δm_z induced field component represented in Eq. (6.6), though it is quite

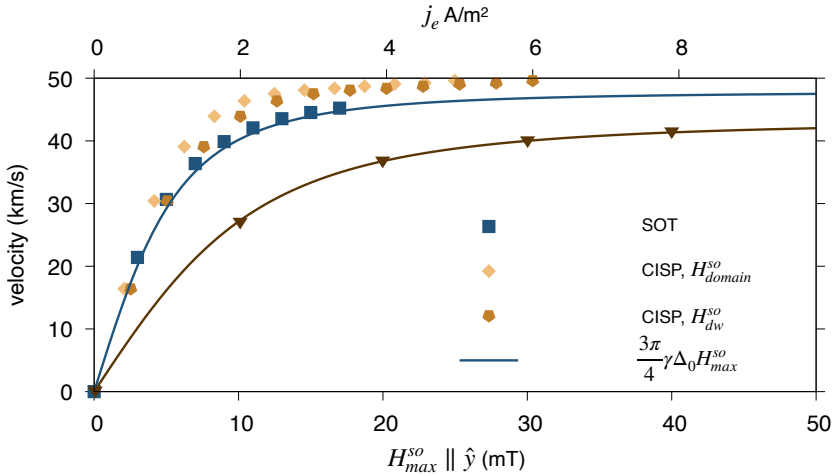

Fig. 6.12 DW steady state velocities for driving field from field-like SOT with asymmetry factor from Eq. (6.18) (blue) and CISP (gold, orange). The second y axis shows the corresponding charge current for the CISP simulations. The line shows the analytic expression for expected DW velocity for Gilbert damping 0.001 under field-like SOT, where H^{so}_{max} is the SOT field at the DW centre. (Gold): velocity vs. field relationship for the $H_{CISP} \parallel \hat{y}$ on the boundary domains. (Orange): velocity vs. field relationship for the $H_{CISP} \parallel \hat{y}$ on the DW centre. (Brown): data for comparison of a 180° DW under field-like H^{so} from [17].

minimal (scaled 100x for visibility). For the field-like torque not containing the asymmetry factor in Eq. (6.18), the dynamics are identical to a), however with a field reduced by $1/\lambda$ to match the effective torque. Thus, for most switching simulations the inclusion of Eq. (6.18) is enough to reproduce the effective torque from the CISP calculated using the ZLF drift-diffusion model.

6.4.2 Domain Wall Driving

In the section above, the CISP calculated from the ZLF drift-diffusion model of spin accumulation showed no significant effect on the switching dynamics, once the proper asymmetry factors were taken into account to reduce the effective torque. More significant differences emerge for DW driving.

Fig. 6.12 shows the results for DW steady state velocity under field-like SOT and CISP. For comparison, we also include data from [17] driving 180° DWs using a field-like SOT which follows the analytic relationship in Eq. (6.12) with a reduced field $h^{so} = \gamma\Delta_0 H^{so}$. The results from the CISP driving agree well with the field-like SOT in the linear regime, diverging at larger driving currents. The saturation velocity for the CISP is likewise larger than the field-like SOT, which in turn is larger than the calculated magnon limit for Mn_2Au (see Chapter 4). This occurs from the non-zero torque on the boundary conditions perturbing the pure soliton solution of the DW, giving $v_m^{SOT} = 47.89$ km/s from numerical fitting to Eq. (6.12). The CISP results show a further increase in the saturation velocity of $v_m^{CISP} = 49.62$ km/s, owing to the small contribution from the in-plane STT on the DW. Simulations of DW driving calculating only the effect of the in-plane STT show an order of magnitude reduction in driving efficiency due to the asymmetric nature of the torque on the DW, in line with other STT calculations in [174].

Comparing the adjusted DW width with the velocity in Fig. 6.13 shows good agreement to the analytic description in Eq. (6.11) for the field-like SOT. Simulations with only the in-plane STT contribution display instead a slight broadening of the DW: another consequence of the non-adiabatic nature of the STT. This effect may help to explain why the DW width from the CISP simulations diverges from the analytic description for high current values: rather than emit the excess energy in the form of spin waves or nucleate additional DW textures as was the case of the LOT driving in Chapter 4, the DW generates instead excess spin currents which act on the wall non-adiabatically.

The DW exceeding the analytic magnon velocity calculated in Chapter 4 is not an unexpected result: the saturation velocity holds only for a perfect soliton solution driven only by compensated torques. Indeed, any solution at finite temperature (as in Chapter 5) will also be an approximation to the saturation velocity.

6.4.3 Spin Accumulation

The ZLF drift-diffusion model allows for direct calculation of the spin current torque on the DW without relying on analytic approximations, such as in Eq. (6.7). More importantly, it reveals how the *DW* torques the spin current. To begin, we first compare between simulations

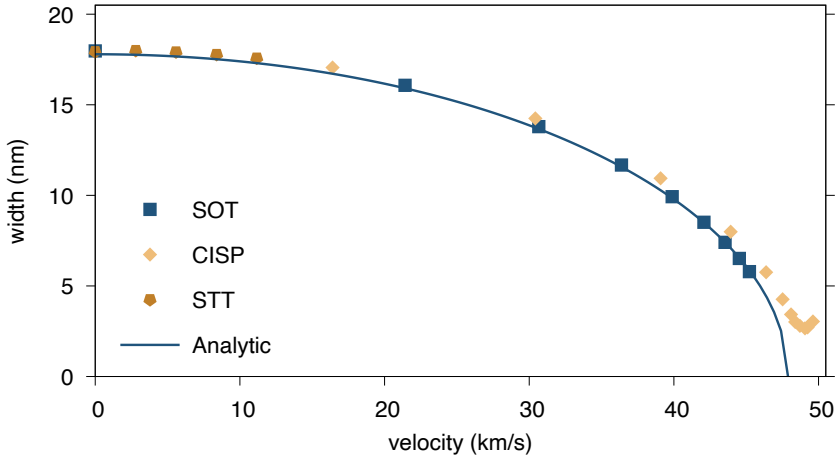

Fig. 6.13 DW width vs. steady state velocity for field-like SOT (blue), CISP (gold), and STT-only (orange). The analytic expression is from Eq. (6.11) using $v_m = 47.89$ km/s fit in from Eq. (6.12).

containing the additional dephasing length term λ_ϕ introduced from strong spin-orbit coupling (e.g. when $\zeta' >> 1$) to minimal spin-orbit coupling ($\zeta \approx 1$). Qualitatively, this can be related to the ratio of the Larmor precession frequency ω_L (intrinsic to the electron band) and the transverse precession frequency $\omega_\perp$ (loosely scaling with the strength of the magnetisation and spin-orbit coupling) [166]. In the context of Eq. (6.16), strong spin-orbit coupling (or a short frequency) leads to a large amount of transverse precession in the equation of motion. For the dephasing length λ_ϕ in Eq. (6.17), $\omega_L \approx \omega_\perp$ gives $\lambda_\phi \approx \lambda_J$. This has the effect of increasing the out-of-plane component of spin accumulation through the DW (orange line in Fig. 6.14).

We extend this comparison for the spin current propagating along x ($\mathbf{J}_s^x$, Fig. 6.15a) and along z ($\mathbf{J}_s^z$, Fig. 6.15b). The impact of dephasing shown in Fig. 6.14 is small for m_z, but in Fig. 6.15 the effect on the spin current is larger in magnitude, on the order of 100% increase for J_z^x. This effect could increase for materials with a larger λ_ϕ than the $\lambda_\phi \approx \lambda_J$ constants used here.

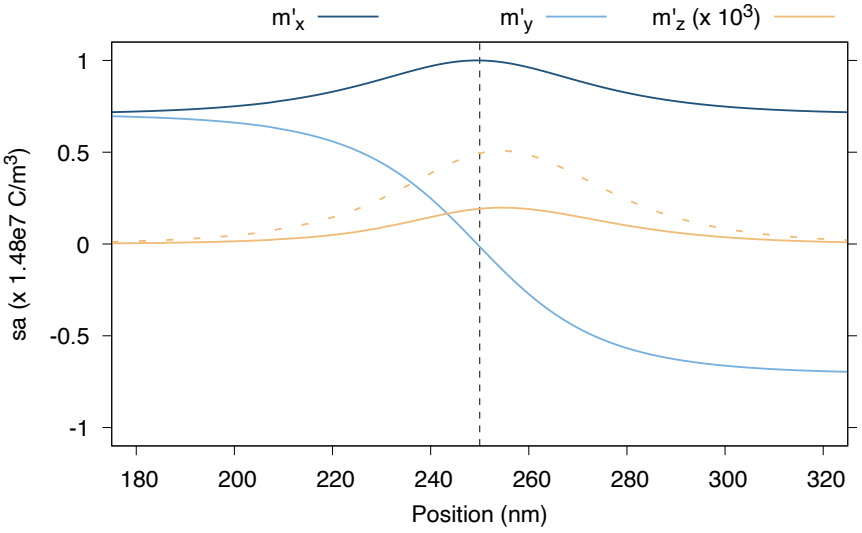

Fig. 6.14 Spin accumulation m through the DW for m_x, m_y, and m_z components. Including the dephasing length λ_ϕ has no effect on m_x and m_y. (Orange): m_z including dephasing. Dashed line shows the DW centre.

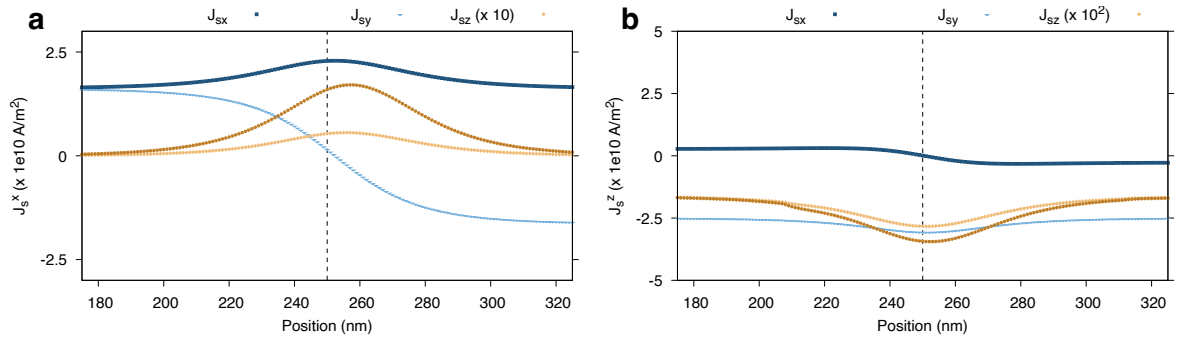

Fig. 6.15 Spin current $\mathbf{J}_s$ through the DW for J^x, and J^z components. Including the dephasing length λ_ϕ has no effect on J_x and J_y. (Orange): J_z including dephasing. Dashed line shows the centre of the DW.

6.5 Summary

The sublattice resolved model shows the effect of the CISP on the spin currents propagating along x and z. For the J^x propagation, J_x^x and J_y^x are equal and opposite. J_z^x, surprisingly, follows the same sign for both sublattices. This is due to opposite rotations of the spin accumulation from each sublattice through the DW. Surprisingly, this contribution occurs from the *adiabatic* torque on the spin accumulation, rather than the non-adiabatic torque, even though the non-adiabatic contribution to DW motion has been shown to be the driving factor [175]. The actual out-of-plane rotation is caused by the $(\mathbf{m} \times \mathbf{S})/\lambda_J^2$ term in Eq. (6.17). While Fig. 6.15 shows dephasing increasing the magnitude of the out of plane spin current, this is from an increase in the volume of spin current moving non-adiabatically past the centre of the DW. Thus, this out of plane spin current is not an effect of DW driving, but rather passing a spin polarised current through the DW. This is also seen through the out of plane contribution from the CISP being smaller in magnitude than the STT contribution, meaning this effect could be accessed in magnetic materials without intrinsic SOT or ISGE.

The out-of-plane contribution from the CISP contribution is opposite the sign of the STT contribution, though the magnitude and direction of propagation are different. The J_z^z term is scaled 100x in Fig. 6.15b, compared to 10x in a. The physical impact of the direction of propagation for a spin current at an interface is a matter of ongoing debate, as multiple factors are now involved regarding the spin mixing, boundary reflection, and spin conductance of the new layer [176]. Regardless, future improvements to this model would allow such simulations, as well as other interface effects such as tunneling magneto-resistance (TMR) with insulators. Mn_2Au is an especially promising AFM in this regard, with an unusually high TMR proposed by *ab initio* calculations [67, 177, 178]. With recent experiments showing THz emission from ultrafast charge currents following laser excitation [79], Mn_2Au multilayer, multidomain structures could be a promising candidate for neuromorphic and reservoir computing devices.

Tracking the spin accumulation across the DW allows for calculation of potential spin injection sources *from* Mn_2Au, rather than into it, as is common with AFMs. This has direct implications for AFM multilayer structures used in memory, resevoir computing, and

neuromorphic computing. Rather than have the AFM inject isotropic spin currents based on a single domain structure, a DW structure injects a time-varying and spatially varying spin injection, allowing for more sophisticated devices. At the current model stage, more work is needed to asses the spin injection from spin accumulation and spin currents passing through the multilayer interface, as the effects will be highly material dependent. At the moment, however, the model reveals the potential for AFM DWs to introduce additional control features for spin injection. This could also be the case even for AFMs without the intrinsic SHE or ISGE, as an injected spin current passing through the DW will experience the local adiabatic torque as well.

Appendix

Here we detail the full solution of **m** in the ZLF EoM Eq. 6.17. Firstly, consider the magnetic multilayer system as shown in Fig. 6.1. The charge current is injected along the x direction causing the spin current to flow perpendicularly along y and z across the planes of the layers. Based on the two-channel model, the density of the spin current is determined by the density of the current induced by the electric field and the density of the propagation current arising from changes in the spin-up and spin-down populations n with the following relationships:

$$\begin{aligned} \mathbf{j}^{\uparrow} &= \sigma^{\uparrow}\mathbf{E} - D^{\uparrow}e\nabla n^{\uparrow} \\ \mathbf{j}^{\downarrow} &= \sigma^{\downarrow}\mathbf{E} - D^{\downarrow}e\nabla n^{\downarrow} \end{aligned}$$

$$\begin{aligned} \mathbf{j}_c &= \mathbf{j}^{\uparrow} + \mathbf{j}^{\downarrow} = \sigma\mathbf{E} - D\nabla n - \beta' D\nabla \mathrm{m} \\ \mathbf{j}_s &= \mathbf{j}^{\uparrow} - \mathbf{j}^{\downarrow} = \beta\sigma\mathbf{E} + \theta_{ISGE}\sigma\zeta - \beta' D\nabla n - D\nabla \mathrm{m} \end{aligned} \tag{6.19}$$

The charge current and spin accumulation vector are assumed to polarize along the direction of the magnetization vector **M** according to the relation $\mathbf{j_c} = j_e\mathbf{M}$ and the direction of the SOC vector defined as $\zeta = (\hat{z} \times \mathbf{E}) = \mathbf{e}_y$. Therefore, the magnetization current or spin current $(\mathbf{j}_s)$ can be written in terms of the modulus of the electrical current (j_e) and the spin accumulation $(\mathbf{m})$ as,

$$\mathbf{j}_s = \beta j_e\mathbf{M} + \theta_{ISGE} j_e\mathbf{e}_y - 2D_0\left[\Delta\mathbf{m} - \beta\beta'\mathbf{M}(\mathbf{M}\cdot\Delta\mathbf{m})\right] \tag{6.20}$$

where **M** is the normalised magnetisation of the free layer. θ_{ISGE} is the inverse spin Galvanic effect coefficient–determining the in-plane charge current conversion to out-of-plane spin current. The spin polarisation parameter β for the conductivity is defined as $\boldsymbol{\sigma} = \beta\sigma_0\mathbf{M}$ and β' is the spin polarisation for the diffusion constant defined as $\mathbf{D} = \beta' D_0\mathbf{M}$. Coefficients σ_0 and D_0 are $\sigma/2$ and $D/2$, respectively.

In the system of Mn_2Au, the charge current is injected into the x direction and the spin current arising from the spin-hall effect flows in the z direction. Without loss of generality, the spin current induced by the SOC can be determined as flowing along the $\hat{z}$ axis, allowing a separation of variables for the gradient of spin accumulation in Eq. (6.20) to be along $\hat{x}$ and $\hat{z}$, with the spin current and spin accumulation in the y plane symmetric in our system exchange limit. The following details the solution process for the spin current propagating along $\hat{z}$, with the solution for the $\hat{x}$ propagating current equivalent but for the differentiation along $\hat{x}$ in Eq. (6.21).

For the current propagating along $\hat{z}$, the current is assumed to be a spin only current, i.e., no charge current. This sets the $\beta j_e \mathbf{M}$ component to zero. It will be included in these equations, however, as reference for the solution propagating along $\hat{x}$. Thus, solving for the spin current propagating along $\hat{z}$ simplifies Eq. (6.20) to:

$$\mathbf{j}_s^z = \beta j_e \mathbf{M} + \theta_{ISGE} j_e \mathbf{e}_y - 2D_0 \left[\frac{\partial \mathbf{m}}{\partial z} - \beta\beta' \mathbf{M} \left(\mathbf{M} \cdot \frac{\partial \mathbf{m}}{\partial z} \right) \right] \tag{6.21}$$

The motion of the spin accumulation is described via the *s-d* exchange interaction between the spin accumulation and the local magnetisation, $\mathcal{H}_{int} = -J\mathbf{m} \cdot \mathbf{M}$. The equation of motion of the spin accumulation can be expressed as:

$$\frac{\mathrm{d}\mathbf{m}}{\mathrm{d}t} + (J/\hbar)\, \mathbf{m} \times \mathbf{M} + (J/\hbar)\, \frac{\omega_L}{\omega_\perp} \mathbf{M} \times (\mathbf{m} \times \mathbf{M}) = -\frac{\mathbf{m}}{\tau_{sf}} \tag{6.22}$$

where $\mathbf{m}$ is the spin accumulation, $\mathbf{M}$ is the unit vector for the local magnetisation of the magnetic layer, J is the exchange energy between the electron spin and the local magnetisation, $\hbar$ is the reduced Planck constant, ω_L and $\omega_\perp$ are the electron Larmor precession and transverse precession length, respectively, and τ_{sf} is the spin-flip relaxation time of the conduction electrons.

The stationary solution of the spin accumulation ($\mathbf{m}$) decomposed into longitudinal and transverse components with respect to magnetization direction can be determined under the assumption that the relaxation time (τ_{sf}) is much shorter than the timescale of magnetization changes. To determine the components of the spin accumulation, we replace $\frac{d\mathbf{m}}{dt}$ in Eq. (6.22)

by $\frac{\partial \mathbf{m}}{\partial t} + \frac{\partial \mathbf{j}_s}{\partial z}$ (removing the z notation from j_s for readability) leading to

$$\frac{\partial \mathbf{m}}{\partial t} = -\frac{\partial \mathbf{j}_s}{\partial z} - (J/\hbar)\mathbf{m}\times\mathbf{M} - (J/\hbar)\frac{\omega_L}{\omega_\perp}\mathbf{M}\times(\mathbf{m}\times\mathbf{M}) - \frac{\mathbf{m}}{\tau_{sf}}. \tag{6.23}$$

Then we consider the value of $\frac{\partial \mathbf{j}_s}{\partial z}$ to replace in the above equation as

$$\frac{\partial \mathbf{j}_s}{\partial z} = -2D_0\left[\frac{\partial^2 \mathbf{m}}{\partial z^2} - \beta\beta'\mathbf{M}\left(\mathbf{M}\cdot\frac{\partial^2 \mathbf{m}}{\partial z^2}\right)\right]$$

Subsequently, we obtain:

$$\frac{1}{2D_0}\frac{\partial \mathbf{m}}{\partial t} = \frac{\partial^2 \mathbf{m}}{\partial z^2} - \beta\beta'\mathbf{M}\left(\mathbf{M}\cdot\frac{\partial^2 \mathbf{m}}{\partial z^2}\right) - \frac{\mathbf{m}}{\lambda_{sf}^2} - \frac{\mathbf{m}\times\mathbf{M}}{\lambda_J^2} - \frac{\mathbf{M}\times(\mathbf{m}\times\mathbf{M})}{\lambda_\phi^2} \tag{6.24}$$

where $\lambda_{sf} = \sqrt{2D_0\tau_{sf}}$, $\lambda_J = \sqrt{2\hbar D_0/J}$, and $\lambda_\phi = \sqrt{2\hbar D_0\omega_L/\omega_\perp J}$.

Stationary solution of spin accumulation

The spin accumulation is time and position dependent. However, because the timescale of the magnetisation changes is much slower than changes in spin accumulation (attosecond precession frequency vs picosecond frequency), the stationary solution of spin accumulation can be obtained with the assumption that the local magnetization is fixed and by setting $\partial\mathbf{m}/\partial t = 0$. This gives:

$$0 = \frac{\partial^2 \mathbf{m}}{\partial z^2} - \beta\beta'\mathbf{M}\left(\mathbf{M}\cdot\frac{\partial^2 \mathbf{m}}{\partial z^2}\right) - \frac{\mathbf{m}}{\lambda_{sf}^2} - \frac{\mathbf{m}\times\mathbf{M}}{\lambda_J^2} - \frac{\mathbf{M}\times(\mathbf{m}\times\mathbf{M})}{\lambda_\phi^2} \tag{6.25}$$

The solution of the spin accumulation can be separated into two parts: longitudinal ($\mathbf{m}_\parallel$) and transverse ($\mathbf{m}_\perp$) modes which are parallel and perpendicular to the direction of the local magnetization. The transformation matrix is used here to rotate the magnetization in arbitrary direction to the basis coordinate system.

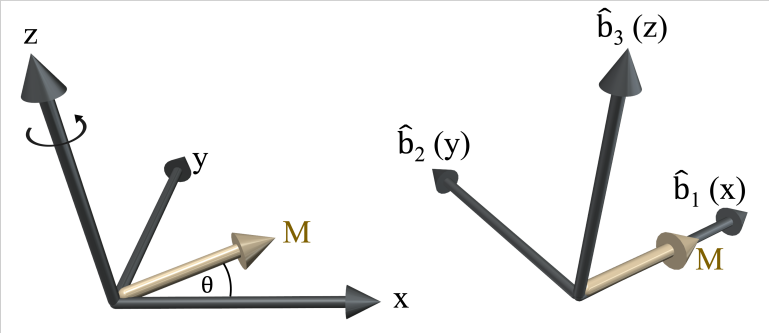

Fig. 6.16 Spin accumulation in the changed basis for (left) magnetization in the global coordinate system, and (right) in the rotated basis system.

The solution of spin accumulation is directly represented by the basis of its transverse and longitudinal modes, with the basis of the spin accumulation demonstrated relative to the magnetisation in the Cartesian coordinate in Fig. 6.16. To solve the coefficients, the spin system is discretised into microcells along $\hat{z}$ and $\hat{x}$ (for the spin current propagating along $\hat{x}$). The separation of variables is assumed to be orthogonal, and solved using an alternating direction scheme [168]. This gives a microcell size of $10 \times d \times 0.14\dot{A}^3$, where d is the y depth of the atomic lattice due to uniform spin accumulation. In its basis, the spin accumulation solution for the ODE in Eq. (6.25) using arbitrary boundaries is:

$$\begin{aligned}
\mathbf{m}_{\parallel}(z) &= \left[m_{\parallel}(\infty) + \left[m_{\parallel}(0) - m_{\parallel}(\infty)\right] e^{-\delta z/\lambda_{sdl}}\right] \hat{\mathbf{b}}_1 \\
\mathbf{m}_{\perp,2}(z) &= 2e^{-k_1 \delta z}\left[u\cos(k_2 \delta z) - v\sin(k_2 \delta z)\right] \hat{\mathbf{b}}_2 \\
\mathbf{m}_{\perp,3}(z) &= 2e^{-k_1 \delta z}\left[u\sin(k_2 \delta z) + v\cos(k_2 \delta z)\right] \hat{\mathbf{b}}_3,
\end{aligned} \tag{6.26}$$

with $(k_1 \pm ik_2) = \sqrt{\lambda_{\mathrm{sf}}^{-2} \pm i\lambda_J^{-2}}$ and δz the microcell height.

The coefficients $m_{\parallel}(0)$, u and v are constants which can be determined from the interface condition by continuity of spin current (where the solution for $\mathbf{j}_s^x$ would utilise the microcell width δx):

$$\begin{aligned}\frac{\mathbf{m}_{\perp,2}(0)+i\mathbf{m}_{\perp,3}(0)}{2} &= u+iv\\ \frac{\mathbf{m}_{\perp,2}(0)-i\mathbf{m}_{\perp,3}(0)}{2} &= u-iv\end{aligned}$$

Spin current at the interface

The spin current at the interface between the layers ($z=0$) is as follows

$$\begin{aligned}j_{mx}(0)-\beta j_e M_x &= 2D_0(\beta\beta' M_x^2-1)\frac{\partial m_x(0)}{\partial z}+2D_0\beta\beta' M_x M_y\frac{\partial m_y(0)}{\partial z}+2D_0\beta\beta' M_x M_z\frac{\partial m_z(0)}{\partial z}\\ j_{my}(0)-\beta j_e M_y-\theta_{ISGE} j_e \mathbf{e}y &= 2D_0\beta\beta' M_x M_y\frac{\partial m_x(0)}{\partial z}+2D_0(\beta\beta' M_y^2-1)\frac{\partial m_y(0)}{\partial z}+2D_0\beta\beta' M_y M_z\frac{\partial m_z(0)}{\partial z}\\ j_{mz}(0)-\beta j_e M_z &= 2D_0\beta\beta' M_x M_z\frac{\partial m_x(0)}{\partial z}+2D_0\beta\beta' M_y M_z\frac{\partial m_y(0)}{\partial z}+2D_0(\beta\beta' M_z^2-1)\frac{\partial m_z(0)}{\partial z}.\end{aligned}$$

For this case, the charge current injected perpendicular to the plane is zero. The incoming spin current at $z=0$ is $\mathbf{j}_s(0)=j_e\theta_{\mathrm{ISGE}}\mathbf{e}_y$. Then one finds the first derivative of the spin accumulation with respect to the distance at $z=0$ in the matrix form as below. It is expressed in terms of the transport parameters of the layer and the incoming spin current $j_m(0)$ from the previous layer:

$$\begin{bmatrix}\frac{\partial m_x(0)}{\partial z}\\ \frac{\partial m_y(0)}{\partial z}\\ \frac{\partial m_z(0)}{\partial z}\end{bmatrix}=\begin{bmatrix}2D_0(\beta\beta' M_x^2-1) & 2D_0\beta\beta' M_x M_y & 2D_0\beta\beta' M_x M_z\\ 2D_0\beta\beta' M_x M_y & 2D_0(\beta\beta' M_y^2-1) & 2D_0\beta\beta' M_y M_z\\ 2D_0\beta\beta' M_x M_z & 2D_0\beta\beta' M_y M_z & 2D_0(\beta\beta' M_z^2-1)\end{bmatrix}^{-1}\begin{bmatrix}j_{mx}(0)\\ j_{my}(0)\\ j_{mz}(0)\end{bmatrix}\quad(6.27)$$

Next, we need to consider $\frac{\partial m}{\partial z}$ in the global coordinate system from the spin accumulation in the basis coordinate system.

Spin accumulation at the interface

The final step is to use the derivatives of $\mathbf{m}$ using the interface conditions in Eq. (6.27) to evaluate the constants $m_{\|}(0)$, u and v which completely determine the solution for $\mathbf{m}$. The

solution of spin accumulation Eq. (6.26) in the basis coordinate system, $\mathbf{b}_1$, $\mathbf{b}_2$ and $\mathbf{b}_3$ can be rewritten to present in the global coordinate system:

$$\begin{aligned} m_x(z)\hat{\mathbf{e}}_x + m_y(z)\hat{\mathbf{e}}_y + m_z(z)\hat{\mathbf{e}}_z = & \quad m_{\parallel}(z)\hat{\mathbf{b}}_1 + m_{\perp,2}(z)\hat{\mathbf{b}}_2 + m_{\perp,3}(z)\hat{\mathbf{b}}_3 \\ = & \quad m_{\parallel}(z)\left[b_{1x}\hat{\mathbf{e}}_x + b_{1y}\hat{\mathbf{e}}_y + b_{1z}\hat{\mathbf{e}}_z\right] \\ + & \quad m_{\perp,2}(z)\left[b_{2x}\hat{\mathbf{e}}_x + b_{2y}\hat{\mathbf{e}}_y + b_{2z}\hat{\mathbf{e}}_z\right] \\ + & \quad m_{\perp,3}(z)\left[b_{3x}\hat{\mathbf{e}}_x + b_{3y}\hat{\mathbf{e}}_y + b_{3z}\hat{\mathbf{e}}_z\right] \end{aligned}$$

Determine the first derivative of the spin accumulation with respect to the distance z,

$$\begin{aligned} \frac{\partial m_x(z)}{\partial z} &= b_{1x}\frac{\partial m_{\parallel}(z)}{\partial z} + b_{2x}\frac{\partial m_{\perp,2}(z)}{\partial z} + b_{3x}\frac{\partial m_{\perp,3}(z)}{\partial z} \\ \frac{\partial m_y(z)}{\partial z} &= b_{1y}\frac{\partial m_{\parallel}(z)}{\partial z} + b_{2y}\frac{\partial m_{\perp,2}(z)}{\partial z} + b_{3y}\frac{\partial m_{\perp,3}(z)}{\partial z} \\ \frac{\partial m_z(z)}{\partial z} &= b_{1z}\frac{\partial m_{\parallel}(z)}{\partial z} + b_{2z}\frac{\partial m_{\perp,2}(z)}{\partial z} + b_{3z}\frac{\partial m_{\perp,3}(z)}{\partial z}, \end{aligned} \tag{6.28}$$

where the derivative takes the form:

$$\begin{aligned} \frac{\partial m_{\parallel}(z)}{\partial z} &= \frac{\left[m_{\parallel}(\infty) - m_{\parallel}(0)\right]}{\lambda_{sdl}} e^{-x/\lambda_{sdl}} \\ \frac{\partial m_{\perp,2}(z)}{\partial z} &= -\left[\frac{G_2}{l_+}e^{-x/l_+} + \frac{G_3}{l_-}e^{-x/l_-}\right] \\ \frac{\partial m_{\perp,3}(z)}{\partial z} &= -i\left[-\frac{G_2}{l_+}e^{-x/l_+} + \frac{G_3}{l_-}e^{-x/l_-}\right]. \end{aligned}$$

At the interface ($z = 0$), one obtains

$$\begin{aligned} \frac{\partial m_{\parallel}(0)}{\partial z} &= \frac{\left[m_{\parallel}(\infty) - m_{\parallel}(0)\right]}{\lambda_{sdl}} \\ \frac{\partial m_{\perp,2}(0)}{\partial z} &= -\left[\frac{G_2}{l_+} + \frac{G_3}{l_-}\right] = -2k_1u - 2k_2v \\ \frac{\partial m_{\perp,3}(0)}{\partial z} &= -i\left[-\frac{G_2}{l_+} + \frac{G_3}{l_-}\right] = 2k_2u - 2k_1v \end{aligned} \tag{6.29}$$

which is substituted into Eq. (6.28). Subsequently one has the following matrix form:

$$\begin{bmatrix} \frac{\partial m_x(0)}{\partial z} \\ \frac{\partial m_y(0)}{\partial z} \\ \frac{\partial m_z(0)}{\partial z} \end{bmatrix} = \frac{m_{\parallel}(\infty)}{\lambda_{sdl}} \begin{bmatrix} b_{1x} \\ b_{1y} \\ b_{1z} \end{bmatrix} + \begin{bmatrix} -\frac{b_{1x}}{\lambda_{sdl}} & (-2b_{2x}k_1 + 2b_{3x}k_2) & (-2b_{2x}k_2 - 2b_{3x}k_1) \\ -\frac{b_{1y}}{\lambda_{sdl}} & (-2b_{2y}k_1 + 2b_{3y}k_2) & (-2b_{2y}k_2 - 2b_{3y}k_1) \\ -\frac{b_{1z}}{\lambda_{sdl}} & (-2b_{2z}k_1 + 2b_{3z}k_2) & (-2b_{2z}k_2 - 2b_{3z}k_1) \end{bmatrix} \begin{bmatrix} m_{\parallel}(0) \\ u \\ v \end{bmatrix}$$

Consequently,

$$\begin{bmatrix} m_{\parallel}(0) \\ u \\ v \end{bmatrix} = \begin{bmatrix} -\frac{b_{1x}}{\lambda_{sdl}} & (-2b_{2x}k_1 + 2b_{3x}k_2) & (-2b_{2x}k_2 - 2b_{3x}k_1) \\ -\frac{b_{1y}}{\lambda_{sdl}} & (-2b_{2y}k_1 + 2b_{3y}k_2) & (-2b_{2y}k_2 - 2b_{3y}k_1) \\ -\frac{b_{1z}}{\lambda_{sdl}} & (-2b_{2z}k_1 + 2b_{3z}k_2) & (-2b_{2z}k_2 - 2b_{3z}k_1) \end{bmatrix}^{-1} \begin{bmatrix} \frac{\partial m_x(0)}{\partial z} - \frac{b_{1x}m_{\parallel}(\infty)}{\lambda_{sdl}} \\ \frac{\partial m_y(0)}{\partial z} - \frac{b_{1y}m_{\parallel}(\infty)}{\lambda_{sdl}} \\ \frac{\partial m_z(0)}{\partial z} - \frac{b_{1z}m_{\parallel}(\infty)}{\lambda_{sdl}} \end{bmatrix} \tag{6.30}$$

For simplicity, the coefficients b_{ij} in Eq. (6.32) above can be restricted to the in-plane magnetisation enforced by the strong easy-plane anisotropy of Mn_2Au:

$$[b_{i\alpha}] = \begin{bmatrix} M_x & M_y & 0 \\ -M_y & M_x & 0 \\ 0 & 0 & 1 \end{bmatrix} \tag{6.31}$$

This is then substituted into the matrix form in Eq. (6.32):

$$\begin{bmatrix} m_{\parallel}(0) \\ u \\ v \end{bmatrix} = \begin{bmatrix} -\frac{M_x}{\lambda_{sdl}} & 2M_xk_1 & 2M_yk_2 \\ -\frac{M_y}{\lambda_{sdl}} & -2M_xk_1 & -2M_xk_2 \\ 0 & 2k_2 & -2k_1 \end{bmatrix}^{-1} \begin{bmatrix} \frac{\partial m_x(0)}{\partial z} - \frac{M_x m_{\parallel}(\infty)}{\lambda_{sdl}} \\ \frac{\partial m_y(0)}{\partial z} - \frac{M_y m_{\parallel}(\infty)}{\lambda_{sdl}} \\ \frac{\partial m_z(0)}{\partial z} \end{bmatrix} \tag{6.32}$$

Finally, the unknown coefficients $m_{\parallel}(0)$, u and v can be calculated by substituting the first derivative of the spin accumulation at interface, $\frac{\partial \mathbf{m}(0)}{\partial z}$, as equation (6.27) into equation (6.32).

7

Conclusions

Sophisticated spintronic control of magnetic materials is a required foundation for ultrafast memory, reservoir and neuromorphic computing, and very-low energy data storage mediums. AFMs currently provide the best platform for these applications, at least in terms of theoretical performance. Actual control methods for multilayer AFM spintronic devices remain too coarse than the level necessary for widescale device implementation. Advancing simulation tools in order to provide accurate, high-throughput modelling and analysis of complex multilayer structures is a serious focus for the computational magnetism community. At the same time, advances in sensors and first principles calculations have discovered physical phenomena outside the bounds of bulk materials modelling. This thesis focused on applying some of these novel physical control methods to traditional ASDs simulations in the AFM Mn_2Au, in both isolated and combined forms, in order to demonstrate opportunities to control AFMs using novel methods. Mn_2Au is one of the most promising spintronic materials, but experimental studies have shown the difficulties of robust magnetic control using traditional spintronic mechanisms. Mn_2Au is an ideal material for ADSs simulations, operating as collinear, ferromagnetic, metallic sublattices with antiparallel exchange coupling. This allows minimal model approximations while maintaining large-scale simulation performance. This conclusion will summarise the key results for spintronic control in Mn_2Au and expand on future work to be applied to additional AFM materials.

7.0.1 All optical switching

Chapter 3 focused on the introduction and application of a novel first principles laser torque operating at optical frequencies to single domain switching. The unusual nature of this torque allows for ultrafast laser control of the AFM order without applied field, current, THz lasers, or circularly polarised light. Such all-optical control methods have previously been demonstrated only for ferrimagnetic systems, but only for toggle (i.e., non-deterministic) switching. The LOT in Mn_2Au can be applied in such a way as to create preferential torque patterns for the AFM order, allowing sequential pulses to deterministically change the magnetic structure regardless of the initial state. Simulations involving temperature effects of the laser-heating on the magnetisation confirm this result is not thermally-driven as it is for ferrimagnetic switching, and is robust even up to several hundred degrees above room temperature.

The existence of this novel torque has been known to the *ab initio* and experimental community, but only for insulating AFM systems at cryogenic temperatures. The application of linearly polarised optical frequencies to AFMs which are magnetic at room temperature has so far rarely been considered in the geometry presented in Chapter 3. Since the *ab initio* foundation of this LOT is based on the $\mathcal{PT}$ symmetry of the system, and is not unique to Mn_2Au. Thus, future work will focus on applications of the LOT to additional AFM materials, as well as further large-scale simulations with multi-grain domain states.

7.0.2 Domain Wall Control

Chapter 4 further applied the novel LOT to magnetic DW textures. DW modelling and control is crucial for magnetic simulations, not just as a consequence of real-world materials science but also as a feature. AFM DWs do not exhibit the Walker-breakdown present for FM systems, allowing DW driving up to the magnon limit. This is often on the order of tens of km/s–tens of nm/ps for nanoscale devices. This means even μm scale devices can manipulate DWs across the span of the device in nanoseconds, far beyond even the fastest FM DWs. Since AFMs do not emit stray fields for sensing or control, DWs represent one of the chief opportunities for encoding magnetic information for AFMs. The novel symmetry of the LOT, different in

geometry from traditional SOT/STT driving mechanisms, was shown to more efficiently drive the DW to the magnon limit than SOT fields. The symmetry of the LOT also allows for control of the DW width without driving by expanding or contracting the system. This is a direct improvement to current-based mechanisms, which require changes to the current direction in order to invert the DW propagation.

Chapter 5 extended the modelling of DWs by including temperature effects to the system. This involved rewriting the Heisenberg spin Hamiltonian from the microspin form found in the *ab initio* work of Khmelevskyi [55] and Shick [148]–into a form suitable for atomistic modelling with temperature. The resultant Hamiltonian was shown to produce macroscale constants consistent with thermodynamic scaling trends, giving proof of concept for more advanced multiscale modelling involving ASD simulations. This Hamiltonian was applied to characterise Mn_2Au DW dynamics at elevated temperatures, seeing excellent agreement with the newly constructed analytic temperature-dependent description of the DW. Excitation of the DW with the LOT showed increased efficiency over the 0 K results in Chapter 4, further supporting the use of LOT for ultrafast, low-energy spintronic control.

The future of DW simulations lies in large-scale computations modelling multi-DW interactions at temperature. This is another foundational area of research for real systems with multiple domains, and indeed the area of research for reservoir computing. ASD is the platform of choice for these experiments, as the mechanics of DW collisions beyond the most trivial cases are analytically opaque, and the micromagnetic platforms cannot handle the severe changes in magnetisation present for high-energy collisions. On a slightly smaller scale, more work is needed on the application of the LOT to DWs at elevated temperature in order to expand and contract the DW. The spin waves excited by the DW spring may be overshadowed by the thermal excitation of the system, so careful deconvolution must be performed.

7.0.3 Spin Transport

Chapter 6 presented implementation of a more robust ZLF drift-diffusion model for spin transport. Though results were presented for Mn_2Au, such a model is applicable to any magnetic material where simultaneous in-plane and out-of-plane spin transport is of interest.

The results highlight the differences between SOT and STT switching and DW driving compared to LOT and pure SOT switching for AFMs. Even though the STT mechanism represents only a small perturbation to the DW driving with SOT alone, the model allows for direct calculation of spin polarised currents applied and generated to the DW.

Though future work needs focus on the addition of multilayer interface effects on the spin currents and boundary spin accumulation, such a model would allow true multiscale simulations of magnetic heterostructure materials involving multiple spintronic control methods. Already, the model allows simulation of the control methods applied in Chapters 4 and 5 (namely LOT on DWs at temperature), with such simulations being the next focus of this project, as well as simulations of the DW-spring driving on the spin currents.

Modifying the current spin transport model to include interface effects would also allow reproduction of experiments utilising spin pumping. This is an area of spin excitation outside the realm of ZLF theory, as the generation of the ultrashort spin current pulses relies on either phenomenological descriptions of the laser-magnetism-current interaction or time-dependent Boltzmann transport solutions at the interface, rather than the Cartesian finite-difference method used in the drift-diffusion model.

Lastly, more work is needed investigating how the LOT generation of spin currents interacts with interfaces and DWs. The *ab initio* formalism for the torque mechanism in Chapter 3 calculates only the net torque on the magnetisation from the non-equilibrium charge density. Further work from the same group later applied the same Kubo linear response formalism behind the CISP discussed in Chapter 6 to the LOT, calculating the non-equilibrium laser induced spin polarisation (LISP) response generating the LOT (analogous to the CISP generating the intrinsic SOT) [83]. For single domain systems or systems without interfaces, the LOT implementation in Chapter 3 is sufficient. In the context of DWs or interfaces, however, there is ambiguity behind the effective torque and driving mechanism. This does not undermine the results of Chapters 4 or 5, but instead presents yet another potential control feature for AFM spintronics in need of investigation.

7.0.4 Summary

Overall, this thesis focused on the development and implementation of additional control features for AFMs into ASD simulations. The chief feature being the implementation and analysis of a novel all-optical torque mechanism, we present ASD simulations in combination of this method. Additional supporting changes to the ASD model present in the open-source software package VAMPIRE, such as the modified spin transport model and improved atomistic spin Hamiltonian at elevated temperatures, will allow further multiscale calculations for Mn_2Au and other complex AFM materials. Thorough understanding of the constituent parts of spintronic devices, both in isolation and combination, will pave the way for next-generation, ultrafast, efficient devices for memory, storage, and computing applications.

References

[1] R. F. L. Evans, R. W. Chantrell, U. Nowak, A. Lyberatos, and H.-J. Richter, Applied Physics Letters **100** (2012), 10.1063/1.3691196.

[2] R. Sbiaa, H. Meng, and S. N. Piramanayagam, physica status solidi (RRL) – Rapid Research Letters **5**, 413–419 (2011).

[3] A. Hirohata, K. Yamada, Y. Nakatani, I.-L. Prejbeanu, B. Diény, P. Pirro, and B. Hillebrands, Journal of Magnetism and Magnetic Materials **509**, 166711 (2020).

[4] D. Xiong, Y. Jiang, K. Shi, A. Du, Y. Yao, Z. Guo, D. Zhu, K. Cao, S. Peng, W. Cai, D. Zhu, and W. Zhao, Fundamental Research **2**, 522–534 (2022).

[5] V. Baltz, A. Manchon, M. Tsoi, T. Moriyama, T. Ono, and Y. Tserkovnyak, Reviews of Modern Physics **90**, 015005 (2018).

[6] S. Bhatti, R. Sbiaa, A. Hirohata, H. Ohno, S. Fukami, and S. Piramanayagam, Materials Today **20**, 530–548 (2017).

[7] P. Wadley, B. Howells, J. Železný, C. Andrews, V. Hills, R. P. Campion, V. Novák, K. Olejník, F. Maccherozzi, S. S. Dhesi, S. Y. Martin, T. Wagner, J. Wunderlich, F. Freimuth, Y. Mokrousov, J. Kuneš, J. S. Chauhan, M. J. Grzybowski, A. W. Rushforth, K. Edmond, B. L. Gallagher, and T. Jungwirth, Science **351**, 587 (2016).

[8] A. V. Kimel, A. Kirilyuk, P. A. Usachev, R. V. Pisarev, A. M. Balbashov, and T. Rasing, Nature **435**, 655–657 (2005).

[9] P. Wadley, B. Howells, J. Železný, C. Andrews, V. Hills, R. P. Campion, V. Novák, K. Olejník, F. Maccherozzi, S. S. Dhesi, S. Y. Martin, T. Wagner, J. Wunderlich, F. Freimuth, Y. Mokrousov, J. Kuneš, J. S. Chauhan, M. J. Grzybowski, A. W. Rushforth, K. W. Edmonds, B. L. Gallagher, and T. Jungwirth, Science **351**, 587–590 (2016).

[10] V. Barthem, C. Colin, H. Mayaffre, M.-H. Julien, and D. Givord, Nature Communications **4** (2013), 10.1038/ncomms3892.

[11] J. Železný, H. Gao, K. Výborný, J. Zemen, J. Mašek, A. Manchon, J. Wunderlich, J. Sinova, and T. Jungwirth, Phys. Rev. Lett. **113**, 157201 (2014).

[12] J. Železný, H. Gao, A. Manchon, F. Freimuth, Y. Mokrousov, J. Zemen, J. Mašek, J. Sinova, and T. Jungwirth, Physical Review B **95** (2017), 10.1103/physrevb.95.014403.

[13] S. Y. Bodnar, L. Šmejkal, I. Turek, T. Jungwirth, O. Gomonay, J. Sinova, A. A. Sapozhnik, H.-J. Elmers, M. Kläui, and M. Jourdan, Nature Communications **9** (2018), 10.1038/s41467-017-02780-x.

[14] S. Bodnar, M. Filianina, S. Bommanaboyena, T. Forrest, F. Maccherozzi, A. Sapozhnik, Y. Skourski, M. Kläui, and M. Jourdan, Physical Review B **99** (2019), 10.1103/physrevb.99.140409.

[15] B. B. Singh and S. Bedanta, Physical Review Applied **13** (2020), 10.1103/physrevapplied.13.044020.

[16] R. M. Otxoa, P. E. Roy, R. Rama-Eiroa, J. Godinho, K. Y. Guslienko, and J. Wunderlich, Communications Physics 2020 3:1 **3**, 1 (2020).

[17] R. Rama-Eiroa, P. E. Roy, J. M. González, K. Y. Guslienko, J. Wunderlich, and R. M. Otxoa, J. Magn. Magn. Mater. **560**, 169566 (2022).

[18] H. V. Gomonay and V. M. Loktev, Physical Review B **81** (2010), 10.1103/physrevb.81.144427.

[19] V. Baltz, A. Manchon, M. Tsoi, T. Moriyama, T. Ono, and Y. Tserkovnyak, Reviews of Modern Physics **90** (2018), 10.1103/revmodphys.90.015005.

[20] Y. Behovits, A. L. Chekhov, S. Y. Bodnar, O. Gueckstock, S. Reimers, Y. Lytvynenko, Y. Skourski, M. Wolf, T. S. Seifert, O. Gomonay, M. Kläui, M. Jourdan, and T. Kampfrath, Nature Communications **14** (2023), 10.1038/s41467-023-41569-z.

[21] J. Heitz, L. Nádvorník, V. Balos, Y. Behovits, A. Chekhov, T. Seifert, K. Olejník, Z. Kašpar, K. Geishendorf, V. Novák, R. Campion, M. Wolf, T. Jungwirth, and T. Kampfrath, Physical Review Applied **16** (2021), 10.1103/physrevapplied.16.064047.

[22] J. L. Ross, P.-I. Gavriloaea, F. Freimuth, T. Adamantopoulos, Y. Mokrousov, R. F. L. Evans, R. Chantrell, R. M. Otxoa, and O. Chubykalo-Fesenko, "Antiferromagnetic switching in mn_2au using a novel laser induced optical torque on ultrafast timescales," (2023).

[23] P.-I. Gavriloaea, J. L. Ross, F. Freimuth, Y. Mokrousov, R. F. L. Evans, R. Chantrell, O. Chubykalo-Fesenko, and R. M. Otxoa, "Efficient motion of 90° domain walls in mn_2au via pure optical torques," (2024).

[24] F. Freimuth, S. Blügel, and Y. Mokrousov, Physical Review B **94** (2016), 10.1103/physrevb.94.144432.

[25] F. Freimuth, S. Blügel, and Y. Mokrousov, Physical Review B **103** (2021), 10.1103/physrevb.103.174429.

[26] J. A. de Jong, I. Razdolski, A. M. Kalashnikova, R. V. Pisarev, A. M. Balbashov, A. Kirilyuk, T. Rasing, and A. V. Kimel, Physical Review Letters **108** (2012), 10.1103/physrevlett.108.157601.

[27] R. Rama-Eiroa, P. Roy, J. González, K. Guslienko, J. Wunderlich, and R. Otxoa, Journal of Magnetism and Magnetic Materials **560**, 169566 (2022).

[28] P. Park, J. Oh, K. Uhlířová, J. Jackson, A. Deák, L. Szunyogh, K. H. Lee, H. Cho, H.-L. Kim, H. C. Walker, D. Adroja, V. Sechovský, and J.-G. Park, npj Quantum Materials **3** (2018), 10.1038/s41535-018-0137-9.

[29] J.-P. Ansermet, Spintronics: A Primer (CRC Press, 2024).

[30] in Atomistic Spin Dynamics: Foundations and Applications (Oxford University Press, 2017) https://academic.oup.com/book/0/chapter/173327735/chapter-ag-pdf/49286760/book_16562_section_173327735.ag.pdf .

[31] A. Szabo and N. Ostlund, Modern Quantum Chemistry: Introduction to Advanced Electronic Structure Dover Books on Chemistry (Dover Publications, 1996).

[32] X. Feng, H. Bai, X. Fan, M. Guo, Z. Zhang, G. Chai, T. Wang, D. Xue, C. Song, and X. Fan, Physical Review Letters **132** (2024), 10.1103/physrevlett.132.086701.

[33] T. Adamantopoulos, M. Merte, F. Freimuth, D. Go, L. Zhang, M. Ležaić, W. Feng, Y. Yao, J. Sinova, L. Šmejkal, S. Blügel, and Y. Mokrousov, npj Spintronics **2** (2024), 10.1038/s44306-024-00053-0.

[34] F. Pan, J. Chico, A. Delin, A. Bergman, and L. Bergqvist, Physical Review B **95** (2017), 10.1103/physrevb.95.184432.

[35] M. O. A. Ellis, M. Galante, and S. Sanvito, Physical Review B **100** (2019), 10.1103/physrevb.100.214434.

[36] M. Strungaru, M. O. A. Ellis, S. Ruta, O. Chubykalo-Fesenko, R. F. L. Evans, and R. W. Chantrell, Physical Review B **103** (2021), 10.1103/physrevb.103.024429.

[37] I. A. Abrikosov and H. L. Skriver, Physical Review B **47**, 16532–16541 (1993).

[38] A. Ruban and H. Skriver, Computational Materials Science **15**, 119–143 (1999).

[39] R. Skomski, Simple Models of Magnetism (Oxford University Press, 2008).

[40] A. B. Shick, D. L. Novikov, and A. J. Freeman, Physical Review B **56**, R14259–R14262 (1997).

[41] A. B. Shick, S. Khmelevskyi, O. N. Mryasov, J. Wunderlich, and T. Jungwirth, Physical Review B **81** (2010), 10.1103/physrevb.81.212409.

[42] U. Atxitia, O. Chubykalo-Fesenko, R. W. Chantrell, U. Nowak, and A. Rebei, Physical Review Letters **102** (2009), 10.1103/physrevlett.102.057203.

[43] L. Waldecker, R. Bertoni, R. Ernstorfer, and J. Vorberger, Physical Review X **6** (2016), 10.1103/physrevx.6.021003.

[44] D. Zahn, F. Jakobs, H. Seiler, T. A. Butcher, D. Engel, J. Vorberger, U. Atxitia, Y. W. Windsor, and R. Ernstorfer, Physical Review Research **4** (2022), 10.1103/physrevresearch.4.013104.

[45] R. F. L. Evans, W. J. Fan, P. Chureemart, T. A. Ostler, M. O. A. Ellis, and R. W. Chantrell, Journal of Physics: Condensed Matter **26**, 103202 (2014).

[46] J. Anders, C. R. J. Sait, and S. A. R. Horsley, New Journal of Physics **24**, 033020 (2022).

[47] R. F. L. Evans, U. Atxitia, and R. W. Chantrell, Physical Review B **91** (2015), 10.1103/physrevb.91.144425.

[48] C. H. Woo, H. Wen, A. A. Semenov, S. L. Dudarev, and P.-W. Ma, Physical Review B **91** (2015), 10.1103/physrevb.91.104306.

[49] J. D. Alzate-Cardona, D. Sabogal-Suárez, R. F. L. Evans, and E. Restrepo-Parra, Journal of Physics: Condensed Matter **31**, 095802 (2019).

[50] P. Asselin, R. F. L. Evans, J. Barker, R. W. Chantrell, R. Yanes, O. Chubykalo-Fesenko, D. Hinzke, and U. Nowak, Phys. Rev. B **82**, 054415 (2010).

[51] B. Koopmans, H. Kicken, M. van Kampen, and W. de Jonge, Journal of Magnetism and Magnetic Materials **286**, 271–275 (2005).

[52] B. Koopmans, G. Malinowski, F. Dalla Longa, D. Steiauf, M. Fähnle, T. Roth, M. Cinchetti, and M. Aeschlimann, Nature Materials **9**, 259–265 (2009).

[53] L. Jiang and H.-L. Tsai, Journal of Heat Transfer **127**, 1167–1173 (2005).

[54] M. Meinert, D. Graulich, and T. Matalla-Wagner, Physical Review Applied **9** (2018), 10.1103/physrevapplied.9.064040.

[55] S. Khmelevskyi and P. Mohn, Applied Physics Letters **93**, 162503 (2008).

[56] S. Selzer, L. Salemi, A. Deák, E. Simon, L. Szunyogh, P. M. Oppeneer, and U. Nowak, Physical Review B **105** (2022), 10.1103/physrevb.105.174416.

[57] A. A. Sapozhnik, M. Filianina, S. Y. Bodnar, A. Lamirand, M.-A. Mawass, Y. Skourski, H.-J. Elmers, H. Zabel, M. Kläui, and M. Jourdan, Physical Review B **97** (2018), 10.1103/physrevb.97.134429.

[58] J. Hirst, U. Atxitia, S. Ruta, J. Jackson, L. Petit, and T. Ostler, Physical Review B **106** (2022), 10.1103/physrevb.106.094402.

[59] R. F. L. Evans, U. Atxitia, and R. W. Chantrell, Phys. Rev. B **91**, 144425 (2015).

[60] R. M. Otxoa, U. Atxitia, P. E. Roy, and O. Chubykalo-Fesenko, Communications Physics **3** (2020), 10.1038/s42005-020-0296-4.

[61] V. Grigorev, M. Filianina, Y. Lytvynenko, S. Sobolev, A. R. Pokharel, A. P. Lanz, A. Sapozhnik, A. Kleibert, S. Bodnar, P. Grigorev, Y. Skourski, M. Kläui, H.-J. Elmers, M. Jourdan, and J. Demsar, ACS Nano **16**, 20589 (2022).

[62] S. M. Rezende, A. Azevedo, and R. L. Rodríguez-Suárez, Journal of Applied Physics **126** (2019), 10.1063/1.5109132.

[63] M. Weißenhofer, F. Foggetti, U. Nowak, and P. M. Oppeneer, Physical Review B **107** (2023), 10.1103/physrevb.107.174424.

[64] M. Zhu, M. Jalali, Z. Zhang, R. F. L. Evans, J. L. Ross, R. W. Chantrell, and Y. Liu, Applied Physics Letters **126** (2025), 10.1063/5.0266902.

[65] Y. Ni, Z. Jin, B. Song, X. Zhou, H. Chen, C. Song, Y. Peng, C. Zhang, F. Pan, G. Ma, Y. Zhu, and S. Zhuang, physica status solidi (RRL) – Rapid Research Letters **15** (2021), 10.1002/pssr.202100290.

[66] T. Jungwirth, X. Marti, P. Wadley, and J. Wunderlich, Nature Nanotechnology **11**, 231–241 (2016).

[67] X.-T. Jia, X.-L. Cai, W.-Y. Yu, L.-W. Zhang, B.-J. Wang, G.-H. Cao, S.-Z. Wang, H.-M. Tang, and Y. Jia, Journal of Physics D: Applied Physics **53**, 245001 (2020).

[68] X. Zhou, X. Chen, J. Zhang, F. Li, G. Shi, Y. Sun, M. Saleem, Y. You, F. Pan, and C. Song, Physical Review Applied **11** (2019), 10.1103/physrevapplied.11.054030.

[69] R. Cheng, M. W. Daniels, J.-G. Zhu, and D. Xiao, Physical Review B **91** (2015), 10.1103/physrevb.91.064423.

[70] L. Huang, Y. Zhou, H. Qiu, H. Bai, C. Chen, W. Yu, L. Liao, T. Guo, F. Pan, B. Jin, and C. Song, Advanced Materials **34** (2022), 10.1002/adma.202205988.

[71] P. Němec, E. Rozkotová, N. Tesařová, F. Trojánek, E. D. Ranieri, K. Olejník, J. Zemen, V. Novák, M. Cukr, P. Malý, and T. Jungwirth, Nature Physics **8**, 411 (2012).

[72] P. E. Roy, R. M. Otxoa, and J. Wunderlich, Physical Review B **94** (2016), 10.1103/physrevb.94.014439.

[73] K. Olejník, T. Seifert, Z. Kašpar, V. Novák, P. Wadley, R. P. Campion, M. Baumgartner, P. Gambardella, P. Němec, J. Wunderlich, J. Sinova, P. Kužel, M. Müller, T. Kampfrath, and T. Jungwirth, Science Advances **4** (2018), 10.1126/sciadv.aar3566.

[74] E. Beaurepaire, J.-C. Merle, A. Daunois, and J.-Y. Bigot, Physical Review Letters **76**, 4250–4253 (1996).

[75] I. Radu, K. Vahaplar, C. Stamm, T. Kachel, N. Pontius, H. A. Dürr, T. A. Ostler, J. Barker, R. F. L. Evans, R. W. Chantrell, A. Tsukamoto, A. Itoh, A. Kirilyuk, T. Rasing, and A. V. Kimel, Nature **472**, 205 (2011).

[76] D. Salomoni, Y. Peng, L. Farcis, S. Auffret, M. Hehn, G. Malinowski, S. Mangin, B. Dieny, L. Buda-Prejbeanu, R. Sousa, and I. Prejbeanu, Physical Review Applied **20** (2023), 10.1103/physrevapplied.20.034070.

[77] A. V. Kimel, B. A. Ivanov, R. V. Pisarev, P. A. Usachev, A. Kirilyuk, and T. Rasing, Nature Physics **5**, 727–731 (2009).

[78] L. Huang, Y. Cao, H. Qiu, H. Bai, L. Liao, C. Chen, L. Han, F. Pan, B. Jin, and C. Song, Nature Communications **15** (2024), 10.1038/s41467-024-51440-4.

[79] L. Huang, L. Liao, H. Qiu, X. Chen, H. Bai, L. Han, Y. Zhou, Y. Su, Z. Zhou, F. Pan, B. Jin, and C. Song, Nature Communications **15** (2024), 10.1038/s41467-024-48391-1.

[80] D. Hamara, M. Strungaru, J. R. Massey, Q. Remy, X. Chen, G. Nava Antonio, O. Alves Santos, M. Hehn, R. F. L. Evans, R. W. Chantrell, S. Mangin, C. Ducati, C. H. Marrows, J. Barker, and C. Ciccarelli, Nature Communications **15** (2024), 10.1038/s41467-024-48795-z.

[81] G.-M. Choi, A. Schleife, and D. G. Cahill, Nature Communications **8** (2017), 10.1038/ncomms15085.

[82] T. Dannegger, M. Berritta, K. Carva, S. Selzer, U. Ritzmann, P. M. Oppeneer, and U. Nowak, Physical Review B **104** (2021), 10.1103/physrevb.104.l060413.

[83] M. Merte, F. Freimuth, D. Go, T. Adamantopoulos, F. R. Lux, L. Plucinski, O. Gomonay, S. Blügel, and Y. Mokrousov, APL Materials **11** (2023), 10.1063/5.0149955.

[84] J. K. Dewhurst, P. Elliott, S. Shallcross, E. K. U. Gross, and S. Sharma, Nano Letters **18**, 1842–1848 (2018).

[85] M. Merte, F. Freimuth, D. Go, T. Adamantopoulos, F. R. Lux, L. Plucinski, O. Gomonay, S. Blügel, and Y. Mokrousov, APL Materials **11**, 71106 (2023).

[86] T. Adamantopoulos, D. Go, P. M. Oppeneer, and Y. Mokrousov, npj Spintronics **3** (2025), 10.1038/s44306-025-00089-w.

[87] Y. Behovits, A. L. Chekhov, S. Y. Bodnar, O. Gueckstock, S. Reimers, Y. Lytvynenko, Y. Skourski, M. Wolf, T. S. Seifert, O. Gomonay, M. Kläui, M. Jourdan, and T. Kampfrath, Nature Communications 2023 14:1 **14**, 1 (2023).

[88] A. Kurenkov, S. Fukami, and H. Ohno, Journal of Applied Physics **128** (2020), 10.1063/5.0009482.

[89] A. M. Kalashnikova, A. V. Kimel, R. V. Pisarev, V. N. Gridnev, A. Kirilyuk, and T. Rasing, Physical Review Letters **99** (2007), 10.1103/physrevlett.99.167205.

[90] T. Satoh, S.-J. Cho, R. Iida, T. Shimura, K. Kuroda, H. Ueda, Y. Ueda, B. A. Ivanov, F. Nori, and M. Fiebig, Physical Review Letters **105** (2010), 10.1103/physrevlett.105.077402.

[91] M. Merte, F. Freimuth, T. Adamantopoulos, D. Go, T. G. Saunderson, M. Kläui, L. Plucinski, O. Gomonay, S. Blügel, and Y. Mokrousov, Physical Review B **104** (2021), 10.1103/physrevb.104.l220405.

[92] D. Afanasiev, B. Ivanov, A. Kirilyuk, T. Rasing, R. V. Pisarev, and A. V. Kimel, Physical Review Letters **116** (2016), 10.1103/physrevlett.116.097401.

[93] R. Bläsing, A. A. Khan, P. C. Filippou, C. Garg, F. Hameed, J. Castrillon, and S. S. P. Parkin, Proceedings of the IEEE **108**, 1303 (2020).

[94] Y. Yamane, O. Gomonay, H. Velkov, and J. Sinova, Physical Review B **96** (2017), 10.1103/physrevb.96.064408.

[95] M. Kläui, Journal of Physics: Condensed Matter **20**, 313001 (2008).

[96] O. Gomonay, K. Yamamoto, and J. Sinova, Journal of Physics D: Applied Physics **51**, 264004 (2018).

[97] S. K. Kim, O. Tchernyshyov, and Y. Tserkovnyak, Physical Review B **92** (2015), 10.1103/physrevb.92.020402.

[98] S. Selzer, U. Atxitia, U. Ritzmann, D. Hinzke, and U. Nowak, Physical Review Letters **117** (2016), 10.1103/physrevlett.117.107201.

[99] O. Gomonay, T. Jungwirth, and J. Sinova, Physical Review Letters **117**, 017202 (2016).

[100] F. Rubio-Marcos, A. Del Campo, P. Marchet, and J. F. Fernández, Nature Communications **6** (2015), 10.1038/ncomms7594.

[101] T. Janda, P. E. Roy, R. M. Otxoa, Z. Šobáň, A. Ramsay, A. C. Irvine, F. Trojanek, M. Surýnek, R. P. Campion, B. L. Gallagher, P. Němec, T. Jungwirth, and J. Wunderlich, Nature Communications **8** (2017), 10.1038/ncomms15226.

[102] J. Godinho, P. K. Rout, R. Salikhov, O. Hellwig, Z. Šobáň, R. M. Otxoa, K. Olejník, T. Jungwirth, and J. Wunderlich, npj Spintronics **2** (2024), 10.1038/s44306-024-00027-2.

[103] T. Koyama, K. Ueda, K.-J. Kim, Y. Yoshimura, D. Chiba, K. Yamada, J.-P. Jamet, A. Mougin, A. Thiaville, S. Mizukami, S. Fukami, N. Ishiwata, Y. Nakatani, H. Kohno, K. Kobayashi, and T. Ono, Nature Nanotechnology **7**, 635–639 (2012).

[104] Y. Liu and P. Grütter, Journal of Applied Physics **83**, 5922–5926 (1998).

[105] E. G. Tveten, T. Müller, J. Linder, and A. Brataas, Phys. Rev. B **93**, 104408 (2016).

[106] R. Rama-Eiroa, P. E. Roy, J. M. González, K. Y. Guslienko, J. Wunderlich, and R. M. Otxoa, Journal of Magnetism and Magnetic Materials **560**, 169566 (2022).

[107] B. A. Ivanov and A. K. Kolezhuk, Phys. Rev. Lett. **74**, 1859 (1995).

[108] N. Papanicolaou, Phys. Rev. B **51**, 15062 (1995).

[109] I. V. Bar'yakhtar and B. A. Ivanov, Solid State Communications **34**, 545 (1980).

[110] S. P. Bommanaboyena, D. Backes, L. S. I. Veiga, S. S. Dhesi, Y. R. Niu, B. Sarpi, T. Denneulin, A. Kovács, T. Mashoff, O. Gomonay, J. Sinova, K. Everschor-Sitte, D. Schönke, R. M. Reeve, M. Kläui, H.-J. Elmers, and M. Jourdan, Nature Communications **12** (2021), 10.1038/s41467-021-26892-7.

[111] X. Ge, P. Yan, W. Luo, S. Liang, and Y. Zhang, Applied Physics Letters **124** (2024), 10.1063/5.0189508.

[112] R. V. Ovcharov, B. A. Ivanov, J. Åkerman, and R. S. Khymyn, Physical Review B **109** (2024), 10.1103/physrevb.109.l140406.

[113] Y. Behovits, A. L. Chekhov, B. R. Serrano, A. Ruge, S. Reimers, Y. Lytvynenko, M. Kläui, M. Jourdan, and T. Kampfrath, "All-optical magnetometric characterization of the antiferromagnetic exchange-spring system mn_2au|py by terahertz spin-torques," (2024).

[114] A. Kimel, T. Rasing, and B. Ivanov, Journal of Magnetism and Magnetic Materials **598**, 172039 (2024).

[115] Y. Quessab, R. Medapalli, M. S. El Hadri, M. Hehn, G. Malinowski, E. E. Fullerton, and S. Mangin, Physical Review B **97**, 054419 (2018).

[116] U. Parlak, R. Adam, D. E. Bürgler, S. Gang, and C. M. Schneider, Physical Review B **98**, 214443 (2018).

[117] A. Kurenkov, S. Fukami, and H. Ohno, Journal of Applied Physics **128**, 10902 (2020).

[118] M. Fattouhi, A. Thiaville, F. García-Sánchez, R. M. Otxoa, M. P. G. Estévez, E. Martínez, and L. López-Díaz, Communications Physics **8** (2025), 10.1038/s42005-025-02155-5.

[119] J. A. Vélez, M.-K. Lee, G. Tatara, P.-I. Gavriloaea, J. Ross, D. Laroze, U. Atxitia, R. F. L. Evans, R. W. Chantrell, M. Mochizuki, and R. M. Otxoa, npj Spintronics **3** (2025), 10.1038/s44306-025-00079-y.

[120] G. Bourianoff, D. Pinna, M. Sitte, and K. Everschor-Sitte, AIP Advances **8**, 55602 (2018).

[121] S. Y. Bodnar, L. Šmejkal, I. Turek, T. Jungwirth, O. Gomonay, J. Sinova, A. A. Sapozhnik, H. J. Elmers, M. Klaüi, and M. Jourdan, Nature Communications 2018 9:1 **9**, 1 (2018).

[122] A. H. MacDonald and M. Tsoi, Philosophical Transactions of the Royal Society A: Mathematical, Physical and Engineering Sciences **369**, 3098 (2011).

[123] E. V. Gomonay and V. M. Loktev, Low Temperature Physics **40**, 17 (2014).

[124] V. Baltz, A. Manchon, M. Tsoi, T. Moriyama, T. Ono, and Y. Tserkovnyak, Rev. Mod. Phys. **90**, 015005 (2018).

[125] T. Jungwirth, J. Sinova, A. Manchon, X. Marti, J. Wunderlich, and C. Felser, Nature Physics **14**, 200 (2018).

[126] M. B. Jungfleisch, W. Zhang, and A. Hoffmann, Physics Letters A **382**, 865 (2018).

[127] S. Fukami, V. O. Lorenz, and O. Gomonay, Journal of Applied Physics **128**, 070401 (2020).

[128] A. A. Sapozhnik, M. Filianina, S. Y. Bodnar, A. Lamirand, M.-A. Mawass, Y. Skourski, H.-J. Elmers, H. Zabel, M. Kläui, and M. Jourdan, Physical Review B **97**, 134429 (2018).

[129] M. Meinert, D. Graulich, and T. Matalla-Wagner, Phys. Rev. Applied **9**, 064040 (2018).

[130] M. Dunz, T. Matalla-Wagner, and M. Meinert, Phys. Rev. Research **2**, 013347 (2020).

[131] P. Sheng, Z. Zhao, O. J. Benally, D. Zhang, and J.-P. Wang, "Thermal contribution in the electrical switching experiments with heavy metal / antiferromagnet structures," (2021), arXiv:2107.13859 .

[132] C. C. Chiang, S. Y. Huang, D. Qu, P. H. Wu, and C. L. Chien, Phys. Rev. Lett. **123**, 227203 (2019).

[133] R. F. L. Evans, W. J. Fan, P. Chureemart, T. A. Ostler, M. O. A. Ellis, and R. W. Chantrell, J. Phys.: Condens. Matt. **26**, 103202 (2014).

[134] P. E. Roy, R. M. Otxoa, and J. Wunderlich, Phys. Rev. B **94**, 014439 (2016).

[135] R. M. Otxoa, R. Rama-Eiroa, P. E. Roy, G. Tatara, O. Chubykalo-Fesenko, and U. Atxitia, Phys. Rev. Research **3**, 043069 (2021).

[136] R. M. Otxoa, G. Tatara, P. E. Roy, and O. Chubykalo-Fesenko, Scientific Reports (2023).

[137] U. Atxitia, P. Nieves, and O. Chubykalo-Fesenko, Physical Review B **86** (2012), 10.1103/physrevb.86.104414.

[138] P. Nieves, U. Atxitia, R. W. Chantrell, and O. Chubykalo–Fesenko, Low Temperature Physics **41**, 739 (2015).

[139] V. Puliafito, R. Khymyn, M. Carpentieri, B. Azzerboni, V. Tiberkevich, A. Slavin, and G. Finocchio, Phys. Rev. B **99**, 024405 (2019).

[140] L. Sanchez-Tejerina, R. Tomasello, V. Puliafito, B. Azzerboni, M. Carpentieri, and G. Finocchio, IEEE Magnetics Letters **11**, 1 (2020).

[141] S. Khmelevskyi and P. Mohn, Applied Physics Letters **93**, 162503 (2008).

[142] A. B. Shick, S. Khmelevskyi, O. N. Mryasov, J. Wunderlich, and T. Jungwirth, Phys. Rev. B **81**, 212409 (2010).

[143] O. Mryasov, U. Nowak, K. Guslienko, and R. Chantrell, Europhysics Letters **69**, 805 (2005).

[144] N. Akulov, Zeitschrift für Physik **100**, 197 (1936).

[145] C. Zener, Phys. Rev. **96**, 1335 (1954).

[146] H. Callen and E. Callen, Journal of Physics and Chemistry of Solids **27**, 1271 (1966).

[147] J. B. Collings, R. Rama-Eiroa, R. M. Otxoa, R. F. L. Evans, and R. W. Chantrell, Physical Review B **107** (2023), 10.1103/physrevb.107.064413.

[148] A. B. Shick, S. Khmelevskyi, O. N. Mryasov, J. Wunderlich, and T. Jungwirth, Phys. Rev. B **81**, 212409 (2010).

[149] R. F. L. Evans, L. Rózsa, S. Jenkins, and U. Atxitia, Phys. Rev. B **102**, 020412 (2020).

[150] L. Rózsa and U. Atxitia, Physical Review Research **5** (2023), 10.1103/physrevresearch.5.023139.

[151] M. S. Gebre, R. K. Banner, K. Kang, K. Qu, H. Cao, A. Schleife, and D. P. Shoemaker, Physical Review Materials **8** (2024), 10.1103/physrevmaterials.8.084413.

[152] K. Hayakawa, S. Kanai, T. Funatsu, J. Igarashi, B. Jinnai, W. Borders, H. Ohno, and S. Fukami, Physical Review Letters **126** (2021), 10.1103/physrevlett.126.117202.

[153] U. Atxitia, D. Hinzke, O. Chubykalo-Fesenko, U. Nowak, H. Kachkachi, O. N. Mryasov, R. F. Evans, and R. W. Chantrell, Physical Review B **82** (2010), 10.1103/physrevb.82.134440.

[154] N. Kazantseva, R. Wieser, and U. Nowak, Physical Review Letters **94** (2005), 10.1103/physrevlett.94.037206.

[155] J. Hirst, U. Atxitia, S. Ruta, J. Jackson, L. Petit, and T. Ostler, Physical Review B **106** (2022), 10.1103/physrevb.106.094402.

[156] S. Reimers, O. Gomonay, O. J. Amin, F. Krizek, L. X. Barton, Y. Lytvynenko, S. F. Poole, V. Novák, R. P. Campion, F. Maccherozzi, G. Carbone, A. Björling, Y. Niu, E. Golias, D. Kriegner, J. Sinova, M. Kläui, M. Jourdan, S. S. Dhesi, K. W. Edmonds, and P. Wadley, Physical Review Applied **21** (2024), 10.1103/physrevapplied.21.064030.

[157] R. M. Otxoa, U. Atxitia, P. E. Roy, and O. Chubykalo-Fesenko, Communications Physics 2020 3:1 **3**, 1 (2020).

[158] P. M. Haney, H.-W. Lee, K.-J. Lee, A. Manchon, and M. D. Stiles, Physical Review B **87** (2013), 10.1103/physrevb.87.174411.

[159] V. Baltz, The basics of electron transport in spintronics: textbook with lectures, exercises and solutions (EDP Sciences, 2023).

[160] H. Li, H. Gao, L. P. Zârbo, K. Výborný, X. Wang, I. Garate, F. Doğan, A. Čejchan, J. Sinova, T. Jungwirth, and A. Manchon, Physical Review B **91** (2015), 10.1103/physrevb.91.134402.

[161] F. Freimuth, S. Blügel, and Y. Mokrousov, Physical Review B **90** (2014), 10.1103/physrevb.90.174423.

[162] M. Jourdan, J. Bläßer, G. O. Gámez, S. Reimers, L. Odenbreit, M. Fischer, Y. R. Niu, E. Golias, F. Maccherozzi, A. Kleibert, H. Stoll, and M. Kläui, Physical Review B **112** (2025), 10.1103/tjhp-rzcb.

[163] J. Železný, H. Gao, K. Výborný, J. Zemen, J. Mašek, A. Manchon, J. Wunderlich, J. Sinova, and T. Jungwirth, Physical Review Letters **113**, 157201 (2014).

[164] Y. P. Feng, L. Shen, M. Yang, A. Wang, M. Zeng, Q. Wu, S. Chintalapati, and C. Chang, WIREs Computational Molecular Science **7** (2017), 10.1002/wcms.1313.

[165] S. Zhang, P. M. Levy, and A. Fert, Physical Review Letters **88** (2002), 10.1103/physrevlett.88.236601.

[166] C. Petitjean, D. Luc, and X. Waintal, Physical Review Letters **109** (2012), 10.1103/physrevlett.109.117204.

[167] P. Chureemart, I. D'Amico, and R. W. Chantrell, Journal of Physics: Condensed Matter **27**, 146004 (2015).

[168] S. Lepadatu, Scientific Reports **7** (2017), 10.1038/s41598-017-13181-x.

[169] M. Arana, M. Gamino, E. F. Silva, V. M. T. S. Barthem, D. Givord, A. Azevedo, and S. M. Rezende, Physical Review B **98** (2018), 10.1103/physrevb.98.144431.

[170] D. M. Nenno, S. Kaltenborn, and H. C. Schneider, Physical Review B **94** (2016), 10.1103/physrevb.94.115102.

[171] Q. Remy, Physical Review B **107** (2023), 10.1103/physrevb.107.174431.

[172] H. Masuda, T. Seki, J.-i. Ohe, Y. Nii, H. Masuda, K. Takanashi, and Y. Onose, Nature Communications **15** (2024), 10.1038/s41467-024-46326-4.

[173] C. Serpico, G. Bertotti, I. D. Mayergoyz, M. d'Aquino, and R. Bonin, Journal of Applied Physics **99** (2006), 10.1063/1.2158388.

[174] M.-K. Lee, R. M. Otxoa, and M. Mochizuki, Physical Review B **110** (2024), 10.1103/physrevb.110.l020408.

[175] H.-J. Park, Y. Jeong, S.-H. Oh, G. Go, J. H. Oh, K.-W. Kim, H.-W. Lee, and K.-J. Lee, Physical Review B **101** (2020), 10.1103/physrevb.101.144431.

[176] L. Cao, S. Ruta, R. Khamtawi, P. Chureemart, Y. Zhai, R. F. L. Evans, and R. W. Chantrell, Journal of Physics: Condensed Matter **36**, 305901 (2024).

[177] C. Zhu, X. Jia, and H.-M. Tang, Journal of Magnetism and Magnetic Materials **597**, 172036 (2024).

[178] X. Jia, H.-M. Tang, and S.-Z. Wang, Physical Review B **108** (2023), 10.1103/physrevb.108.104406.